

DESIGN OF ALD-BASED CATALYSTS AND PROCESSES FOR
DRY REFORMING OF METHANE

A Dissertation

by

SHAIK AFZAL

Submitted to the Office of Graduate and Professional Studies of
Texas A&M University
in partial fulfillment of the requirements for the degree of

DOCTOR OF PHILOSOPHY

| | |
|------------------------|--------------------|
| Chair of Committee, | Nimir Elbashir |
| Co-Chair of Committee, | Mahmoud El-Halwagi |
| Committee Members, | Patrick Linke |
| | Hamid Parsaei |
| Head of Department, | Arul Jayaraman |

August 2020

Major Subject: Chemical Engineering

Copyright 2020 Shaik Afzal

ABSTRACT

Dry reforming of methane (DRM) is an important process that utilizes CO_2 to convert methane into a mixture of H_2 and CO (synthesis gas or syngas). Commercial applicability of DRM has been challenged by the high energy requirement, susceptibility to coke formation, and low-quality syngas (syngas ratio, $\text{H}_2/\text{CO} \sim 1$). In this work, a multi-scale approach is used to address each of these challenges in a systematic way.

A commercial 20% nickel-based catalyst is used as a benchmark, and the performance of all synthesized catalysts is compared with this benchmark catalyst. Atomic Layer Deposition (ALD) is used to deposit alumina over Ni catalysts to improve the coking and sintering resistance. In the first part of the catalysis work, the performance of commercial catalyst overcoated with 5 cycles of ALD alumina was compared with the uncoated commercial catalyst. Throughout 40 h time-on-stream, the rate of drop in catalyst dispersion was much lower in the 5-ALD catalyst when compared to the uncoated catalyst. Without sacrificing catalytic activity, the amount of coke formation in the 5-ALD catalyst decreased by 50%. In the second part of the catalysis work, pretreatment methods are investigated to modify the overcoat properties. The protocol described could be used to modify/synthesize reforming catalysts through ALD with tunable properties.

Having an efficient catalyst for DRM is not the only challenge for its industrial applicability. To better understand the impact of DRM on the reduction of carbon footprint and process economics, a Life Cycle Analysis (LCA) study was conducted. An optimization-based approach is used to compare the carbon footprint of conventional reforming technologies with other processes involving DRM to produce syngas of different H_2/CO ratios. Technical, economic, and environmental metrics are used to evaluate processes that can utilize the varying H_2/CO ratio of syngas, and promising pathways are highlighted. This multi-scale work has identified treatment techniques for ALD catalysts and modifications to the DRM process that hold potential for the future, both in terms of reducing the overall carbon footprint and operating costs of syngas production.

DEDICATION

To my parents, my wife, and my sister.

ACKNOWLEDGMENTS

In the name of God, Most Gracious, Most Merciful.

I would like to thank my committee chair, Dr. Nimir Elbashir, for all his support and guidance throughout the many years I have been his student in my master's and PhD. I have had various opportunities to perform significant research across many areas and I consider myself fortunate and honored to be a part of his research team. I would like to thank my committee co-chair, Dr. Mahmoud El-Halwagi, for his support and guidance in my work. It is an honor to work under the same professor whose book I used during my undergraduate years in India! I also want to thank my committee members, Dr. Patrick Linke and Dr. Hamid Parsaei for their valuable feedback and support during the course of my study.

Thanks also go to my friends and colleagues, Anuj Prakash, Dr. Hanif Choudhary, Sufiyan Challiwala, Dr. Anjaneyulu Chatla, Dr. Patrick Littlewood, Ziyen Sheriff and Raid Hassiba. The many hours spent in the lab together while doing experiments have created life-long friendships 😊 At College Station, I would like to thank Dr. Debalina Sengupta, Abdulrahman Alsuhaibani and Ahmad Al-Douri for their support in my work and their valuable feedback. I am grateful to have worked with a passionate group of skilled researchers in both teams of Doha and College Station. I would like to thank Hania and Cherine from Doha campus, and Ashley and Terah from College Station for their help and support with all the work that accompanied while moving between campuses that are 8000 miles apart!

Finally, thanks to my mother, Anjum, my father, Ilyas, my wife, Wafa, and my sister, Ayesha, for their love, support, and encouragement throughout the period of my study.

CONTRIBUTORS AND FUNDING SOURCES

Contributors

This work was supervised by a dissertation committee consisting of Professor Nimir Elbashir [chair] and Professor Mahmoud El-Halwagi [co-chair], Professor Patrick Linke [member] and Professor Hamid Parsaei [member].

The ALD catalysts that have been used for the studies in Chapters 2 and 3 were prepared by Dr. Patrick Littlewood at Northwestern University. The Design of Experiments in section 3.1 was performed by Dr. Patrick Littlewood from Northwestern University and Dr. Daniel Curulla from TOTAL. The BET surface area for the catalysts in section 3.1.1 was obtained by Dr. Patrick Littlewood. The Raman experiment shown in Figure 36 was performed by Dr. Zafar Khan Ghouri from Texas A&M University at Qatar. I would like to acknowledge Dr. Said Mansour of Qatar Environment and Energy Research Institute (QEERI) and Dr. Kim Hansoo from Microscopy Imaging Center (MIC), Texas A&M University for their support in obtaining TEM images.

All other work conducted for the dissertation was completed by the student independently.

Funding Sources

This work was supported by the Qatar National Research Fund (QNRF), a member of Qatar Foundation. This work was also made possible in part by [NPRP-EP] under Grant Number [NPRP X - 100 - 2 - 024]. Its contents are solely the responsibility of the author and do not necessarily represent the official views of the Qatar National Research Fund. The statements made herein are solely the responsibility of the author.

NOMENCLATURE

| | |
|------|---|
| ALD | Atomic Layer Deposition |
| DRM | Dry Reforming of Methane |
| POX | Partial Oxidation (of Methane) |
| SMR | Steam Methane Reforming |
| TPSR | Temperature Programmed Surface Reaction |

TABLE OF CONTENTS

| | Page |
|---|------|
| ABSTRACT | ii |
| DEDICATION | iii |
| ACKNOWLEDGMENTS | iv |
| CONTRIBUTORS AND FUNDING SOURCES | v |
| NOMENCLATURE..... | vi |
| TABLE OF CONTENTS..... | vii |
| LIST OF FIGURES..... | x |
| LIST OF TABLES | xiv |
| 1. INTRODUCTION TO DRY REFORMING OF METHANE (DRM) | 1 |
| 1.1. Catalyst Challenge | 5 |
| 1.2. Process Challenge | 7 |
| 1.3. Multi-scale approach of this work | 9 |
| 2. ALD COATED CATALYSTS FOR DRY REFORMING OF METHANE..... | 12 |
| 2.1. Using pulse chemisorption to study Methane Reforming catalysts | 13 |
| 2.1.1. Factors affecting chemisorption | 15 |
| 2.2. Methodology..... | 18 |
| 2.2.1. ALD Catalyst Synthesis | 18 |
| 2.2.2. H ₂ -CO Pulse Chemisorption Technique to measure in-situ dispersion | 19 |
| 2.2.3. Sintering Protocol..... | 23 |
| 2.2.4. High-Resolution Transmission Electron Microscopy..... | 24 |
| 2.3. Results of the chemisorption study | 25 |
| 2.3.1. TEM Imaging Results..... | 33 |
| 2.3.2. Comparing TEM and Chemisorption Results | 38 |
| 2.3.3. DRM performance Data..... | 40 |
| 2.3.4. Conclusions..... | 42 |
| 3. PRETREATMENT METHODS FOR ALD CATALYST | 44 |
| 3.1. Design of Experiments Study..... | 44 |
| 3.1.1. BET and Activity Results for DOE study..... | 46 |

| | |
|---|-----|
| 3.2. TPSR as means of activating ALD catalyst..... | 49 |
| 3.2.1. TPSR Protocol | 52 |
| 3.2.2. TPSR Study – Catalyst Performance and TGA Results..... | 54 |
| 3.2.3. TPSR Study – Images from SEM, TEM and Raman | 61 |
| 3.2.4. Parameters affecting the TPSR phenomenon | 71 |
| 3.2.5. Effect of TPO after TPSR..... | 73 |
| 3.2.6. Conclusions..... | 75 |
| 4. EMISSIONS OF SYNGAS PRODUCTION AND LCA STUDY FOR DRM..... | 77 |
| 4.1. Literature Review..... | 77 |
| 4.2. Major sources of CO ₂ Emissions in Syngas Production – LCA Scope..... | 79 |
| 4.2.1. Upstream emissions of natural gas..... | 81 |
| 4.2.2. Reformer Duty | 81 |
| 4.2.3. Oxidant production..... | 81 |
| 4.2.4. Catalyst Regeneration | 82 |
| 4.2.5. Catalyst Preparation..... | 83 |
| 4.2.6. CO ₂ production in reforming reactions | 83 |
| 4.3. Optimization Model..... | 84 |
| 4.3.1. Reformer Modeling Equations | 84 |
| 4.3.2. Optimization Model Formulation..... | 86 |
| 4.3.3. Comparing cost of syngas production | 91 |
| 4.4. Results | 92 |
| 4.4.1. Conventional Reforming Technologies | 94 |
| 4.4.2. Dry Reforming of Methane | 95 |
| 4.4.3. Parallel Combinations..... | 96 |
| 4.5. Conclusion..... | 98 |
| 5. NOVEL TECHNOLOGIES FOR DRM PROCESSES..... | 99 |
| 5.1. DRM + COSORB..... | 99 |
| 5.2. DRM + H ₂ from external source | 102 |
| 5.3. Potential for integration of DRM+COSORB process in an industrial city..... | 104 |
| 5.3.1. Processes requiring H ₂ /CO ratio ~ 2 | 104 |
| 5.3.2. Processes requiring H ₂ /CO ratio ~ 1 | 105 |
| 5.3.3. Processes requiring H ₂ /CO ratio ~ 0 | 108 |
| 5.4. Carbon footprint and Operating Costs for Methane Decomposition | 110 |
| 5.5. Conclusion..... | 113 |
| 6. CONCLUSIONS AND FUTURE WORK..... | 115 |
| REFERENCES..... | 118 |

| | |
|---|-----|
| APPENDIX A RGA SETUP, MS AND GC CALIBRATION | 131 |
| APPENDIX B EFFECT OF DILUENT SAND ON CATALYTIC ACTIVITY | 135 |
| APPENDIX C PATENT APPLICATION – PROCESSING METHANE FOR SYNGAS PRODUCTION WITH REDUCED CO ₂ EMISSIONS..... | 151 |

LIST OF FIGURES

| | Page |
|--|------|
| Figure 1 - Current status of utilization of natural gas | 1 |
| Figure 2 –Methane Reforming Technologies | 3 |
| Figure 3 - Deactivation pathways of Ni catalysts. Reprinted from [22] | 5 |
| Figure 4 – Strategies for catalyst design..... | 6 |
| Figure 5 - Commercial Catalyst Bulk Particle Size Distribution..... | 7 |
| Figure 6 - Different starting points for each reforming technology | 8 |
| Figure 7 – Multi-scale approach to DRM..... | 10 |
| Figure 8 - H ₂ -CO Sequential Chemisorption Protocol. Reprinted from [22] | 19 |
| Figure 9 – RGA responses of CO (m/z=28) and H ₂ (m/z=2) during the CO chemisorption step. Reprinted from [22]..... | 20 |
| Figure 10 – Experimental Setup for DRM reaction. Modification for in-situ chemisorption highlighted in red. Reprinted from [22]..... | 24 |
| Figure 11 - H ₂ desorbed, μmol/g _{cat} , during H ₂ -CO chemisorption, at specific intervals during 40h of DRM. Right pane: After TPO at the end of 40 hours. Reprinted from [22]..... | 26 |
| Figure 12 – Change in Ni Dispersion for Commercial and 5-ALD catalysts with Time-on-Stream; equations show the relative rates of change in dispersion. Reprinted from [22] | 29 |
| Figure 13 – Pulse injection trends comparing CO moles consumed and H ₂ moles desorbed per pulse at various intervals during sintering of the Commercial catalyst. (a) before DRM, (b) after 4 hours (c) 27 hours and (d) 39 hours of DRM. Dotted lines represent data smoothed data. Reprinted from [22]..... | 31 |
| Figure 14 – Comparison of CO moles consumed vs. H ₂ moles desorbed per pulse at various stages of sintering for the 5-ALD catalyst. Dotted lines represent smoothed data. Reprinted from [22]..... | 33 |
| Figure 15 – Comparison of TEM images of Commercial and ALD Ni catalysts before and after DRM of 40 h TOS. (a): fresh, reduced Commercial and EDS | |

| | |
|--|----|
| elemental analysis. (b): TEM, HAADF, Ni EDS mapping for sintered catalysts. Reprinted from [22] | 34 |
| Figure 16 – Normalized particle size distribution as measured from selected TEM images for the different catalyst samples (data-points connected for clarity). Inset: Mean crystallite size comparison of the investigated catalysts before and after 40h DRM. Reprinted from [22]..... | 36 |
| Figure 17 - HR-TEM images of 20-ALD catalyst highlighting the presence of Ni (111), (200) and Nickel Aluminate spinel (511) phases. Data for calculation of d- spacing obtained from reference JCPDS 10-0339 for Nickel Aluminate and JCPDS 04-0850 for Nickel. Reprinted from [22] | 38 |
| Figure 18 – Crystallite size comparison by chemisorption and TEM, before and after DRM reaction for (a) Commercial and (b) 5-ALD catalysts. Reprinted from [22] | 39 |
| Figure 19 - DOE Parameters affecting ALD overcoat ultimately affecting catalyst activity | 45 |
| Figure 20 - CH ₄ consumption rates for two different deposition temperatures (E1-125 °C, E2-300 °C)..... | 47 |
| Figure 21 - H ₂ /CO Ratio | 47 |
| Figure 22 - CH ₄ Activity Profiles for all samples | 48 |
| Figure 23 - Activity of ALD coated catalysts compared with Commercial uncoated catalyst | 49 |
| Figure 24 - Experimental Setup for TPSR..... | 53 |
| Figure 25 – Catalyst Reduction and Reactor Temperature Profile in the TPSR experiment..... | 54 |
| Figure 26 – Comparison of catalytic performance of Commercial and 20-ALD catalysts during TPSR | 56 |
| Figure 27 - Comparing TPSR with Pressure Dilution | 57 |
| Figure 28 - Repeat TPSR Experiments - 1 | 58 |
| Figure 29 - Repeat TPSR Experiments - 2 | 59 |
| Figure 30 - TGA plots for Commercial and 20-ALD catalysts | 60 |

| | |
|---|-----|
| Figure 31 - Differential changes in weights in TGA | 61 |
| Figure 32 - Comparison of SEM images after TPSR..... | 63 |
| Figure 33 - TEM images of catalysts after TPSR..... | 66 |
| Figure 34 – Magnified images and overlap to show that the needle-like structures are from the amorphous overcoated alumina..... | 67 |
| Figure 35 - High-Resolution Images of carbon morphology on Commercial and 20-ALD catalyst | 69 |
| Figure 36 - Raman Shift for spent catalysts - Commercial and 20-ALD | 70 |
| Figure 37 - CH ₄ Activity - after TPSR+TPO+Reduction..... | 74 |
| Figure 38 - H ₂ /CO ratio - after TPSR+TPO+Reduction..... | 75 |
| Figure 39 - Workflow in TPSR experiments | 76 |
| Figure 40 – Schematic showing major sources of emissions considered in the study..... | 80 |
| Figure 41 – Solution Approach. Reprinted from [40]..... | 89 |
| Figure 42 – Optimization variables in single reformer (Cases 1-4) and parallel reformers (Cases 5a, 5b). Reprinted from [40] | 91 |
| Figure 43 – Carbon footprint of syngas production for various processes. Reprinted from [40]..... | 93 |
| Figure 44 – Cost of syngas production by various processes. Reprinted from [40] | 94 |
| Figure 45 - CuAlCl ₄ molecule [136]..... | 100 |
| Figure 46 – Proposed DRM+COSORB Process. Reprinted from [40] | 101 |
| Figure 47 - Comparison of POX/ATR and DRM+COSORB (Captured CO sold as feedstock case) for syngas ratio of 2 and 3. Reprinted from [40] | 102 |
| Figure 48 - DRM and Ethylene Plants before and after mass integration. Reprinted from [40] | 103 |
| Figure 49 - DRM Process utilized for different pathways based on H ₂ /CO requirement . | 104 |
| Figure 50 - DRM for H ₂ /CO=2..... | 105 |

| | |
|--|-----|
| Figure 51 - O/P ratios for different H ₂ /CO ratio syngas. Reprinted from [141] | 106 |
| Figure 52 - Utilization of DRM to produce CO as feedstock for Propiolactone..... | 108 |
| Figure 53 - Estimated production cost of CO..... | 109 |
| Figure 54 - Carbon footprint of CO production | 110 |
| Figure 55 – Carbon footprint Comparison for DRM (higher syngas ratios with coke formation allowed). Reprinted from [40]..... | 111 |
| Figure 56 – Operating Cost Comparison for DRM (higher syngas ratios with coke formation allowed). Reprinted from [40]..... | 112 |
| Figure 57 - Residual Gas Analyzer. Reprinted from [149] | 131 |
| Figure 58 - Suggested workflow for using Mass Spec in experiments | 132 |
| Figure 59 - Typical Calibration Chart for PA ratio v/s Molar ratio | 134 |
| Figure 60 - Experimental Setup | 135 |
| Figure 61 - Data Analysis for 2.5 mg Riogen, 25 mg sand, <53 μm range | 137 |
| Figure 62 - CH ₄ rate with Space Velocity (ml/min/g _{cat}) | 138 |
| Figure 63 - CH ₄ Conversion with Space Velocity (ml/min/g _{cat}) | 138 |
| Figure 64 - Choosing the right conditions based on objective..... | 142 |

LIST OF TABLES

| | Page |
|---|------|
| Table 1 – DOR Calculation for Commercial catalyst. Reprinted from [22] | 21 |
| Table 2 – DOR Calculation for 5-ALD catalyst. Reprinted from [22] | 22 |
| Table 3 – ICP-OES Results and mass gain from ALD. Reprinted from [22]..... | 23 |
| Table 4 – Catalyst performance data for ~40 h TOS of DRM. Reprinted from [22] | 41 |
| Table 5 - Experimental Design | 45 |
| Table 6 - BET Results of 20-ALD catalyst..... | 46 |
| Table 7 - Comparison of coke formation rates in TGA experiment | 61 |
| Table 8 - Intensity of Raman bands | 70 |
| Table 9 - Factors affecting TPSR behavior in ALD catalysts (Green: TPSR works, Red: TPSR does not work, Blank: untested) | 72 |
| Table 10 – Carbon footprint for oxidant production. Reprinted from [40] | 82 |
| Table 11 – Cases considered for study. Reprinted from [40] | 90 |
| Table 12 – Feedstock Costs. Reprinted from [40] | 92 |
| Table 13 – Comparison of Model solutions for syngas ratio = 2.25. Reprinted from [40] .. | 97 |
| Table 14 – Comparison of Model solutions for syngas ratio = 1.5. Reprinted from [40] | 98 |
| Table 15 - Estimation of the COSORB plant capacity | 105 |
| Table 16 - Prices considered for MISR calculation..... | 107 |
| Table 17 - MISR Estimation for C ₂ -C ₄ Olefins | 108 |
| Table 18 - Results from Optimization Model for CO ₂ /CH ₄ =3..... | 109 |
| Table 19 - Details of short TOS runs..... | 136 |
| Table 20 - Different Objectives, Different Conditions..... | 140 |

| | |
|--|-----|
| Table 21 - Operating Conditions for Future Testing..... | 141 |
| Table 22 - Proposed set of kinetic experiments (more runs will be added as needed to vary the partial pressure span of species)..... | 143 |

1. INTRODUCTION TO DRY REFORMING OF METHANE (DRM)

Natural gas is a major source of energy globally. In 2018, about 31% of the total energy demand of the United States was met by natural gas alone [1]. Natural gas consists mainly of methane (>85%) with ethane and other some higher hydrocarbons. Globally, there are primarily three ways of utilization of natural gas [2], as shown in Figure 1. Most of the use, about 90%, is for combustion in furnaces to either heat or to produce steam, which generates electricity.

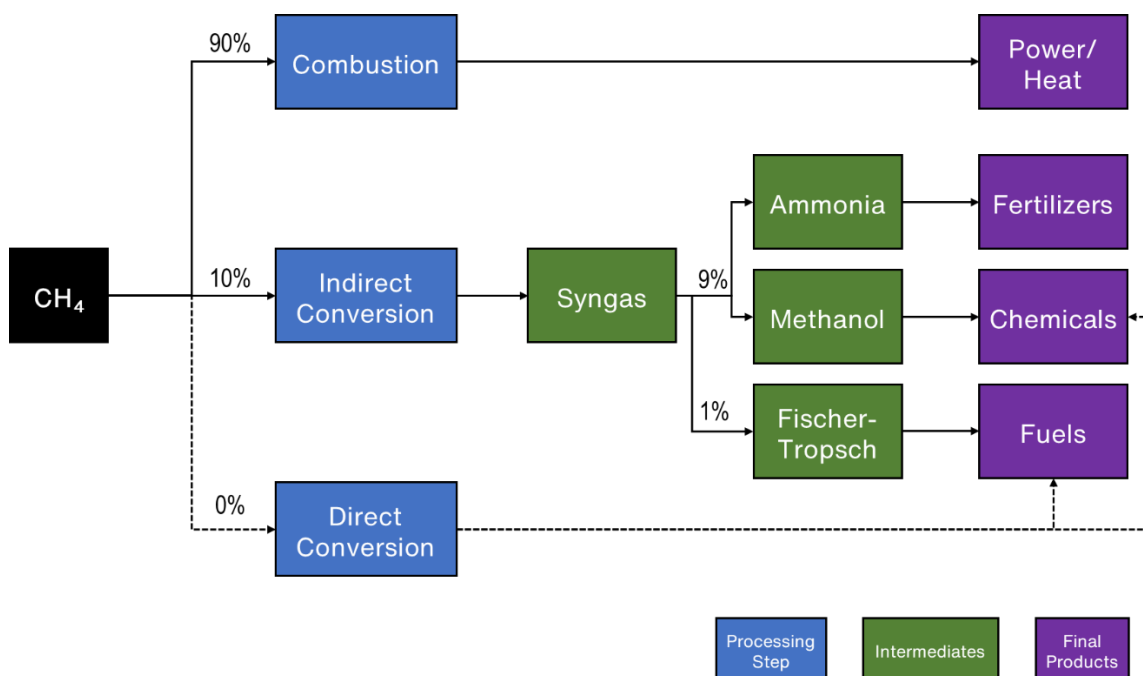


Figure 1 - Current status of utilization of natural gas

About 10% of the natural gas is used as a feedstock. However, methane is a relatively stable compound. The bond energy of the C-H bond in methane is 415 kJ/mol [3]. This makes methane relatively unreactive. But, by converting it to the more active mixture of carbon monoxide and hydrogen, it is easier to then just change catalyst and operating conditions for further downstream processing. Natural Gas Reforming refers to the process of activating methane. This mixture of CO and H₂ is known as Syngas and syngas-based routes are called

Indirect Conversion routes. Syngas is one of the most versatile intermediates in the chemical industry that can be used to monetize natural/shale gas to produce a variety of chemicals and petrochemicals [4]–[8]. Furthermore, syngas can be converted into liquid fuels through the Fischer-Tropsch (FT) process. Direct conversion to fuels and products is desirable but the conversions are too low to compete with syngas based routes [9]. Hence, syngas will continue to remain an essential intermediate of the chemical industry for many decades to come. And this makes it necessary to exhaust any available methods to reduce the carbon footprint of these highly energy-intensive processes to produce syngas.

There are primarily three industrial processes to produce syngas. Steam Methane Reforming (SMR), Partial Oxidation of Methane (POX), and Auto Thermal Reforming (ATR). In SMR, steam is used as the oxidant to produce syngas, and from stoichiometry, 3 moles of H₂ are produced per mole of CO. The molar ratio of H₂ to CO is also called Syngas Ratio and is an important parameter, as it decides the downstream application of the syngas produced. Sometimes, another stoichiometric ratio, R is used which is given by:

$$R = \frac{H_2 - CO_2}{CO + CO_2}$$

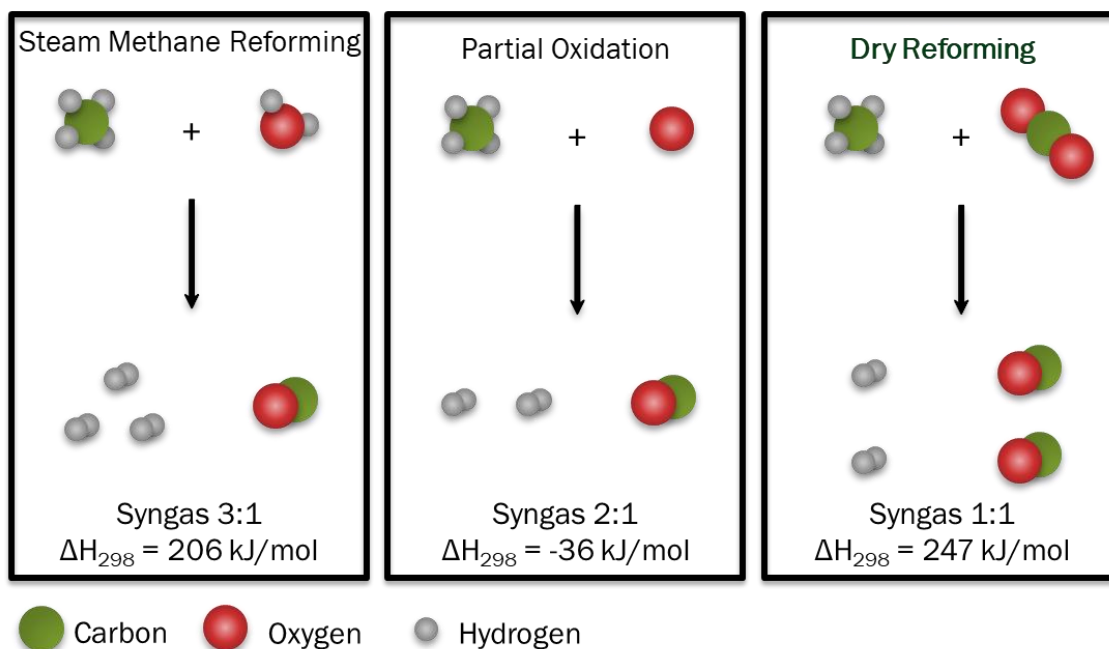
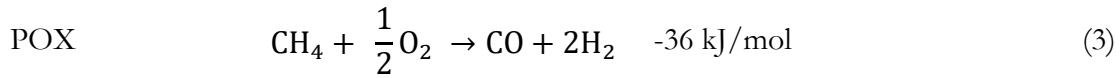
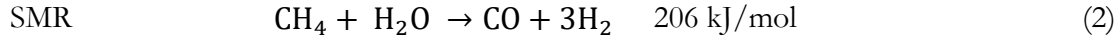


Figure 2 –Methane Reforming Technologies

In the POX technology, oxygen is used as the oxidant. The pure O₂ is obtained by liquifying air in an Air Separation Unit (ASU). Pearl GTL has the world's largest oxygen plant with a capacity of 28,800 tons per day to produce O₂ for syngas production. In an auto thermal reformer, a mixture of O₂ and steam is used. It is called auto thermal since the partial oxidation is exothermic; the idea is that it generates energy for the reaction itself. Qatar, having the world's third-largest natural gas reserves at ~ 872 tcf (trillion cubic feet) [10], has various syngas production technologies in operation in the industrial cities of Ras Laffan and Mesaieed. The Pearl GTL and Oryx GTL plants in Ras Laffan utilize Partial Oxidation (POX) and Auto-Thermal Reformer (ATR), respectively, for their syngas production which is then used to produce synthetic fuels via the FT reaction. Other petrochemical plants in Mesaieed utilize Steam methane reforming (SMR) to produce syngas of high H₂/CO ratio which is required for the production of various petrochemicals. As shown in Figure 2, Dry Reforming of Methane (DRM) refers to the reaction between CH₄ and CO₂ to produce syngas as shown:



As per the stoichiometry of the DRM reaction, the syngas produced has an H₂/CO ratio of 1. This is much lower than that obtained by SMR (≥ 3) and POX (~ 2). SMR uses steam and POX uses pure oxygen as the oxidant, and the respective reactions are as follows:



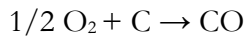
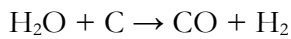
The stoichiometric syngas ratio is 3 in SMR, 2 in POX, and 1 in DRM. And this is a deciding factor in the applicability of these processes. DRM is a very attractive reaction as it utilizes a greenhouse gas, CO₂ and produces a valuable intermediate syngas. Greenhouse Gases (GHGs) are those gases that trap heat in the atmosphere resulting in the rise of average global temperature. GHGs are considered the most significant cause of global warming [11]. The major greenhouse gases are carbon dioxide (CO₂), methane (CH₄), nitrous oxide (N₂O), and other fluorinated gases. According to the US Environmental Protection Agency (EPA) estimates for 2015, CO₂ is responsible for 82% of the total greenhouse gas emissions [12]. This is also supported by the Intergovernmental Panel on Climate Change (IPCC) Report for 2014, which stated that CO₂ constituted about 76% of anthropogenic emissions in 2010 [13]. Out of the various solutions being proposed to mitigate the CO₂ problem [14]–[16], Carbon Capture and Utilization (CCU) processes are one of the promising pathways.

DRM has the potential of being integrated with existing syngas production infrastructure. Since DRM utilizes CO₂ as the oxidant, it helps gain a credit in the CO₂ balance of the process, which is not available for current technologies of SMR and POX. Additionally, DRM has gained interest in recent years due to the requirement to process high CO₂ content natural gas feeds [17], [18]. Towards commercial applicability, DRM faces three main challenges. Firstly, the energy requirement of DRM (247 kJ/mol) is higher than that of SMR (206 kJ/mol), which is currently the leading technology to produce hydrogen and hydrogen-rich syngas in the industry. Secondly, the conditions of DRM promote coke formation at a faster rate and hence catalyst design is crucial. Most of the literature on DRM is aimed at finding

coke resistant catalysts. The third challenge facing DRM is that the produced syngas has a low H_2/CO ratio of around 1, which limits its application for downstream processes. This dissertation uses a multi-scale approach to address the two main challenges of the process – Catalyst Deactivation and Life Cycle Analysis. They are described in further detail in the next two sections and how the work presented in this dissertation helps propose possible solutions to mitigate these challenges.

1.1. Catalyst Challenge

In the conventional SMR and POX, steam and oxygen help to remove the surface carbon by the reaction to CO by the following reactions:



Hence, this helps in reducing the catalyst deactivation by coke formation. However, in a pure DRM reaction, the only oxidant is CO_2 , which is considered as a soft oxidant. Various catalyst designs have been suggested in the literature for DRM application [19]–[21]. There are two primary modes of deactivation for catalysts in DRM systems – carbon deposition and metal sintering, as shown in Figure 3.

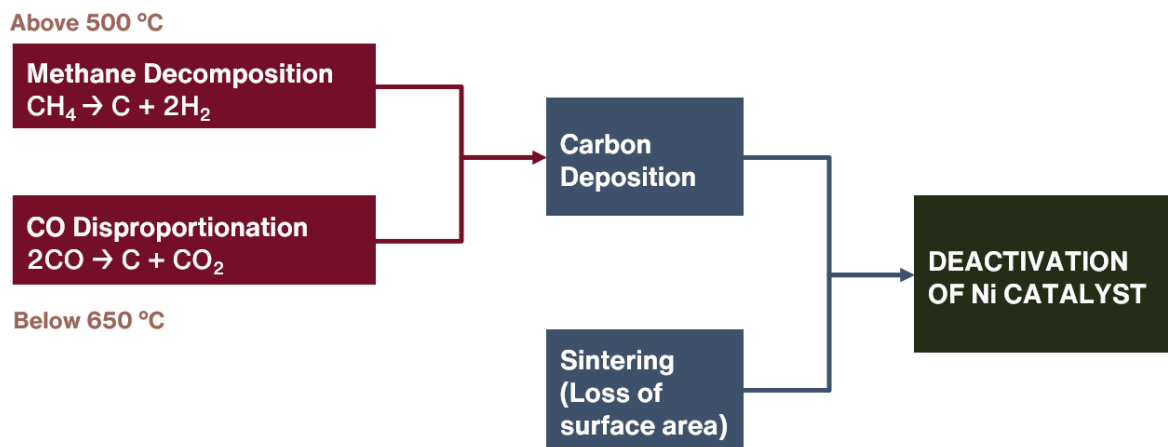


Figure 3 - Deactivation pathways of Ni catalysts. Reprinted from [22]

Adding promoters like cerium, lanthanum, etc. is a popular method to increase catalyst stability [21], [23]–[25]. The promoters change the kinetics of pathways and preferentially speed up reactions towards DRM and slow down the coke forming reactions. Another approach is to change the support material to increase metal-support interactions. Pyrochlores [20] are crystalline metal oxides and they have been used by several research groups. They have the general formula, $A_2B_2O_7$, and the oxygen is assumed to be interchangeable with the oxygen in CO_2 . This increases the oxygen concentration on the catalyst surface thereby enhancing coke removal rates.

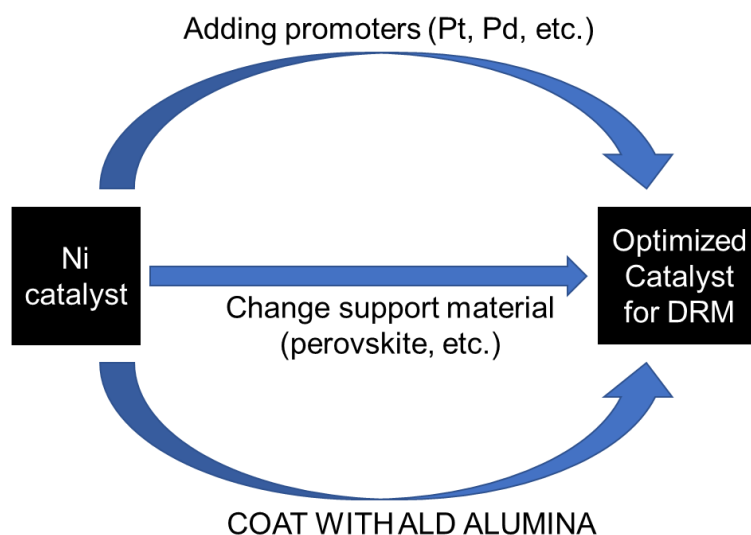


Figure 4 – Strategies for catalyst design

In this work, the route of promoters was completely avoided. Instead, an alternative approach called Atomic Layer Deposition (ALD) has been used [26]. In an ALD process, a precursor is used to deposit the substrate onto the catalyst surface. Tri-methyl aluminum (TMA) is the precursor to deposit alumina. The alumina overcoat helps stabilize the Ni active metal and protects it from sintering. The benchmark catalyst in all the work presented in this dissertation is a 20% Ni on Al_2O_3 catalyst obtained from a commercial supplier, Riogen [27]. The powder procured has a product size distribution as shown in Figure 5. The catalyst is referred to as ‘Commercial,’ and any modified version of the catalyst will be compared with this benchmark.

The advantage of using a Commercial catalyst as opposed to a model catalyst prepared in-house is that the results obtained here will be more readily transferable to scale-up studies than a model catalyst. Model catalysts with very low loading are better suited for studying fundamental phenomena on the catalyst surface. The additional advantage of using ALD is the use of a cheaper material like alumina when compared to more expensive noble metals. Alumina costs around \$600/ton [28] whereas platinum costs upwards of \$32,000/kg [29].

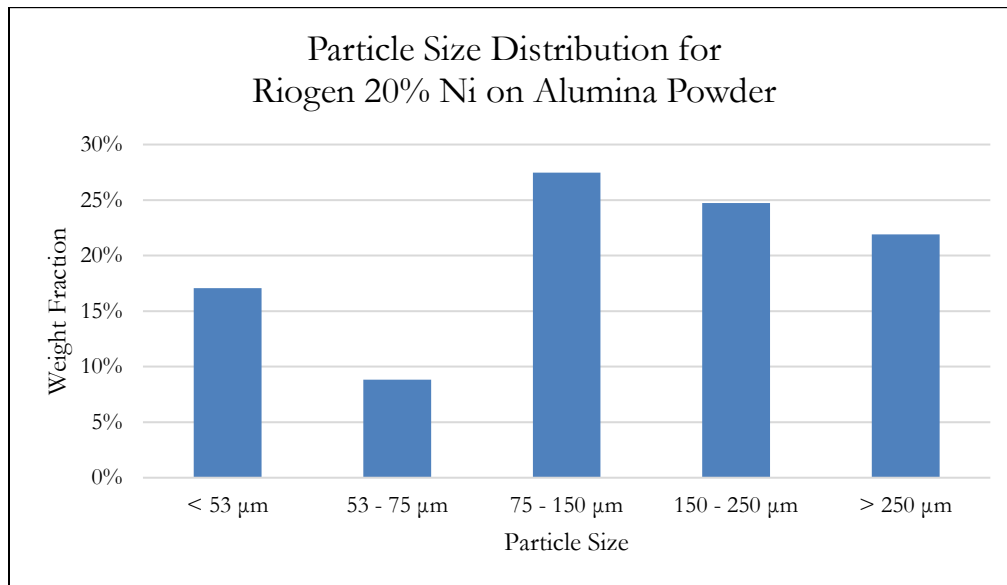


Figure 5 - Commercial Catalyst Bulk Particle Size Distribution

1.2. Process Challenge

One of the main issues in comparing the environmental impact of DRM and other conventional processes like SMR, ATR, and POX is that each of these processes produces syngas of different ratios (SMR ~3.5 and above, ATR ~2.5, POX ~1.9, DRM ~1). SMR gets a head start as the oxidant contains 1 mole of H₂ to begin with, whereas all hydrogen in DRM syngas comes from methane. Hence, the starting point of all these competing processes is different. Since these technologies produce different qualities of syngas, a direct comparison among these is not equitable without considering the quality and quantity of the produced syngas. From a life cycle assessment (LCA) perspective, choosing the functional unit becomes an issue in this case, because it is challenging to get the same quality of product from each of

these processes. Different syngas production networks can still be compared on the basis of carbon footprint and operating costs, provided the final blended syngas has the same H_2/CO ratio and the natural gas feed remains the same in those cases.

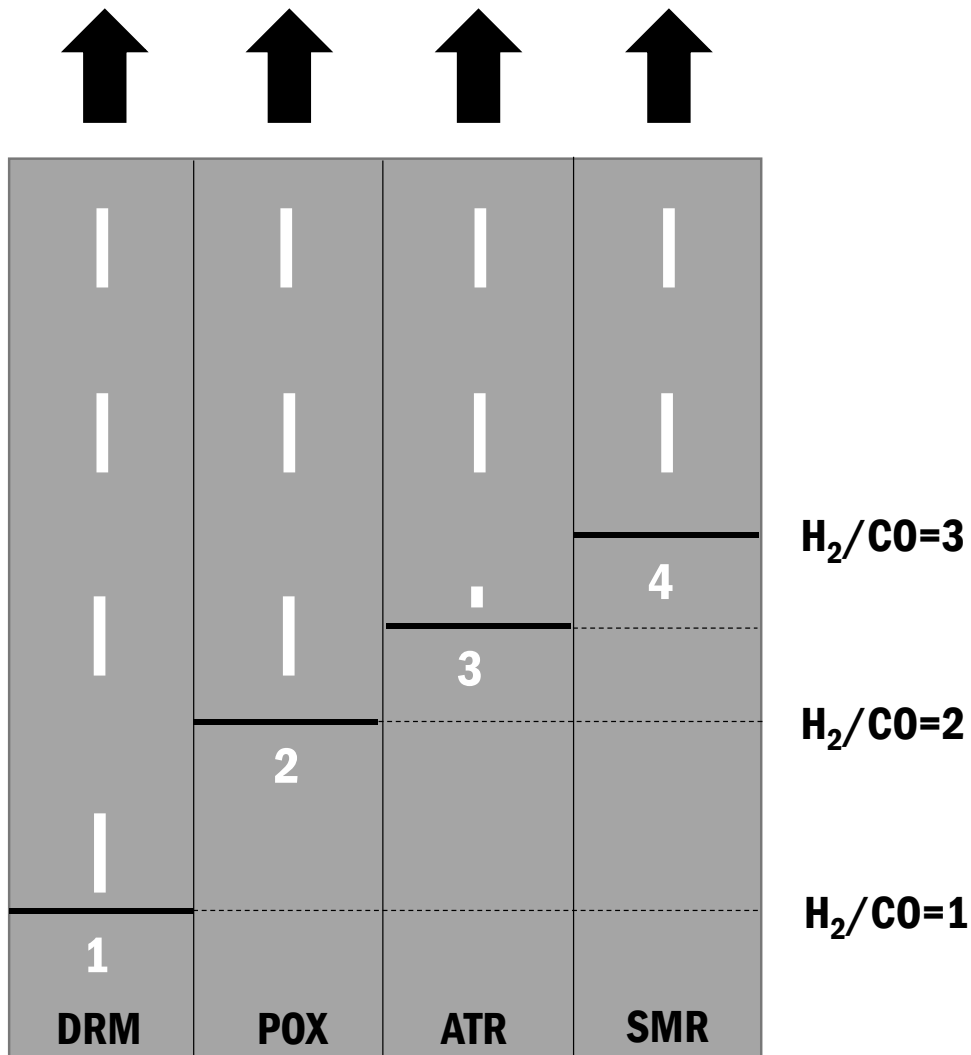


Figure 6 - Different starting points for each reforming technology

Some researchers have suggested using a combination of oxidants and termed it as Tri-reforming [30], [31]. But doing so has a minimal effect on the overall carbon footprint of the syngas production process [32]. Moreover, having all oxidants together requires CAPEX for each of these oxidants thereby affecting the process economics. Some commercial SMR

flowsheets [33] show a CO₂ separation unit and feed it back to the reformer inlet to adjust the syngas ratio. The CO₂ might either do the DRM or reserve WGS. However, this cannot be considered as the DRM intended here since there is no CO₂ fed from outside the process. Internal recycling does not help the overall mass balance and hence the CO₂ utilization potential of the DRM is not fulfilled. We would ideally want to use an external CO₂ stream, a pure stream or a concentrated CO₂ stream captured a flue gas stream. Hence, when comparisons are made, they will be made with commercial benchmarks of SMR and POX, and not with Tri-reforming. The objective is to ascertain if the DRM reaction can be used as an alternative to conventional syngas production technologies. Hence, the focus is on trying to understand what the maximum potential of the DRM reaction is. An Optimization-based approach is used to evaluate different reforming options. Promising pathways are selected and studied in further detail. To produce syngas with high H₂/CO ratio by DRM, it was found that the best approach is to capture CO from the DRM syngas by any separation process, thereby enhancing the syngas ratio. Various scenarios that include this process combination are studied and analyzed in terms of overall carbon footprint and operating costs.

1.3. Multi-scale approach of this work

A unique aspect of this work is the multi-scale approach employed to address the research problem. The results from catalyst design impact the process LCA and the optimization results from the LINGO model will decide the process conditions for the catalytic studies as shown in Figure 7. Catalyst modification and testing campaigns will help establish the actual conversion and stability information. This dissertation is broadly divided into two parts: the first part (chapters 2 and 3) focuses on DRM catalysis using ALD catalysts and the second part (chapters 4 and 5) deals with the synthesis of processes for DRM which have the potential of reduction of carbon footprint.

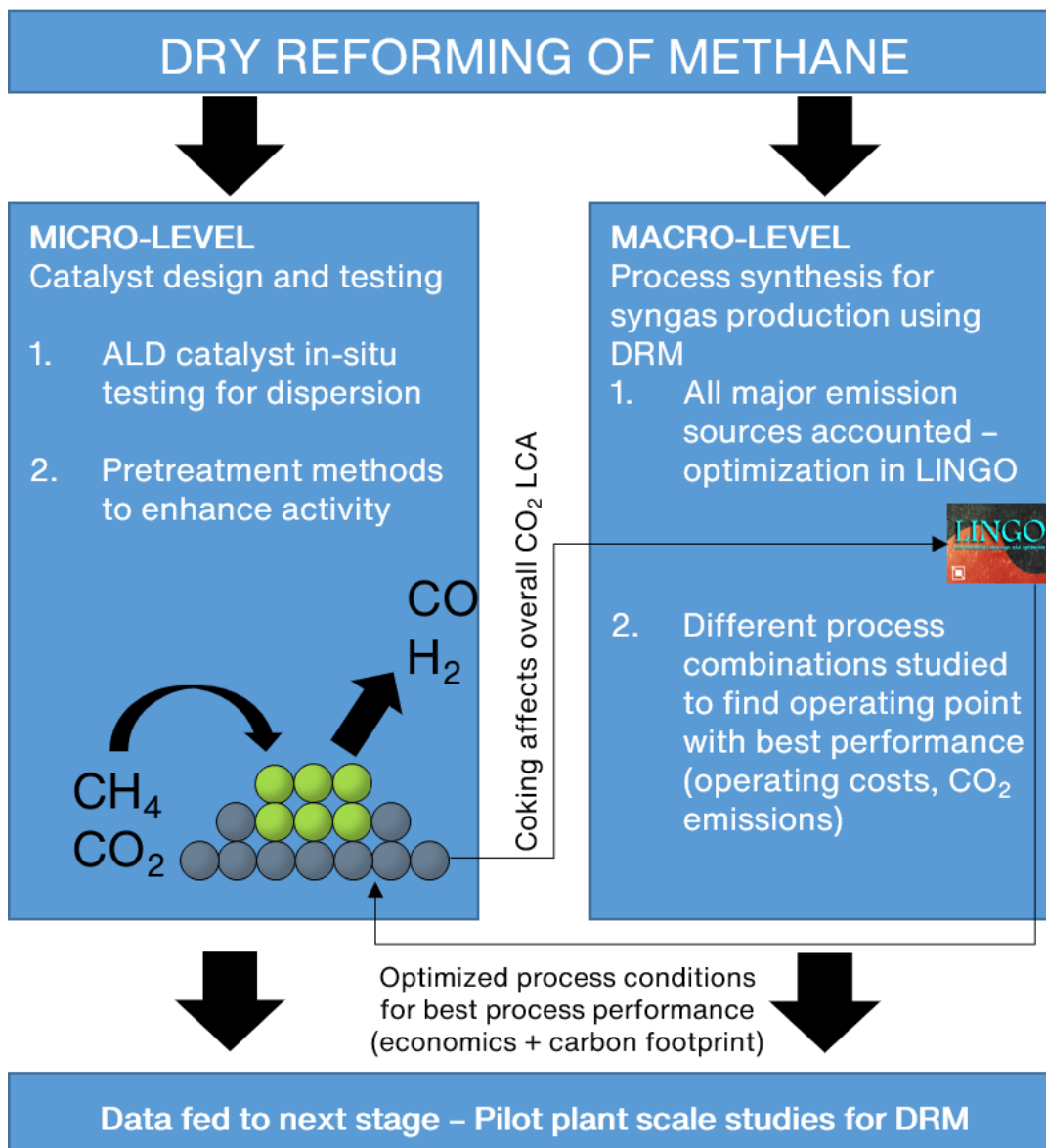


Figure 7 – Multi-scale approach to DRM

In this dissertation, Chapter 2 deals with the performance of 5-ALD catalysts, the challenge of using ALD catalysts and future pathways, and prospects to use ALD catalysts. In chapter 3, various parameters of the ALD annealing process are investigated for their effect on overcoat porosity. An alternative annealing process for the 20-ALD catalyst is studied which has marked improvement in the catalyst performance. As described earlier, catalysis is not the only challenge in DRM; there are also questions around the actual impact on CO₂ emissions.

Chapter 4 describes the LCA model and approach used to investigate different pathways for syngas production. Chapter 5 deals with DRM assisted processes that have the potential for reducing overall CO₂ emissions and the associated process economics aspects.

2. ALD COATED CATALYSTS FOR DRY REFORMING OF METHANE¹

The ability to characterize industrial catalytic systems has undergone a tremendous evolution over the last few decades as a result of advances in analytical techniques that offer rapid analysis without compromising measurement accuracy [34]–[36]. Metal dispersion and particle size are two metrics that are critical for the development of catalysts with improved activity and stability. Determining the change in metal dispersion, i.e., the degree to which an active metal is evenly distributed over the available surface area of a support, is considered a good indicator of catalyst stability [37], [38]. Specifically, higher active metal dispersion is generally associated with increased metal-support interaction, which can minimize the agglomeration of active metal sites by sintering. On the other hand, the potential for sintering typically decreases as the overall exposed metal surface area decreases. Sintering is primarily a thermally induced deactivation phenomenon caused by an increase of metal crystallite size, leading to a loss of surface area and, consequently, catalytic activity [39]. In addition to temperature, the reaction atmosphere, metal type, and promoters are some of the factors which can affect rates of sintering. In this study [22], a monometallic Ni catalyst supported on alumina is investigated. Sintering is induced here under a DRM atmosphere, which consists of 1:1 CH₄:CO₂ feed diluted in an inert gas, and contains H₂, CO, and H₂O as products of the DRM and reverse water gas shift (RWGS) reactions. The catalyst and conditions were chosen because of their relevance to the DRM process.

The DRM process is an important and widely studied reaction which involves the reduction of CO₂ with CH₄, producing synthesis gas (CO+H₂). Previous work done by our group [40] has shown that in specific process scenarios, the DRM process has the potential of reducing the overall carbon footprint of syngas production at competitive operating costs. However, one of the main practical challenges towards the commercialization of this technology is the rapid deactivation of catalysts due to coke formation and sintering.

¹ A major portion of this chapter has been published in International Journal of Hydrogen Energy 45 (2020) 12835-12848 Copyright 2020 Elsevier. [22]

Of the various approaches to mitigate these challenges, designing improved, sinter-resistant catalysts via Atomic Layer Deposition (ALD) is a relatively new one. ALD is widely employed in the semiconductor fabrication industry and has now attracted the interest of the catalysis community [26], [41]. ALD is a thin film deposition technique using vapor phase precursors and has proven benefits over conventional chemical vapor deposition (CVD) due to its capacity to deposit highly conformal overcoats with precise atom-scale thickness and desired composition. From a process perspective, ALD is a cyclic, self-limiting set of surface chemical deposition reactions. Ni catalysts treated in sequences of tri-methyl aluminum (TMA) then H₂O pulses have been shown to undergo slower deactivation than the analogous uncoated catalysts [42]. Baktash et al. [43] showed that a model unsupported NiO DRM catalyst overcoated with 5 TMA/H₂O ALD cycles undergoes limited catalyst deactivation via sintering while sustaining exceptional activity, especially at higher temperatures of around 800 °C. In an ALD coated catalyst, access to active sites is facilitated by increasing the porosity of this ALD overcoat by high-temperature annealing, as shown by previous studies [43]–[45]. In this contribution, the inhibition of sintering via ALD coating is investigated by quantifying the changes in the dispersion of a commercial Ni/Al₂O₃ catalyst during the DRM reaction. There have been many studies investigating the evolution of crystallite size and dispersion for Ni catalysts under sintering conditions [46], [47]. Frequently used techniques for measuring Ni ‘crystallite’ or ‘particle’ size and dispersion are XRD (X-ray Diffraction), H₂ chemisorption, and TEM (Transmission Electron Microscopy). While other techniques can be employed independently or to complement these methods, including SAXS (Small Angle X-ray Scattering) [48] and magnetometer analysis [49], they are far less common. Mustard and Bartholomew [50] provide an informative summary of the pros and cons of conventional measurement techniques viz, chemisorption, XRD, and TEM.

2.1. Using pulse chemisorption to study Methane Reforming catalysts

Sintering of Ni catalysts for steam reforming systems has been investigated by Sehested et al. [51], using sulfur chemisorption as a means to determine Ni surface area. One drawback of this method is the regeneration of these catalysts after sulfur chemisorption, a tedious process requiring steaming at high temperatures of above 600 °C, which can further affect Ni

dispersion [52]. The sintering of the catalysts in this study was achieved without the introduction of methane. Different ratios of $\text{H}_2\text{O}/\text{H}_2$ were introduced, simulating oxidizing and reducing atmospheres, respectively. An advantage of this approach is that it excludes the effect of carbon deposition on deactivation and targets only the phenomenon of sintering. The primary challenge concerning methane dry reforming systems is that both reactants, CH_4 and CO_2 , are carbonaceous species, and therefore varying H_2O , and H_2 partial pressures would be ineffective in simulating sintering in an actual DRM atmosphere. Moreover, the H_2 and H_2O partial pressures in a dry reforming atmosphere are lower than in steam reforming, and any steam generated is due to the reverse water-gas shift reaction. Therefore, typical DRM conditions were employed for the present sintering study. It is important to note that both carbon deposition and sintering will contribute toward catalyst deactivation in this study (see Figure 3), and thus, the results must be interpreted within this context. While the deposited carbon may affect chemisorption results, TEM imaging of the used catalyst can provide visual confirmation of sintering regardless of carbon deposits.

Although TEM is becoming increasingly accessible, chemisorption is typically a more expeditious approach to measure Ni crystallite size. Chemisorption rapidly measures the available surface area of an entire sample, rather than requiring an extrapolation from an image of a small fraction of the catalyst which may or may not be representative. A key differentiating feature of chemisorption is its capacity to not only measure the extent of sintering before and after a reaction, but it also to permit in-situ characterization, without removing a sample from the reactor or exposure to air, and with minimal equipment modification.

Although H_2 is typically considered the probe molecule of choice for titrating surfaces of Ni catalysts [50], for many applications achieving the conditions most suited for H_2 chemisorption depends on several factors viz. experimental setup, ambient conditions, catalyst properties, to name a few. In this study, we utilize the phenomenon of H_2 displacement by CO to probe the reduced Ni crystallite surface over the course of the DRM reaction. The displacement of pre-adsorbed H_2 by CO on Nickel films has been investigated

in the past [53]–[56], and the principle extended to determine the surface area of supported Nickel systems [57]. It is believed that the transformation of adsorbed H into an H-CO surface complex species precedes the rapid desorption of H₂ molecule from the Ni surface on CO addition. This surface complex has a lower surface binding energy than typically adsorbed H₂, which promotes the facile desorption of H₂.

This sequential H₂-CO chemisorption approach as described above is applied in the current study to reveal dynamic changes in metal dispersion with time-on-stream (TOS) of over ~40 h of the DRM reaction using a commercial, industrial grade 20 wt.% (nominal) Ni-Al₂O₃ catalyst. The same procedure is followed for the ALD-coated catalysts, which are over-coated with varying cycles of TMA-H₂O ALD. Furthermore, trends in sequential chemisorption pulses for the catalysts are analyzed. Particle size obtained by TEM imaging of the fresh and used catalysts allows for unambiguous quantification of crystallite size changes.

2.1.1. Factors affecting chemisorption

Prior to the application of the unconventional H₂-CO sequential chemisorption technique to titrate Ni surfaces, several attempts were made to utilize standard H₂ pulse chemisorption as a means to track catalyst sintering in-situ. Although H₂ is typically considered the probe molecule of choice for Ni surfaces, contrary to expectations, almost no H₂ uptake was detected on the reference industrial Ni catalyst following standard literature chemisorption protocols [50]. Subsequent Temperature Programmed Desorption did not liberate detectable H₂ either, confirming the inadequacy of this approach for the system under investigation. In troubleshooting this issue, a reference material of known dispersion, 0.5 wt% Pt/Al₂O₃, was loaded into the reactor with the intention of performing CO pulse chemisorption. Interestingly, as CO pulsed through the catalyst bed, the RGA mass spectrometer detected H₂ being displaced from the surface of the catalyst, in addition to the expected CO adsorption. The dispersion was calculated separately using the total volume of CO adsorbed as well as H₂ desorbed. The equation for estimation of percent metal dispersion via either CO chemisorption or H₂ desorption is of the form:

$$\%D = SF \times \left(\frac{V_{gas}}{V_{STP}} \right) \times \left(\frac{MW}{m\% \times m} \right) \times 100 \quad (4)$$

where,

SF = Stoichiometric factor of CO (1) or H₂ adsorption (2) to Ni

V_{gas} = Volume of CO chemisorbed/ H₂ desorbed per gram catalyst, cm³

V_{STP} = CO or H₂ molar volume at STP, cm³

MW = Molecular weight of Ni

$m\%$ = weight % of Ni metal in catalyst

m = mass of catalyst loaded, g

V_{gas} is calculated from the following equations:

$$V_{gas} = V_{pulse} \times \sum_{i=1}^n \left(1 - \frac{PA_i}{PA_{ref}} \right) \quad (5)$$

$$V_{pulse} = V_{loop} \times \frac{273 K}{T_{loop}} \times \frac{P_{loop}}{760 mmHg} \times \frac{C_{gas}}{100} \quad (6)$$

where,

V_{pulse} = volume of gas dosed from the loop, cm³

PA_i = Peak area of pulse i

PA_{ref} = Peak area of reference or saturated pulse

V_{loop} = loop volume, cm³

T_{loop} = Temperature of loop, K

P_{loop} = pressure of gas in loop, mm Hg

C_{gas} = % volume concentration of active gas in the loop

Dispersions estimated by utilizing either CO or H₂ adsorbed volumes were found to be very comparable and matched that of the reported dispersion of the Pt standard. Building on this observation, attempts were next made to reproduce the phenomenon on the Commercial catalyst. However, the phenomenon could not be reproduced under similar conditions, so the temperature of chemisorption was varied (40°C, 60°C, 80°C), as was the concentration of pulsed H₂ (10% and 100% pure), mass, and the sieved-size fraction of the catalyst to ascertain suitable chemisorption conditions. Although not exhaustive, the efficacy of the H₂-

CO chemisorption protocol was tested under these sets of conditions, and consequently, certain trends became evident.

Based on the experimental campaign, the following parameters were found to be influential in obtaining reproducible H₂-CO chemisorption results on the Ni surface, namely temperature, particle size, the partial pressure of the probe molecule, catalyst mass, and pulse volume. Each of these parameters is summarized below.

Ambient and lower than ambient temperatures are generally regarded as favorable for adsorption [58], but for the system investigated here, it was observed that low temperatures might not always produce good chemisorption results. The 60 °C chemisorption temperature was chosen after multiple trials of runs at different temperatures; no measurable chemisorption results were obtained at 40 °C and 80 °C, indicating a temperature dependence of the chemisorption kinetics.

Air leakage into the system has a crucial impact on the chemisorption results. For our experimental setup, we found that even ~40 ppm of O₂ entering the system is enough to passivate the Ni active sites, and no chemisorption is observed. Hence, it is crucial to ensure that the system is airtight as much as possible.

Catalyst particle size also has an impact on chemisorption. The catalyst particles were sieved into several size fractions and tested for chemisorption. At 60 °C, particles in size range of 150-250 μm yielded satisfactory results. For the particle size >250 μm, a temperature of 80 °C worked well but showed no CO or H₂ uptake at 60 °C.

The partial pressure of the probing molecule (H₂ in our case) is another consideration. On switching between pure H₂ and 10% H₂ diluted in He, it was observed that 10% H₂ did not result in any observable chemisorption.

Loading the catalyst above 100 mg was found to be detrimental toward obtaining useful chemisorption results, and a mass of 50 mg appears to work satisfactorily for the present setup.

Pulse or injection volume differs between instruments and is also known to affect chemisorption results. The injection loop in the Microactivity Effi system is calibrated to be 0.525 cm³ at STP.

While it is difficult to provide a generalized set of conditions for successful chemisorption results, the success of the technique depends on a precise combination of these factors, which must be fine-tuned for each experimental setup.

2.2. Methodology

2.2.1. ALD Catalyst Synthesis²

Commercially procured 20 wt.% nominal Ni/Al₂O₃ powder (Riogen Inc., NJ, USA) was sieved to a 150-250 μm range and used as the reference catalyst (hereafter referred to as “Commercial”). Before overcoating by ALD, the as-received Commercial catalyst was sieved to <250 μm particle diameter and dried overnight at 105 °C in air, before cooling in air and storage in a sealed container. ALD overcoatings were performed using an Arradiance Gemstar ALD reactor operating at 175 °C using tri-methyl aluminum (TMA) and water, with N₂ as the purge gas. Timing sequences for the ALD cycles are described here as an A step and a B step to complete one ALD cycle. In the A step, the reactor outlet valve was closed and a 1 s pulse of the “A” precursor (TMA) was introduced by holding open a valve between the precursor bottle and the reactor for 1 s. The reactor was subsequently held for 30 s to allow diffusion of the “A” precursor before the reactor outlet valve was opened to vacuum and held for 5 s to evacuate the chamber. This entire process of pulsing, holding, and evacuating was repeated 12 times, after which 100 ml/min of N₂ was flowed through the reactor for 90 s to purge all unreacted TMA. These tasks together constitute a single A step.

² The catalyst synthesis of ALD catalysts was done by Patrick Littlewood at Northwestern University.

In the B step, the same events and timing sequence are used to dose the "B" precursor, except the "B" precursor pulse was performed by holding open a valve between the H₂O precursor bottle and the reactor for 1 s. Note that 12 cycles of pulsing, holding, and evacuating, followed by a 90 s purge in 100 mL/min N₂ constitute a full B cycle. For TMA/H₂O, approximately 500 mg of the substrate was loaded into the reactor. Note that longer dose, hold, and purge times, as well as additional numbers of pulse-hold-evacuate cycles, were also investigated and gave no additional deposition. It should be noted that these dose/purge times may be reactor specific. The overcoated samples in this study were prepared using 5, 10, and 20 complete ALD cycles to generate the protective layers ('X-ALD', X: number of alumina ALD cycles on Commercial catalyst). Overcoated catalysts were not calcined after ALD. The ALD catalysts were sieved to the same size range as the Commercial catalyst, 150-250 μm, before performing the sintering study.

2.2.2. H₂-CO Pulse Chemisorption Technique to measure in-situ dispersion

The H₂-CO sequential chemisorption procedure, as specified by the term itself, primarily comprises two steps: H₂ chemisorption followed by CO chemisorption, resulting in H₂ desorption. The CO binds more strongly to Ni than H₂ and hence, for every CO pulse, there is an evolution of the adsorbed H₂ as it is displaced from the catalyst surface [54]. This procedure is outlined in Figure 8.

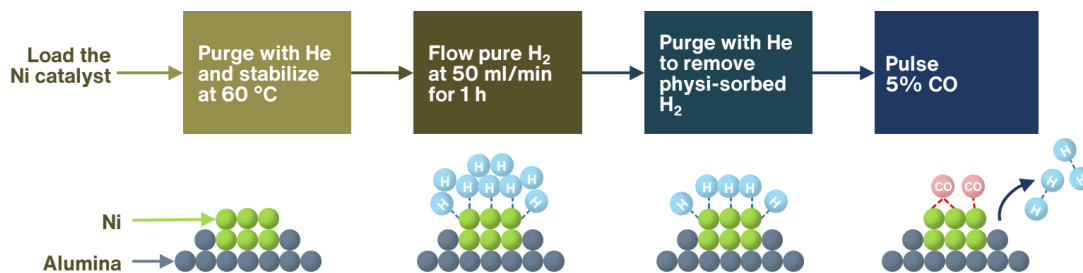


Figure 8 - H₂-CO Sequential Chemisorption Protocol. Reprinted from [22]

At first, the catalyst is reduced by ramping to 650 °C at 10 °C/min in pure H₂ (50 mL/min flow) and holding for 1 hr thereafter. Following this, the system is purged in He for 30 min and finally ramped down in He to 60 °C. After the reduction of the catalyst for the desired experiment, the sample temperature is equilibrated at 60 °C. Pure H₂ is passed through the

catalyst bed for 1.0 h, followed by purging out residual, physisorbed H₂ with He for another 1.0 h. Subsequently, CO is pulsed from a standard chemisorption loop (0.525 cc at STP) at 5-min intervals until peak saturation. The desorbed H₂ peaks are then used to calculate dispersion and crystallite size. Pulse signals are recorded using an online mass spectrometer, the MKS Cirrus 2 RGA (Residual Gas Analyzer). Several parameters affect chemisorption and a trial-and-error approach is followed to optimize conditions for each experiment as detailed in 2.1.1.

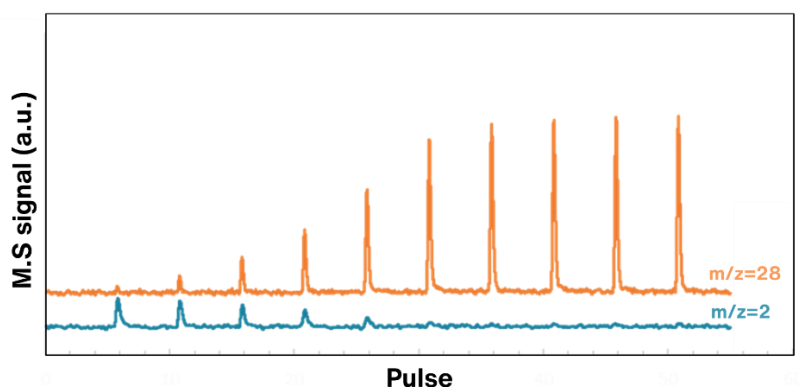


Figure 9 – RGA responses of CO (m/z=28) and H₂ (m/z=2) during the CO chemisorption step. Reprinted from [22]

Figure 9 shows the overlapped CO and H₂ peaks from the RGA. The amount of H₂ desorbed is directly proportional to the number of exposed Ni atoms, which is expressed as percent dispersion (%D) by Equation 7:

$$\%D = \frac{C_2 X}{fw} \quad (7)$$

C_2 → constant for Ni = 1.17, based on Bartholomew and Farrauto [39]

X → chemisorption uptake in $\mu\text{mol/g}$ (desorbed in our case)

f → extent of reduction

w → weight % of metal in the sample (obtained from ICP-OES)

The f refers to the extent of reduction or degree of reduction (DOR), which was estimated by Thermo-Gravimetric Analysis (TGA). The catalyst was dried at 150 °C for 2 h. Then, the temperature was ramped at 10 °C/min to 650 °C in a pure H₂ atmosphere for reduction. This was followed by an N₂ purge for 30 min. Finally, the sample was oxidized with pure O₂. The DOR is calculated based on the weight gain during the oxidation process. All the reduced Ni will oxidize, and the ratio of reduced Ni/total theoretical Ni gives the DOR. The sample calculation of DOR for the Commercial and 5-ALD catalysts are given in Table 1 and Table 2.

Table 1 – DOR Calculation for Commercial catalyst. Reprinted from [22]

| | |
|--|----------|
| Weight of catalyst (mg) | 6.3 |
| Moisture Loss (mg) | 0.217 |
| Moles of water | 1.21E-05 |
| | |
| Dry Catalyst (mg) | 6.083 |
| Amount of Ni (mg) | 1.0962 |
| Moles of Ni | 1.87E-05 |
| | |
| Reduction Loss (mg) | 0.4556 |
| Moles of O lost in reduction | 2.85E-05 |
| | |
| Oxidation Gain (mg) | 0.2893 |
| Moles of O consumed in oxidation | 1.81E-05 |
| | |
| Theoretical Weight Gain if all Ni sites are oxidised to NiO (mg) | 0.2988 |
| DOR (Based on Theoretical No. of Moles) | 96.82% |

Table 2 – DOR Calculation for 5-ALD catalyst. Reprinted from [22]

| | |
|--|----------|
| Weight of catalyst (mg) | 6.3 |
| Moisture Loss (mg) | 0.2052 |
| Moles of water | 1.14E-05 |
| | |
| Dry Catalyst (mg) | 6.0948 |
| Amount of Ni (mg) | 0.7812 |
| Moles of Ni | 1.33E-05 |
| | |
| Reduction Loss (mg) | 0.4096 |
| Moles of O lost in reduction | 2.56E-05 |
| | |
| Oxidation Gain (mg) | 0.1828 |
| Moles of O consumed in oxidation | 1.14E-05 |
| | |
| Theoretical Weight Gain if all Ni sites are oxidised to NiO (mg) | 0.2129 |
| DOR (Based on Theoretical No. of Moles) | 85.85% |

The ' f ' was found to be ~ 0.97 for the uncoated Commercial catalyst and ~ 0.86 for the 5-ALD catalyst. More discussion on this parameter is included in section 2.3.2. The ' w ' in the equation accounts for the quantity (weight %) of Ni loaded in the catalyst. Since the ALD catalyst has additional layers of alumina that reduce the % Ni content, all samples were analyzed by ICP-OES (Inductively Coupled Plasma Optical Emission Spectroscopy) to get accurate Ni wt%. The results are shown in Table 3.

Table 3 – ICP-OES Results and mass gain from ALD. Reprinted from [22]

| Sample | Ni wt. % | Mass Gain from ALD % |
|------------|----------|----------------------|
| Commercial | 17.4 | - |
| 5-ALD | 12.4 | 44 |
| 10-ALD | 11.3 | 67 |
| 20-ALD | 11.6 | 75 |

For the ICP-OES analysis, 10 mg of each sample is weighed out and 2 mL of concentrated H₂SO₄ is added. The sample is heated to 250 °C and held for 1 h at that temperature, heated further to 300 °C and held for 30 min until completely dry. After cooling to room temperature, 2 mL each of concentrated HCl and HNO₃ is added and the mixture heated to 150 °C. After 10 - 20 min of heating, the sample is cooled, and deionized water added to make up the required volume. The analysis is performed in an ICP-OES PQ9000 (AnalytikJena), having a plasma flow of 12 L/min, auxiliary flow 0.5 L/min, nebulizer flow 0.5 L/min, RF power 1200W, and sample flow rate of 1 mL/min.

2.2.3. Sintering Protocol

All the sintering tests were conducted in a compact Microactivity Effi unit (PID Eng&Tech, Spain) modified by Micromeritics Inc. (Georgia, USA) for in-situ temperature-programmed experiments. A 0.525 mL sample loop allows for in-situ chemisorption studies. A schematic of the experimental setup is shown in Figure 10. 50 mg of catalyst is loaded into a 9.2 mm internal diameter quartz reactor and pre-treated by drying under He for 2 h at 150 °C. After reduction by ramping to 650 °C at 10 °C/min in pure H₂ (50 mL/min flow), the system is purged with He for 1 h and ramped down to 60 °C. Before starting the sintering process, the initial dispersion is estimated in-situ via the sequential H₂-CO chemisorption protocol, as described in section 2.2.2. The DRM experiment is initiated by ramping the temperature to 650 °C in He and then switching to a flowing gas mixture of 10%CH₄:10%CO₂:2%Ar diluted in He through the catalyst bed at 150 mL/min. Over the course of ~40 h the DRM reaction is paused at intervals and cooled in He to 60 °C and H₂-CO sequential chemisorption is performed, in-situ. Thus, the Ni surface available for chemisorption is monitored at intervals.

At the end of 40 h DRM, six dispersion readings have been obtained for each catalyst. All data (reaction and chemisorption) is acquired via an online Cirrus 2 Residual Gas Spectrometer (MKS Instruments, UK). Further details of the product characterization system used are described in Appendix A.

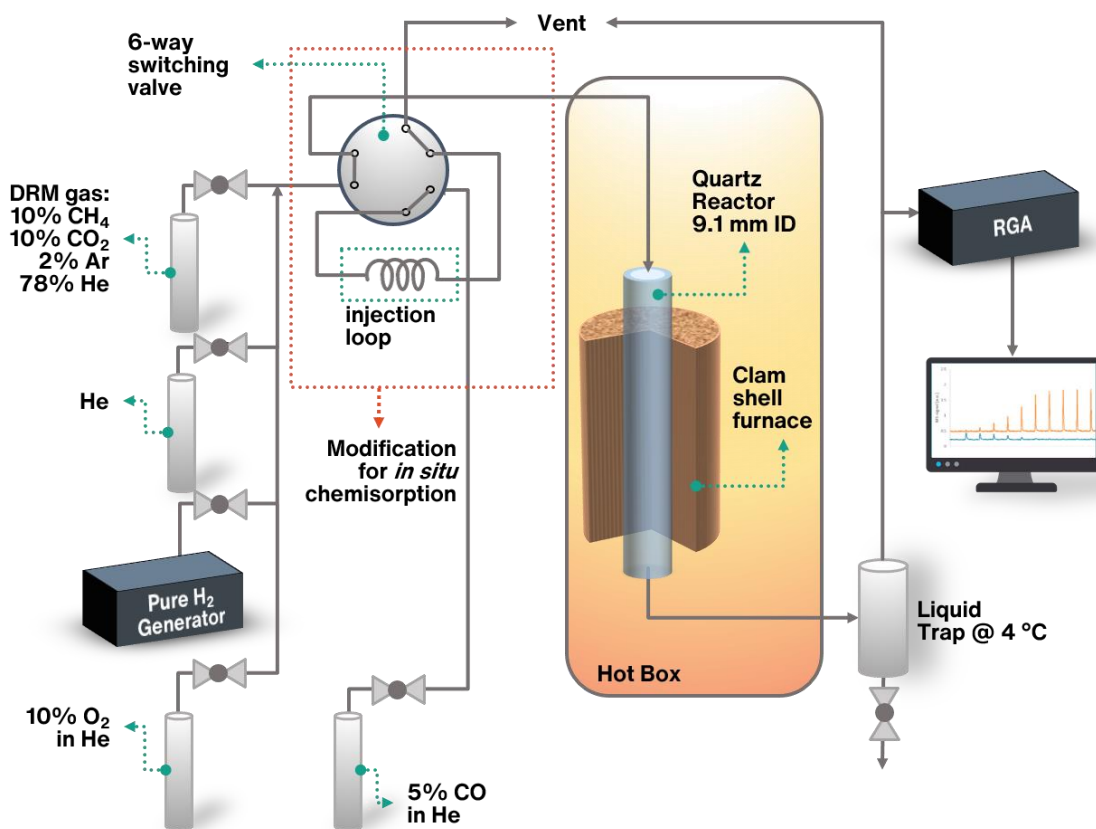


Figure 10 – Experimental Setup for DRM reaction. Modification for in-situ chemisorption highlighted in red. Reprinted from [22]

2.2.4. High-Resolution Transmission Electron Microscopy

Transmission Electron Microscopy (TEM) is used to measure metal crystallite size and size distribution, before and after the DRM reaction. The post-DRM samples also have a TPO and an H₂ reduction step included. High-resolution micrographs were obtained with FEI Talos F200X transmission electron microscope set at 200 kV. Images were processed with ImageJ 1.51j8 and DigitalMicrograph v3.22.1461.0.

2.3. Results of the chemisorption study

The data for total H₂ moles desorbed at various intervals during the sintering campaign is shown in Figure 11. The first chemisorption data point was collected after the initial H₂ reduction step, before initiating the DRM reaction. Subsequent chemisorption analyses were performed by stopping the DRM reaction at desired intervals, ramping down from the DRM temperature of 650 °C to the chemisorption temperature of 60 °C in He atmosphere, and then performing the chemisorption protocol as detailed in section 2.2.3. After the 40 h TOS, a TPO was performed for all catalysts except for the 20-ALD catalyst. A 10% O₂ in He gas was used and the temperature was ramped to 750 °C at a rate of 10 °C/min including a hold for 1 h at 750 °C. This was done to remove the carbon deposited by the DRM reaction. After the TPO, the catalyst was reduced by flowing pure H₂ of 50 mL/min and ramping the temperature to 650 °C at 10 °C/min and held for 30 min. An additional chemisorption evaluation was then performed to calculate dispersion on the ‘clean’ Ni surface.

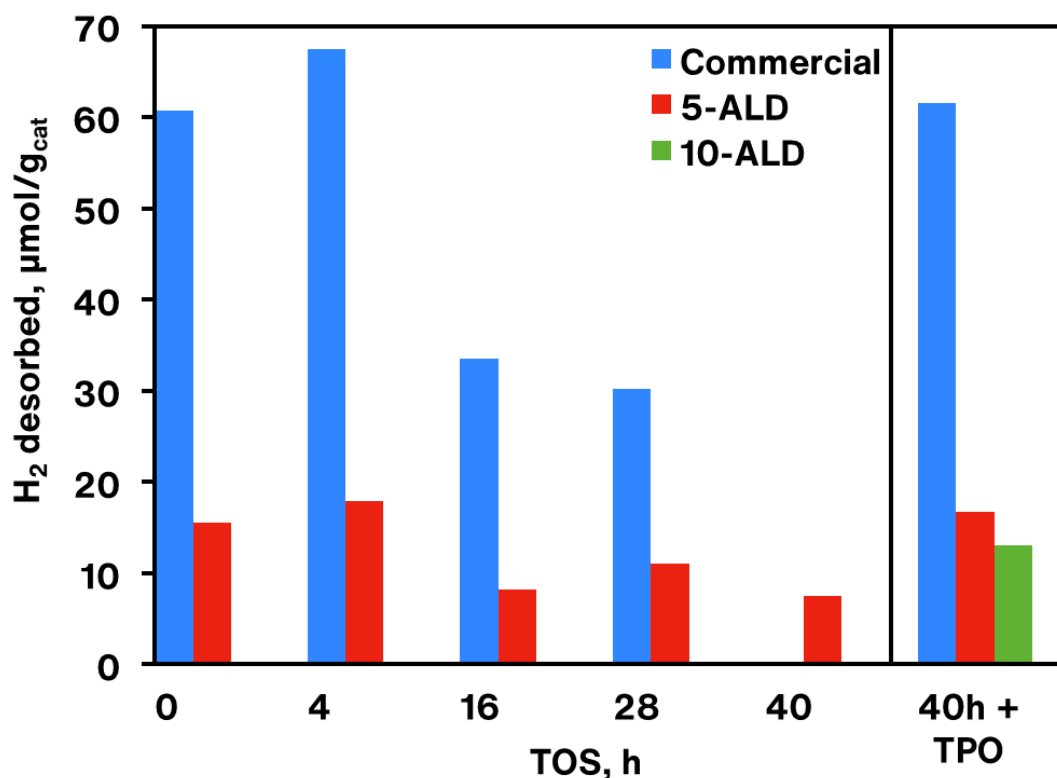


Figure 11 - H₂ desorbed, μmol/g_{cat}, during H₂-CO chemisorption, at specific intervals during 40h of DRM. Right pane: After TPO at the end of 40 hours.

Reprinted from [22]

As evidenced from Figure 11, only the Commercial and 5-ALD catalysts showed noticeable H₂ desorption. On the other hand, the 10-ALD and 20-ALD samples did not show any H₂ desorption for the duration of the sintering experiment under the DRM atmosphere, most likely due to more complete and pinhole-free coverage [41] of the Ni sites by the ALD overcoat. Dumesic and coworkers [12] have shown previously that regeneration by heat treatment enhances the porosity of an alumina ALD overcoat, and therefore, an additional 5-hour TPO was carried out for the 10-ALD and 20-ALD coated Commercial catalysts to observe H₂ uptake. Although the 20-ALD sample displayed no signs of H₂ desorption even after intermediate TPO treatments, the 10-ALD sample exhibited H₂ desorption of ~13 μmol/g_{cat}. With the TPO, the quantity of exposed Ni in the 10-ALD becomes comparable to that of the unused 5-ALD catalyst. Other studies have also observed improved accessibility

to underlying active sites after thermal treatment of the ALD overcoat at high temperatures (750 °C in this case), as a consequence of evolving pore structure [59]. Alternatively, it may be that high-temperature oxidation allows Ni to react with the Al_2O_3 overcoat to form NiAl_2O_4 , which subsequently reduces under H_2 , allowing the Ni to effectively migrate through the overcoat to the surface via a NiAl_2O_4 intermediate or causing the overcoat to restructure. These results, however, also imply that the chemisorption technique may be limited in its applicability to investigate sintering behavior for ALD and similar core-shell catalysts where Ni sites are not sufficiently exposed. Measured activities for DRM in the case of the 10 and 20 cycle coated catalysts were significantly lower than for 5-ALD and Commercial catalysts (refer to section 3.4), confirming that the Ni crystallites were more completely covered by the amorphous alumina overcoat. For such catalytic systems with relatively thicker shells, other techniques such as TEM or XRD may be better suited to estimate crystallite size but may not give much information on the amount of exposed Ni surface area. The ensuing discussion of results will hence focus on the uncoated Commercial catalyst and the 5-ALD coated catalyst as these provide the most useful results.

From Figure 11, the H_2 desorbed from the Commercial and 5-ALD catalysts at 0 h (pre-DRM) is 60.7 and 15.6 $\mu\text{mol}/\text{g}_{\text{cataly}}$, respectively. In the case of the 5-ALD catalyst, the overcoat covers some of the Ni active sites, thus reducing H_2 uptake. After about 4h of DRM reaction at 650 °C, the H_2 -CO sequential chemisorption procedure is performed again to determine the change in dispersion. For both Commercial and 5-ALD catalysts, a slight increase in the moles of H_2 desorbed is observed. This can be attributed to an increase in the extent of Ni^{2+} reduction within the DRM atmosphere, producing new Ni active sites [60]–[62]. Note that this does not exclude the possibility that the sintering of existing Ni sites also simultaneously occurs. As the reaction proceeds, a gradual decrease in H_2 desorption is observed indicating loss of active catalyst surface area, either due to sintering and/or coking. After 40h of DRM TOS, the Commercial catalyst shows no H_2 desorption, meaning that either or both of two possibilities has occurred: accessibility to all Ni sites is now obstructed by carbon deposits, or that sintering has resulted in a loss of Nickel surface area, reducing H_2 uptake [63]. As will be

shown in section 2.3.1, TEM images verify the changes in crystallite size thereby corroborating the results of this chemisorption study.

After carrying out TPO to oxidize the deposited carbon and re-reducing the Ni, the amount of H₂ desorbed increases to the same quantity as before DRM, for both Commercial and 5-ALD catalysts. TPO is expected to remove encapsulating carbon, which will permit H₂ chemisorption. However, this alone is insufficient in explaining the markedly higher jump in H₂ desorption considering that the catalyst has undergone sintering, reducing the available Ni area for chemisorption. The additional uptake could likely be due to the “redispersion” effect [64]–[66] and/or an increased extent of NiO reduction after the TPO. The latter phenomenon was studied in detail by Silvester et al. [67] where partially-reduced NiO species, interacting strongly with the alumina support, form more reducible NiO species on oxidation than were previously available. In the case of re-dispersion, oxidation of the sintered crystallite produces oxy-metal species that tend to migrate and disperse across the support surface because of ‘strain’ between them and adjacent reduced species. Thus, H₂ desorbed correlates directly with the proportion of smaller, dispersed Ni crystallites, and is not influenced by the presence of larger, sintered Ni, highlighting the sensitivity of this technique over TEM. Either or both of these effects could explain the increase in H₂ desorption after TPO.

The in-situ evolution of dispersion, as calculated by equation 7, is shown in Figure 12. From the slopes of the lines, the rate of change of dispersion for the Commercial catalyst is $\sim 0.11\%h^{-1}$ whereas, for the 5-ALD catalyst, it is slower at $0.025\%h^{-1}$. It is expected that the ALD overcoat impedes the sintering process by anchoring down the Ni crystallites [68]. One could also argue that by maintaining a smaller crystallite size, deactivation via the coke deposition rate is also reduced [69]. More discussion on this is provided in section 2.3.3. A similar observation was made by Hansen et al. [70] but for Pd on alumina catalysts, for which the dispersion dropped exponentially from 4% to about 1% in 100 h.

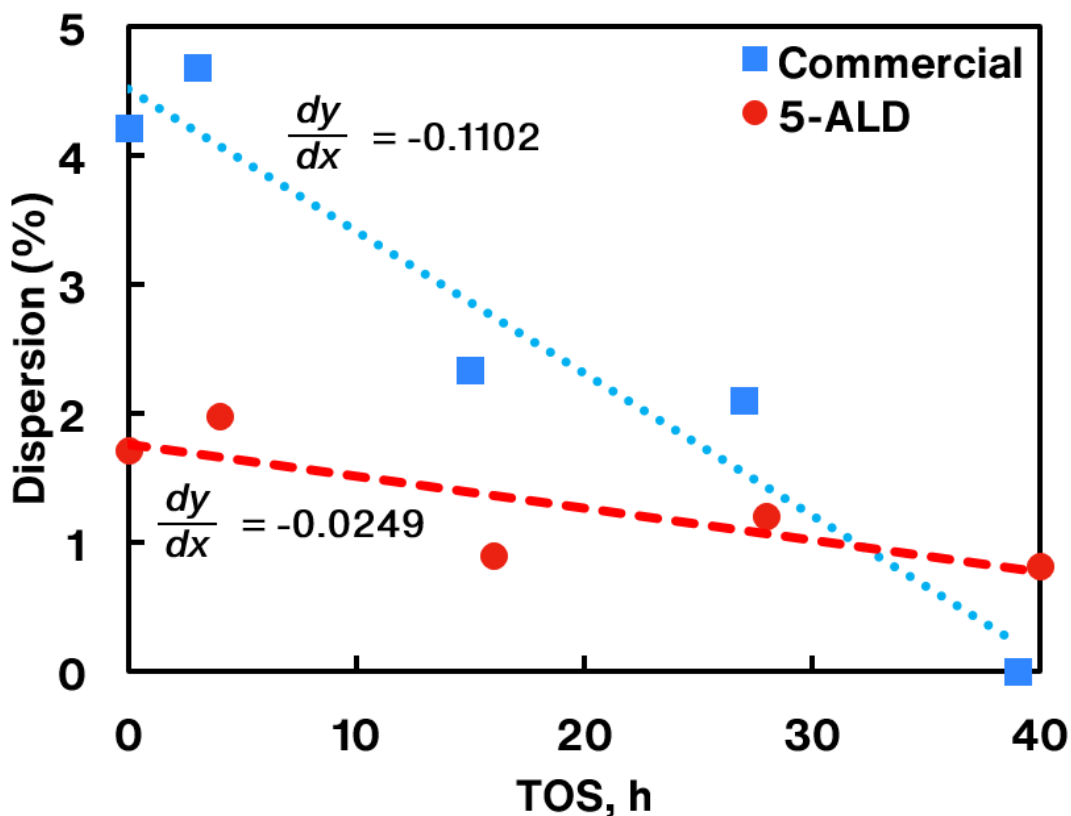


Figure 12 – Change in Ni Dispersion for Commercial and 5-ALD catalysts with Time-on-Stream; equations show the relative rates of change in dispersion.

Reprinted from [22]

Analyzing the H₂-CO chemisorption data in terms of individual pulses of both H₂ and CO hints towards the dependence of this technique on the nature of exposed Ni sites, and the differences in their adsorption stoichiometries. Figure 13 comprises snapshots of the sintering process at selected intervals in the form of moles of H₂ desorbed and CO consumed in consecutive pulses. It is apparent that for almost all cases, the moles of CO adsorbed is greater than that of H₂ desorbed. This difference in the adsorption stoichiometries of CO and H₂ on Ni surfaces plays an important role here and has been discussed at length by Bartholomew and Pannell [71]. In general, H₂ dissociates prior to adsorption in a 1:1 H:Ni ratio, while for CO, the presence of bridge and sub-carbonyl bonding, in addition to CO-Ni linear bonding,

complicates adsorption calculations. Moreover, the uptake of CO by Ni increases in the presence of pre-adsorbed H₂ [56], which might explain the observed trends.

An exception is highlighted in Figure 13 (b), wherein after 4 hours of DRM, the trend in pulse volumes reverse after 3 pulses. Specifically, the quantity of CO adsorbed after 3 pulses drop below the quantity of H₂ desorbed. A probable cause is that the rapid sintering of the Ni catalyst during the initial phase of the reaction [70] produces a growing pool of larger crystallites having fewer low-coordination Ni sites (edge/corners). It is known that CO binds strongly as a bridged species ($\text{CO}_{\text{ads}}:\text{Ni} < 1$), on larger crystallites, i.e. metal clusters with a higher terrace to corner/edge ratio. Given that fewer CO molecules are now required to bind to the available Ni, the amount of CO consumed drops once all the low-coordination sites are occupied. H₂ however, continues to desorb via facile formation of the H-CO surface complex on the continued addition of CO. These observations highlight the sensitivity of the H₂-CO sequential chemisorption towards the evolution of catalyst active site over the course of sintering in a DRM atmosphere.

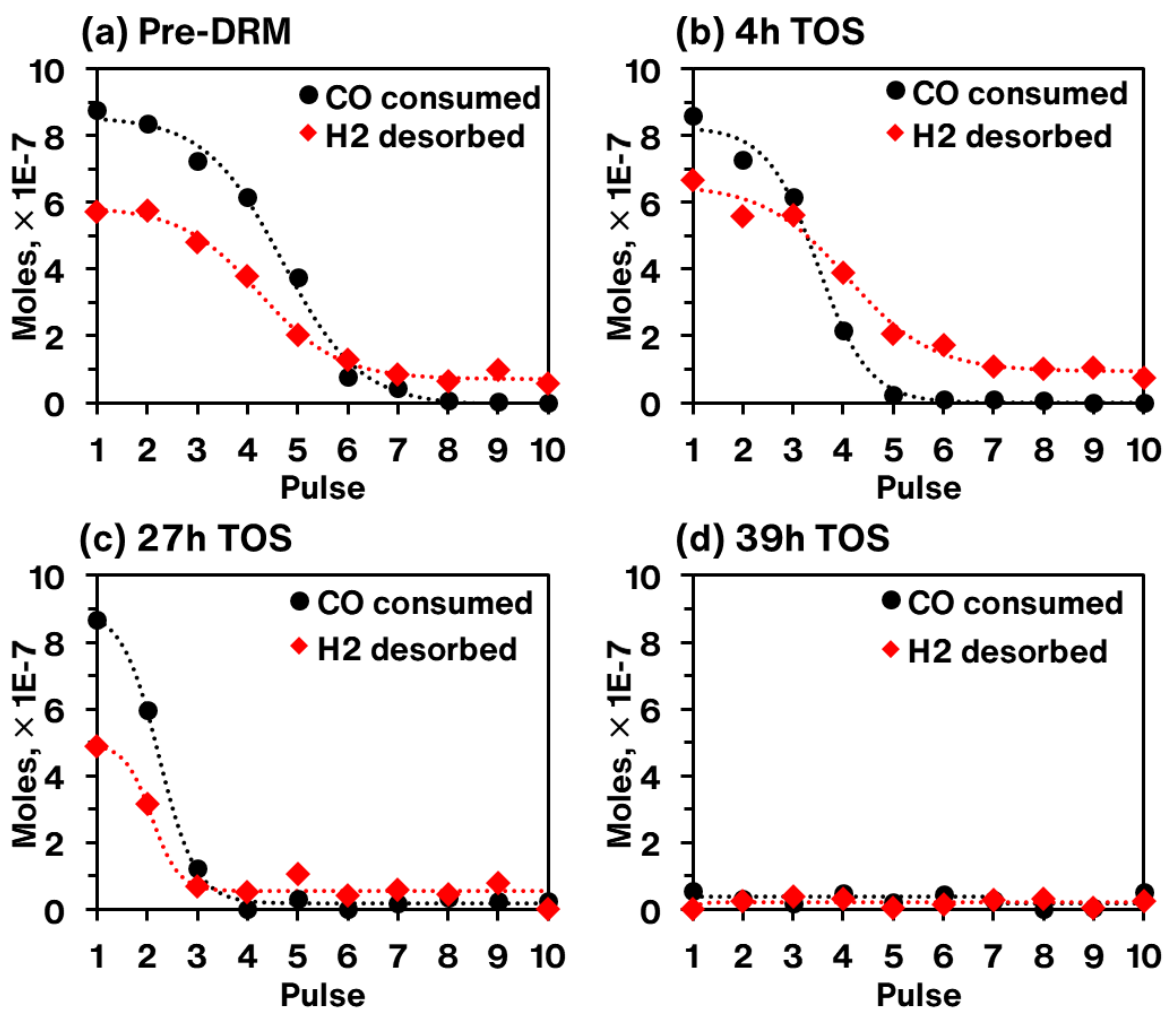


Figure 13 – Pulse injection trends comparing CO moles consumed and H₂ moles desorbed per pulse at various intervals during sintering of the Commercial catalyst.

(a) before DRM, (b) after 4 hours (c) 27 hours and (d) 39 hours of DRM. Dotted lines represent data smoothed data. Reprinted from [22]

Moving from the commercial catalyst to the over-coated 5-ALD catalyst, a rather interesting phenomenon is observed with the trend of CO consumption. While H₂ ceases to desorb after a few pulses, the overcoated system continues to consume CO unexpectedly, after reaching a temporary ‘saturated’ state. While there is no obvious interpretation for this, a rather speculative explanation has to do with the micro-porous nature of the ALD overcoat. When the pore diameter approaches that of the diffusing molecule, a transition occurs from

conventional Knudsen diffusion to configurational diffusion regime [72]. Configurational diffusion is associated with significant energy barriers and is controlled by several factors including pore size and shape, kinetic diameter, and polarizability of the molecule, as well as the presence of functional groups in the pore leading to considerable gas-surface interactions. Other nano-porous materials like zeolites and metal-organic frameworks have exploited these effects for selective gas separations. Of particular interest is a certain class of MOFs that exhibit a ‘breathing’ effect, (e.g. Aluminum terephthalate MIL-53(Al)) [73], [74], not unlike the enhanced CO consumption observed for the Alumina ALD coated catalysts. Depending on the interactions with the incoming ‘guest’ molecule, the MOF framework can undergo a substantial expansion, allowing for greater consumption of the guest molecule. Another study on nano-porous ALD coated membranes [75] concluded that gas transport through pores is affected by pore diameters and surface functional groups. The existence of these anomalous interactions cannot be proved definitely by the techniques presently used, and as such, these explanations should be considered speculative.

Calculating dispersion from moles of CO adsorbed during this binary H₂-CO sequential technique is also a possibility. However, this will yield values larger than for a CO-only chemisorption experiment as a result of greater CO uptake in the presence of an H₂ adlayer. As discussed by Wedler et al. [56], H₂ pre-adsorption on a polycrystalline Ni surface results in a more negative enthalpy of CO adsorption, increasing CO uptake. Unlike CO, H₂ pulse trends follow the expected pattern of desorption as in the case of the commercial catalyst. This aids in the reliable measurement of moles of H₂ desorbed, which in turn is used to estimate dispersion. These results highlight the advantage of the binary H₂-CO chemisorption method over a conventional CO pulse chemisorption for ALD and similar core@shell systems with porous overcoats.

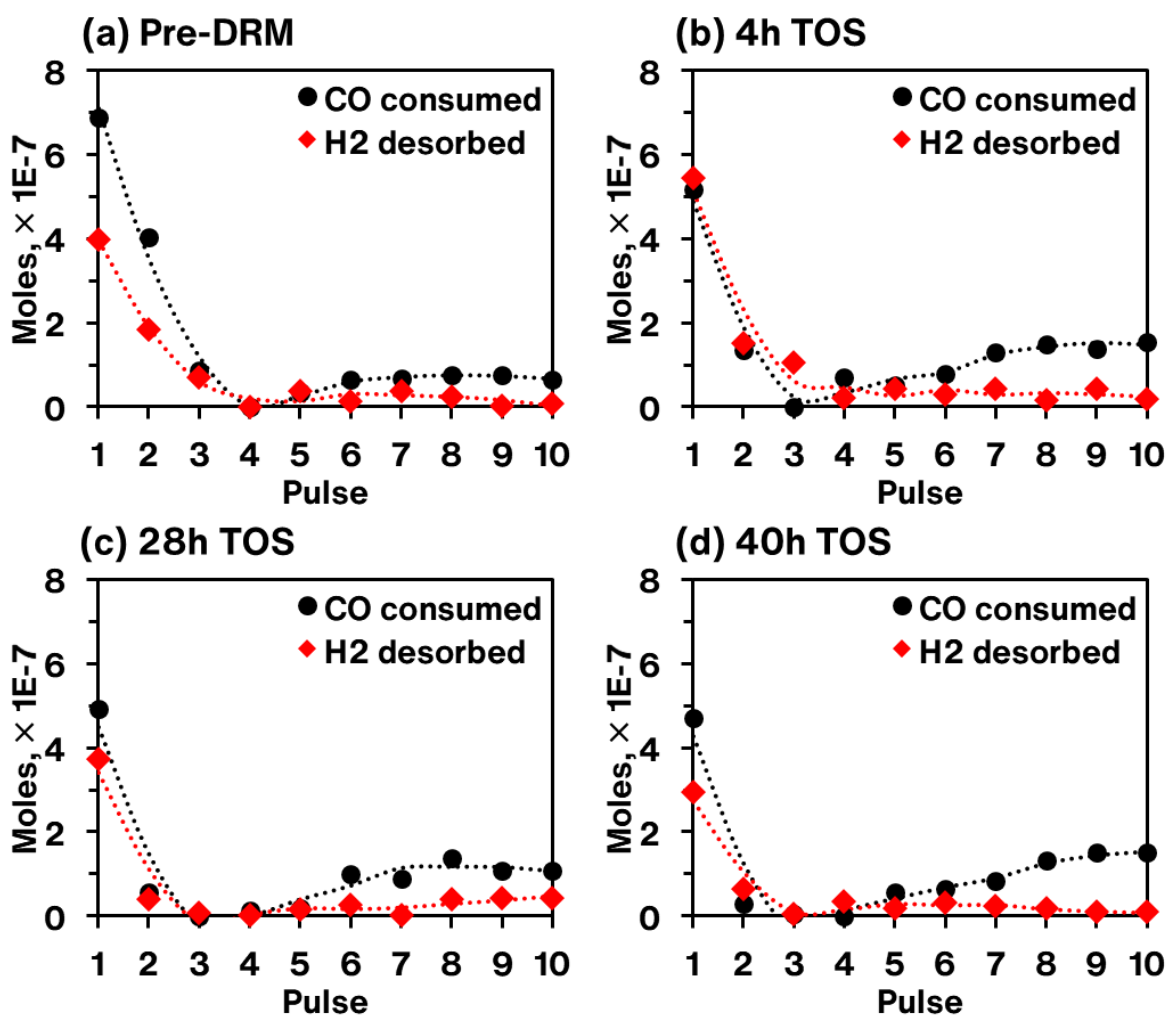


Figure 14 – Comparison of CO moles consumed vs. H₂ moles desorbed per pulse at various stages of sintering for the 5-ALD catalyst. Dotted lines represent smoothed data. Reprinted from [22]

2.3.1. TEM Imaging Results

TEM images were taken before the reactions and after 40 h of DRM, including after the final TPO and H₂ reduction. The diameter of visible particles is measured, and the particle size distribution is plotted. The results and selected images at various magnifications are shown in Figure 15.

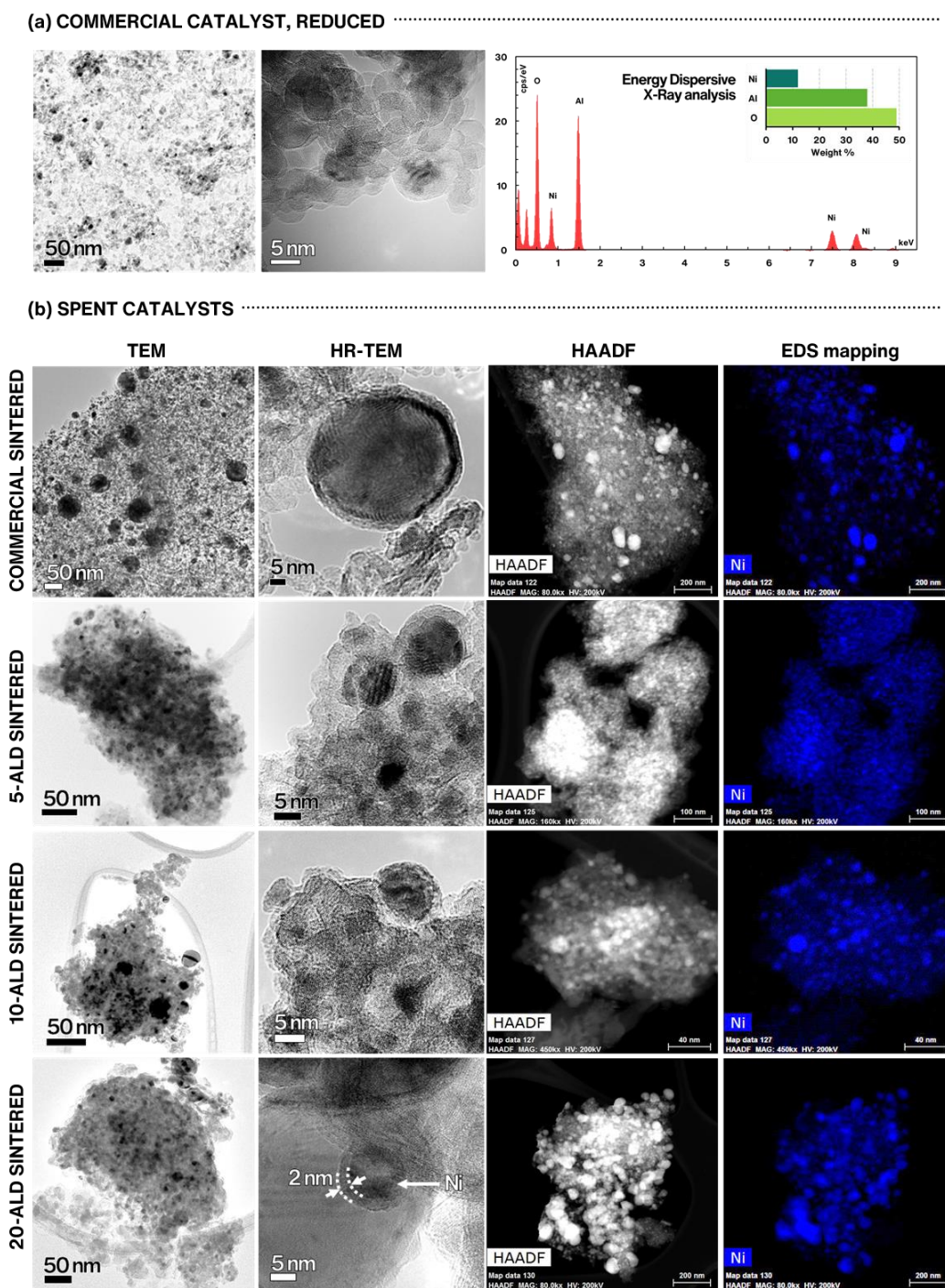


Figure 15 – Comparison of TEM images of Commercial and ALD Ni catalysts before and after DRM of 40 h TOS. (a): fresh, reduced Commercial and EDS elemental analysis. (b): TEM, HAADF, Ni EDS mapping for sintered catalysts.

Reprinted from [22]

It is evident from the images of the Commercial catalyst, both before and after reduction, that there is an increase in the average particle size. The normalized frequency was calculated by dividing the frequency of different particle sizes by the total number of particles in the sample and multiplying this by 100. The normalized frequencies of particle sizes for all cases are plotted in Figure 16. The Commercial catalyst particle size distribution clearly shows a shift to the right after 40 h DRM, indicating that the particle sizes have increased because of sintering.

For the ALD-coated catalysts, the initial particle size can be assumed to be the same as the Commercial catalyst, the reason being that the ALD process uses the same catalyst as the starting material and does not involve temperatures of more than 175 °C, which is too low to cause significant Ni sintering. The Commercial catalyst distribution clearly shows a shift to higher crystallite sizes in Figure 16, indicating that the particles have sintered, and it also features a bimodal particle size distribution in contrast to either the fresh or ALD coated catalysts. The sintered 5-ALD and 10-ALD catalysts show similar distributions before and after the reaction, indicating that the average particle size has remained the same. This confirms that the ALD alumina overcoat helps stabilize the particle size more effectively than the uncoated catalyst.

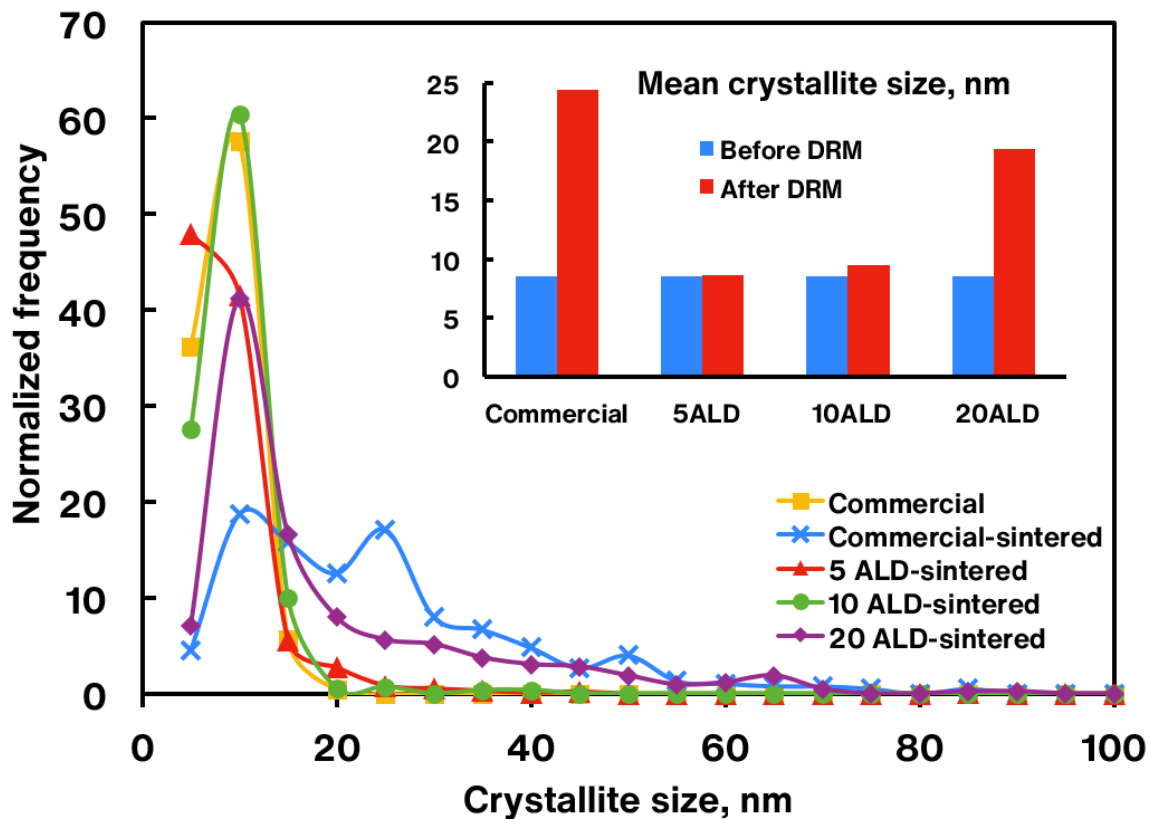


Figure 16 – Normalized particle size distribution as measured from selected TEM images for the different catalyst samples (data-points connected for clarity). Inset: Mean crystallite size comparison of the investigated catalysts before and after 40h DRM. Reprinted from [22]

For the sake of clarity, the mean particle sizes are plotted in Figure 16. The average particle size of the Commercial catalyst significantly increases from an average of 8.4 nm to 24.5 nm after sintering. For the 5-ALD and 10-ALD, the post-DRM particle sizes are close to their pre-DRM values, at 8.7 nm and 9.5 nm, respectively. The prevalence of crystallites less than 10 nm for the used 5-ALD catalyst increases slightly, with respect to the other catalysts. This could be a result of re-dispersion after TPO (performed at the end of 40h DRM) producing smaller crystallites that get trapped in the alumina ALD matrix as the overcoat further crystallizes. It would be expected that the thicker overcoats for 10 and 20-ALD catalysts

would likely retard the extent of re-dispersion, and thus the likelihood of generating smaller crystallites.

Interestingly, for the 20-ALD, the post-DRM particle size is relatively high at ~ 19.4 nm, though it is still lower than that of the spent uncoated Commercial catalyst. We hypothesize that for the 20-ALD catalyst, the thicker layer of amorphous alumina deposited by ALD over the active site effectively acts as a medium for enhanced sintering under the conditions applied. Stair and coworkers [62] have recently demonstrated the formation of Nickel Aluminates within the overcoat in a 20-cycle ALD coated Ni/Al₂O₃ catalyst, in a reducing environment. Although NiAl₂O₄ is not catalytically active for DRM, a gradual increase in activity was observed as a result of Ni²⁺ reduction under DRM conditions, precipitating metallic Ni. We hypothesize that this newly formed Ni, which is now active for DRM, sinters gradually during DRM, perpetuating crystallite growth. This phenomenon is not as pronounced in the 5 and 10 ALD cycle coated catalysts probably due to the lack of the required 'threshold' thickness to facilitate this process of NiAl₂O₄ formation, reduction, and subsequent Ni coalescence. Considering that there is a thermodynamic driving force preventing Ni⁰ from reacting with alumina [76] under these conditions, Ni²⁺ must react with the ALD overcoat to form NiAl₂O₄ before it is reduced by H₂, and this is more likely to occur when a thicker alumina overcoat restricts access to the gas phase H₂. The presence of NiAl₂O₄ spinel in the 20-ALD catalyst after 40 h of DRM is confirmed via HR-TEM imaging (Figure 17). The rate at which this particular coalescence occurs is probably dissimilar to that for commercial nickel catalyst, considering the lack of a bimodal crystallite size distribution as in the case of the sintered commercial catalyst.

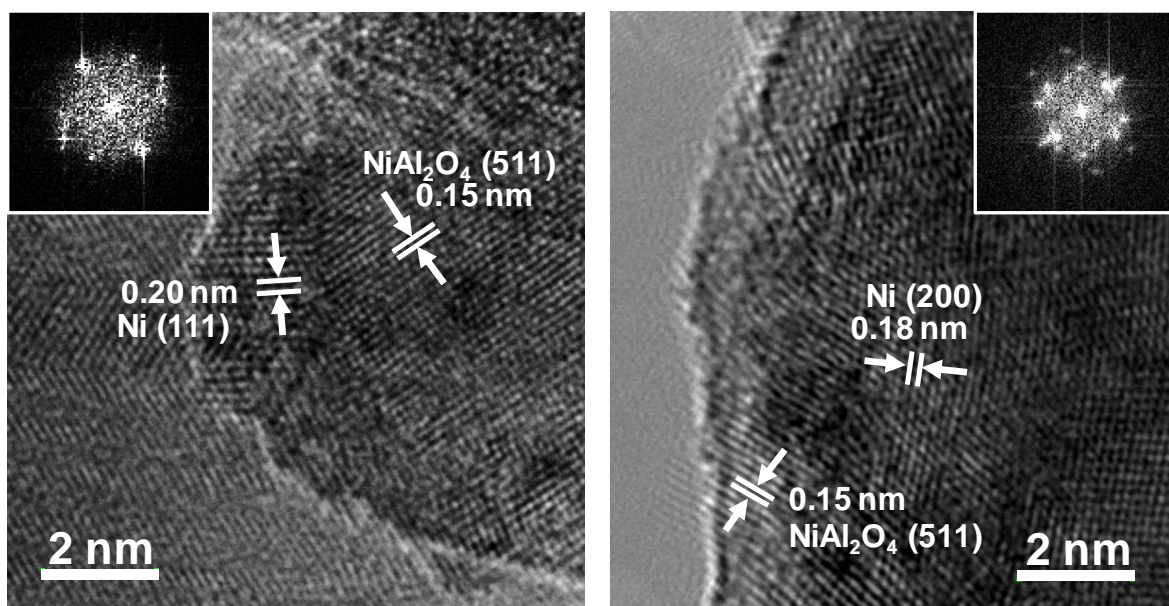


Figure 17 - HR-TEM images of 20-ALD catalyst highlighting the presence of Ni (111), (200) and Nickel Aluminate spinel (511) phases. Data for calculation of d-spacing obtained from reference JCPDS 10-0339 for Nickel Aluminate and JCPDS 04-0850 for Nickel. Reprinted from [22]

2.3.2. Comparing TEM and Chemisorption Results

Extensive work on chemisorption by Bartholomew et al. [50], [77] highlight the advantages and limitations of TEM and chemisorption, to estimate crystallite size for supported Nickel systems. These methods should, therefore, be considered complementary to each other. For example, in the case of chemisorption, overestimating the mean Ni particle diameter is a possibility if those Ni atoms located at the interface of the metal crystallite and support cannot be probed by chemisorption [47]. Chemisorption is a bulk technique that tends to probe smaller, dispersed crystallites quite well and is structure sensitive, while TEM provides a visual picture of the individual crystallites and general particle size distribution but does not give a direct measurement of the surface available to the gas phase.

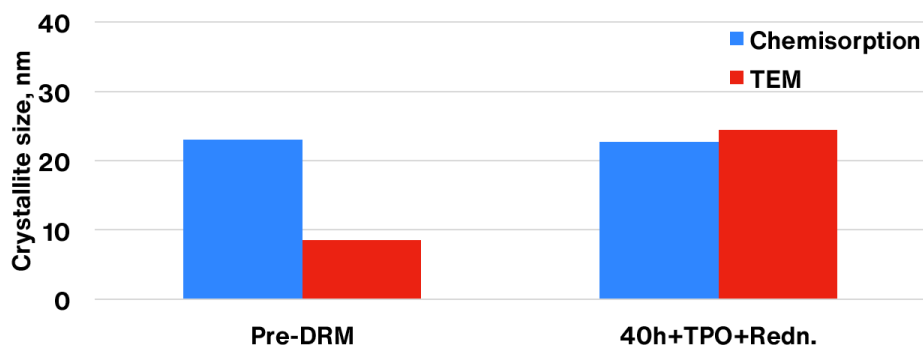
Figure 18 shows the comparison of crystallite sizes estimated by the chemisorption technique and TEM imaging. The crystallite size, d for Ni catalysts is estimated by Equation 8:

$$d = \frac{C_1}{\%D} = C_1 \frac{fw}{C_2X} \quad (8)$$

C_1 → constant for Ni = 97, based on Bartholomew and Farrauto [39]

$\%D$ → percent dispersion as estimated by Equation 7

(a) Commercial



(b) 5-ALD

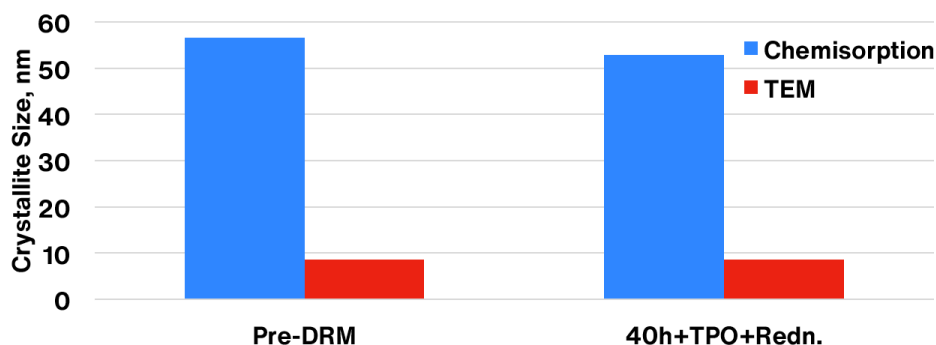


Figure 18 – Crystallite size comparison by chemisorption and TEM, before and after DRM reaction for (a) Commercial and (b) 5-ALD catalysts. Reprinted from [22]

From Figure 17 (a), the mean crystallite size of the pre-DRM Commercial catalyst is 8.4 nm as estimated by TEM. This is significantly lower than the 23.0 nm from chemisorption. We believe there could be two reasons for this large variation in crystallite size estimations from the two methods. Firstly, it is possible that since the chemisorption for the pre-DRM sample happens just after the reduction step, any carbonaceous material on the active Ni sites could reduce H₂ uptake, subsequently bringing down the estimated crystallite size. The 40h

DRM+TPO+Redn. sample has been through 40 h exposure of DRM and one oxidation cycle and can be expected to be relatively cleaner. As discussed by Silvester et al. [67], such redox cycles increase the degree of reduction and also do the job of cleaning the surface. Hence, an increased X in the pre-DRM sample will also bring down the gap between the estimations by TEM and chemisorption techniques. As shown in Figure 18 (a), the crystallite size from both methods being very similar for this post-DRM sample lends credence to this explanation.

Secondly, when the chemisorption measurement is made for the pre-DRM sample, the only preceding step is reduction with H_2 , as described in section 2.2.3. It could be that not all Ni is reduced in this reduction step and some Ni^{2+} is trapped in the catalyst bulk. From Equation 8, it is worth noting that the crystallite size estimated by chemisorption, d , is $\propto f$, i.e. proportional to the degree of reduction. The discrepancy in crystallite size measurements is likely due to an over-estimation of the f as determined by TGA oxidation experiments (0.97 for Commercial). A lesser f would bring the crystallite size estimations closer.

For the 5-ALD system, the low H_2 uptake, as shown in Figure 11, results in abnormally high crystallite size estimations. Equations 7 and 8 are derived for typical catalytic systems with active material exposed on a support. However, in the case of the 5-ALD catalyst, an amorphous alumina overlayer covers the active sites, affecting chemisorption. Therefore, using conventional chemisorption equations for estimating crystallite sizes would be inappropriate in this scenario without an additional parameter in Equation 7 to describe the extent of encapsulation. Hence, complementing the TEM with this chemisorption technique can give more information about the amount of Ni available for DRM catalysis. The estimated crystallite sizes from both methods might not match closely, as also noted by Bartholomew and Farrauto [39], nevertheless, the chemisorption technique described here is effective in measuring dynamic changes in in-situ dispersion which may be due to sintering and/or coking.

2.3.3. DRM performance Data

As discussed in Section 2, the objective of this work is to investigate the changes in the dispersion of different Ni catalysts with TOS in the DRM reaction. For reliable measurements

of chemisorption, 50 mg of catalyst sample was used. This is a relatively large amount of catalyst considering the maximum reactant flowrate of 150 mL/min used, and catalyst deactivation was not expected to be evident. It is therefore not reasonable to compare conversions to infer catalyst stability from this data set. However, to provide a complete picture of the experimental campaign, the average catalyst performance for ~40 h for all the catalysts tested is provided in Table 4.

Table 4 – Catalyst performance data for ~40 h TOS of DRM. Reprinted from [22]

| Catalyst | Average CH ₄ Conversion | Average CO ₂ Conversion | H ₂ /CO | Avg. Rate CO ₂ , mmol/min/g _{Ni} | Avg. Rate CH ₄ , mmol/min/g _{Ni} | Avg. Rate H ₂ , mmol/min/g _{Ni} | Avg. Rate Coke, µgC/h/g _{Ni} |
|------------|------------------------------------|------------------------------------|--------------------|--|--|---|---------------------------------------|
| Commercial | 69.8% | 78.8% | 0.77 | 60.8 | 53.3 | 105 | 0.31 |
| 5-ALD | 51.2% | 57.4% | 0.69 | 64.1 | 55 | 87.9 | 0.15 |
| 10-ALD | 18.3% | 21.3% | 0.9 | 25.5 | 22.2 | 45.6 | 0.36 |
| 20-ALD | 8.2% | 9.3% | 0.76 | 10.8 | 9.1 | 16.5 | n.d. |

n.d. – not determined. DRM conducted at 650 °C, 1 atm pressure.

The average CH₄ and CO₂ conversion for the ~40 h TOS for the commercial catalyst is ~70% and ~79% respectively. In comparison, the 5-ALD catalyst shows ~51% CH₄ and ~57% CO₂ conversions. The 10-ALD and 20-ALD catalysts show a much lower conversion and activity, possibly due to the relatively thicker overcoats hindering access to the Ni active sites underneath. Based on the ICP-OES results shown in Table 3, it is clear that Ni% in the commercial and 5-ALD catalysts are different. To provide a common basis to compare the catalysts, reaction rates are therefore reported per gram of the active metal (Ni). Note that the rates of CH₄ and CO₂ reactions are similar in both the commercial and 5-ALD catalyst. Since the amount of Ni present in the 5-ALD sample is less than in the uncoated commercial catalyst, the specific reaction rate of the 5-ALD is higher despite lower single-pass

conversions. This implies that the rates of CO₂ and CH₄ consumption per Ni site are comparable for both catalysts, which is interesting, considering the possibility for additional mass transfer limitations imposed by the ALD overcoat. Furthermore, considering the significantly lower dispersion observed for the 5-ALD catalyst than for the uncoated (Figure 12), the similarity in reaction rates per gram of Ni is perhaps of note. However, as noted above, the average conversions for these datasets are too high to be considered conclusive for the purposes of kinetics. More details on the catalytic performance of the reactor used as a function of catalyst weight and bed dilution are given in Appendix B.

The amount of coke deposited was estimated by integrating the TPO peak after the ~40 h runs. The rate of coke formation for the 5-ALD catalyst is 0.15 µgC/h/g_{Ni} which is almost half of that obtained for the commercial catalyst. Coking and sintering resistance of Pd catalysts over coated via ALD was first reported by J. Lu et al. [78] where the ALD alumina was theorized to block and stabilize edge and corner atoms responsible for the coking reactions. In the current study, the reduced coke formation rate is most likely linked to crystallite size changes. As shown in Figure 16, the crystallite size in the Commercial catalyst increased from 8.5 nm to 24.5 nm, while remaining almost unchanged at 8.7 nm for the 5-ALD catalyst. For steam reforming on Ni catalysts, Christensen et al. [69] found that the coking rate increased with increasing the crystallite size. It is generally understood that smaller Ni crystals have a higher corner/edge atom to terrace site ratio, which lowers the coking formation rate [79], [80]. This would explain the relatively lower carbon formation rate in the 5-ALD catalyst compared to the Commercial catalyst.

2.3.4. Conclusions

This work describes the use of a binary in-situ H₂-CO chemisorption technique for estimating the dispersion of the active metal in a catalyst, which, in this study, is an alumina-supported nickel DRM catalyst. This case study of a commercial nickel catalyst coated with varying layers of alumina by ALD demonstrates the applicability of this technique. No measurable chemisorption was obtained for catalysts coated with 10 and 20 TMA-H₂O ALD cycles, most likely due to the overcoat limiting access to the Ni active sites. In comparing a Commercial 20% Ni/Al₂O₃ catalyst with the same catalyst coated with 5 cycles of TMA-H₂O, the

chemisorption results reveal a more rapid fall in dispersion for the Commercial catalyst at $\sim 0.11\% \text{h}^{-1}$ as opposed to $0.025\% \text{h}^{-1}$ for the 5-ALD catalyst. Although the initial dispersion as measured by chemisorption is 1.7% for the 5-ALD catalyst when compared to the 4.2% for the Commercial catalyst, the alumina overcoat on the 5-ALD catalyst helps sustain the dispersion better, for the 40 h of DRM. TEM imaging confirms the extent of sintering in all cases. Average crystallite size for the Commercial catalyst increases from 8.5 nm to 24.5 nm, while for the same time-on-stream in the DRM atmosphere, the 5-ALD catalyst maintains its original average crystallite size of about 8.7 nm. This is further supported by the lower coke formation rate for the 5-ALD catalyst *vs.* the commercial nickel catalyst. Since the 5-ALD catalyst exhibited lower coking rate in addition to maintaining the crystallite size, a follow-up work of this study is to investigate the performance of catalysts coated with lower cycles of ALD, to ascertain if there is an optimal number of ALD cycles that gives the best performance.

In summary, this in-situ measurement technique not only provides information on changes in metal dispersion in the catalyst with time-on-stream but can also provide insight into the morphology of the active site, as it evolves over the course of the DRM reaction. Direct size measurement by TEM affords a more visual and accurate assay of selected crystallite sizes, but since in-situ TEM requires highly specialized equipment, the chemisorption method described here is a more expeditious approach for an in-situ study of the dynamic changes in the dispersion of catalysts.

3. PRETREATMENT METHODS FOR ALD CATALYST

The previous chapter showed how the ALD overcoat could help protect the catalyst active from coking and sintering. The activity was not studied since the amount of catalyst was high and the time scale was not enough to observe catalyst deactivation. Nevertheless, it is known that adding the overcoat to a high number (10, 20 cycles) and above causes a mass transfer limitation directly impacting the activity. In this chapter, the objective is to investigate the effect of different parameters on the ALD overcoat and the impact it has on catalyst activity. In the later part of this chapter, a Temperature Programmed Surface Reaction (TPSR) technique is described which could be a promising way to activate ALD catalysts, by making them more resistant against catalyst deactivation and simultaneously enhancing the catalyst activity and stability.

3.1. Design of Experiments Study³

Various parameters in the ALD deposition process could affect the overcoat characteristics, thereby affecting porosity. A systematic study to investigate these effects necessitates a Design of Experiments (DoE) Study for these ALD parameters. Three parameters were chosen as these are critical to the ALD process and they are listed below with the upper and lower values used in the study:

- Deposition Temperature (125 °C, 300 °C)
- Annealing Temperature (600 °C, 800 °C)
- Heating Rate (1 °C/min, 15 °C/min)

After the ALD deposition process with 20 cycles (20-ALD), the annealing was carried out as per the conditions shown in Table 5. After the catalytic experiments were performed, BET experiments were done to obtain BET Surface Area. These responses were then correlated with catalytic activity testing which is described in section 3.1.1. The schematic of the

³ This study was performed by Patrick Littlewood from Northwestern University and Daniel Curulla from TOTAL.

workflow is illustrated in Figure 19. The Full Factorial Experimental Design is shown in Table 5.

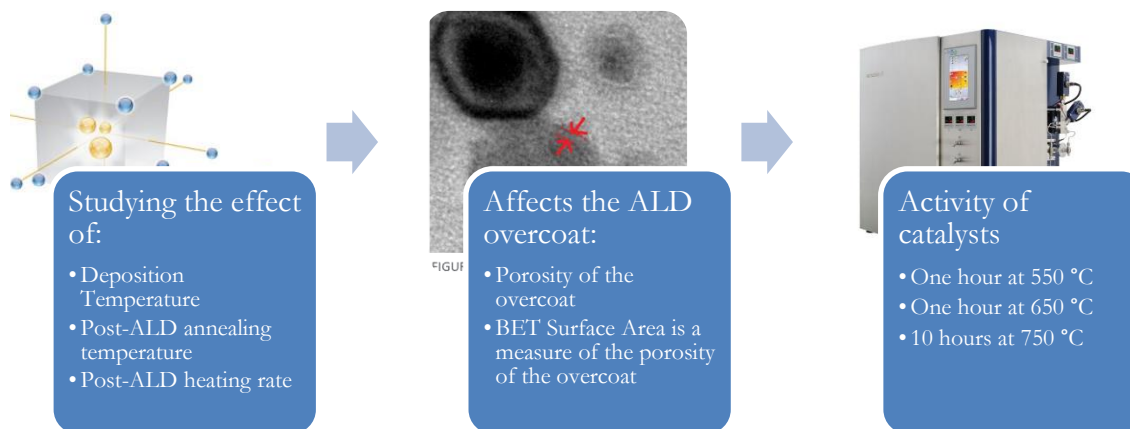


Figure 19 - DOE Parameters affecting ALD overcoat ultimately affecting catalyst activity

Table 5 - Experimental Design

| Experiment | Temperature of Deposition, °C | Temperature of Annealing, °C | Heating Rate, °C/min |
|------------|-------------------------------|------------------------------|----------------------|
| 1 | 125 | 600 | 1 |
| 2 | 300 | 600 | 1 |
| 3 | 125 | 800 | 1 |
| 4 | 300 | 800 | 1 |
| 5 | 125 | 600 | 15 |
| 6 | 300 | 600 | 15 |
| 7 | 125 | 800 | 15 |
| 8 | 300 | 800 | 15 |
| 9 | 212.5 | 700 | 8 |

3.1.1. BET and Activity Results for DOE study

The BET results for the 20-ALD catalyst are shown in Table 6 and indicate that the ALD temperature has a positive effect on the surface area. A higher ALD temperature gives a higher surface area. And this can be explained from the fact that a higher deposition temperature means the ALD overcoat has more energy and the mobility of the Al atoms means that they have a lesser chance of any agglomeration as compared to a lower temperature.

Table 6 - BET Results of 20-ALD catalyst

| Sample | TD (°C) | TA (°C) | HR(°C/min) | BET (m ² /g) |
|--------|---------|---------|------------|-------------------------|
| E1 | 125 | 600 | 1 | 44.0 |
| E2 | 300 | 600 | 1 | 69.4 |
| E3 | 125 | 800 | 1 | 50.7 |
| E4 | 300 | 800 | 1 | 68.7 |
| E5 | 125 | 600 | 15 | 58.1 |
| E6 | 300 | 600 | 15 | 66.8 |
| E7 | 125 | 800 | 15 | 48.9 |
| E8 | 300 | 800 | 15 | 66.0 |

The activity results provide further confirmation of the data obtained in the BET experiments. 5 mg catalyst was used in each case. The Weight Hourly Space Velocity (WHSV) was maintained as 360 Lh⁻¹g_{cat}⁻¹ and the feed gas flow had a composition of 10% CH₄, 10% CO₂, 2% Ar, and 78% He. The temperatures were varied in steps, at 550 °C for one hour, 650 °C for one hour, and finally 750 °C for 10 hours. The reactor was maintained at atmospheric conditions.

To highlight the effect of the Deposition Temperature, the activity results of samples E1 and E2 are shown, which have same annealing temperature and heating rate, but the deposition temperatures are 125 °C and 300 °C, respectively.

Figure 20 shows the CH₄ activity profile for the 12 h time-on-stream (TOS) and the E2 sample has higher activity than E1. There is not much of a difference in the H₂/CO ratio, which indicates that the kinetics at the active site has remained mostly unchanged and the difference is only due to the access to the active site.

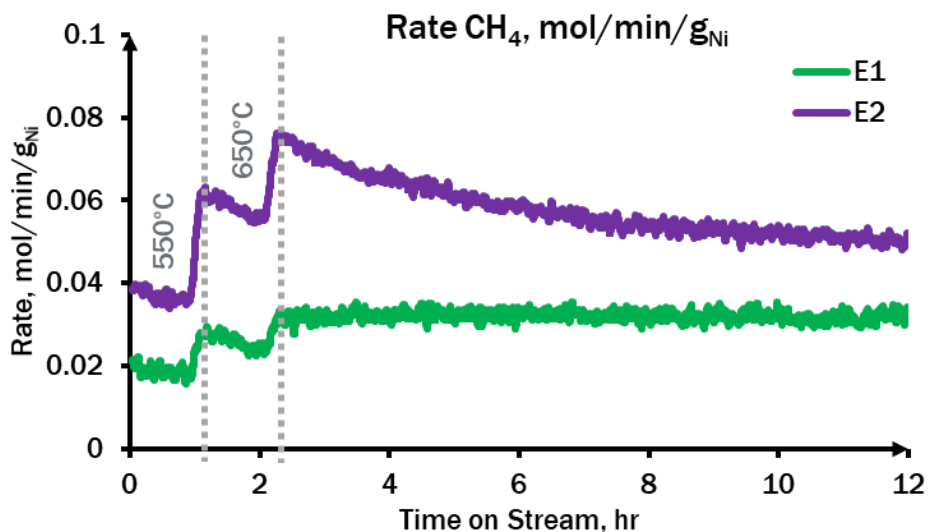


Figure 20 - CH₄ consumption rates for two different deposition temperatures (E1-125 °C, E2-300 °C)

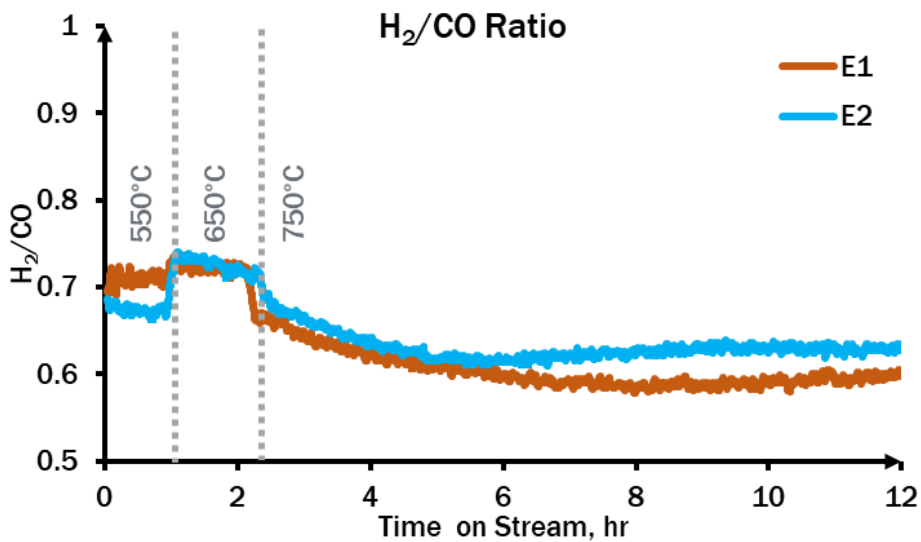


Figure 21 - H₂/CO Ratio

The CH₄ consumption rates for all the other runs are shown in Figure 22 and Figure 23 shows the comparison with the uncoated catalyst. As is evident, all the ALD catalysts show stability but a lower activity than the uncoated Commercial catalyst. The Commercial catalyst, however, has a high initial activity but exhibits a rapidly deactivating behavior. This is the case in many catalytic systems where the initial activity is sacrificed for long term stability.

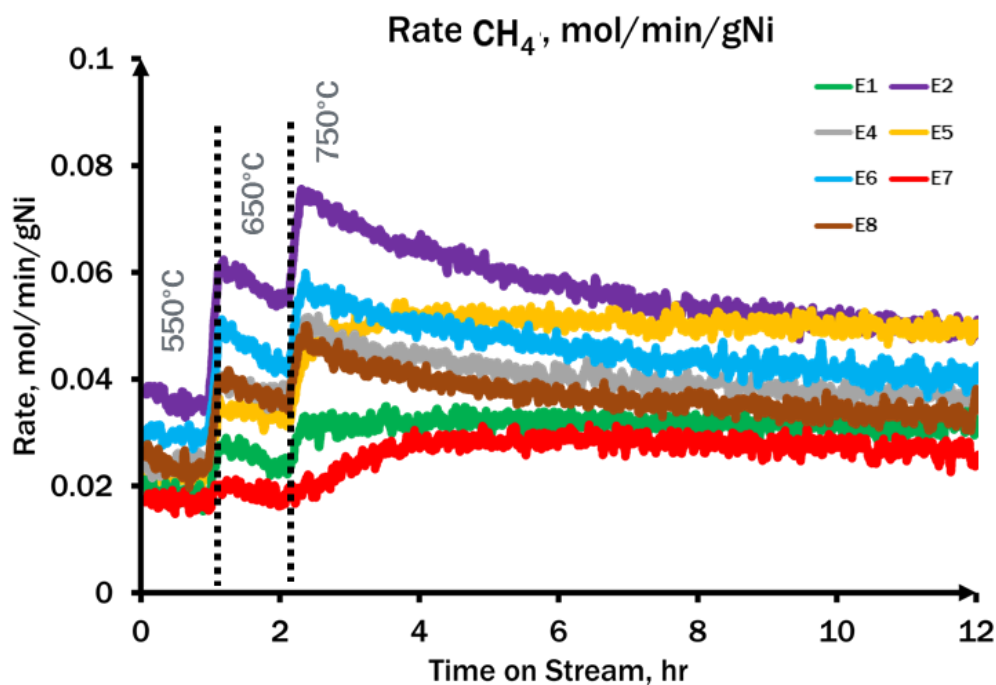


Figure 22 - CH₄ Activity Profiles for all samples

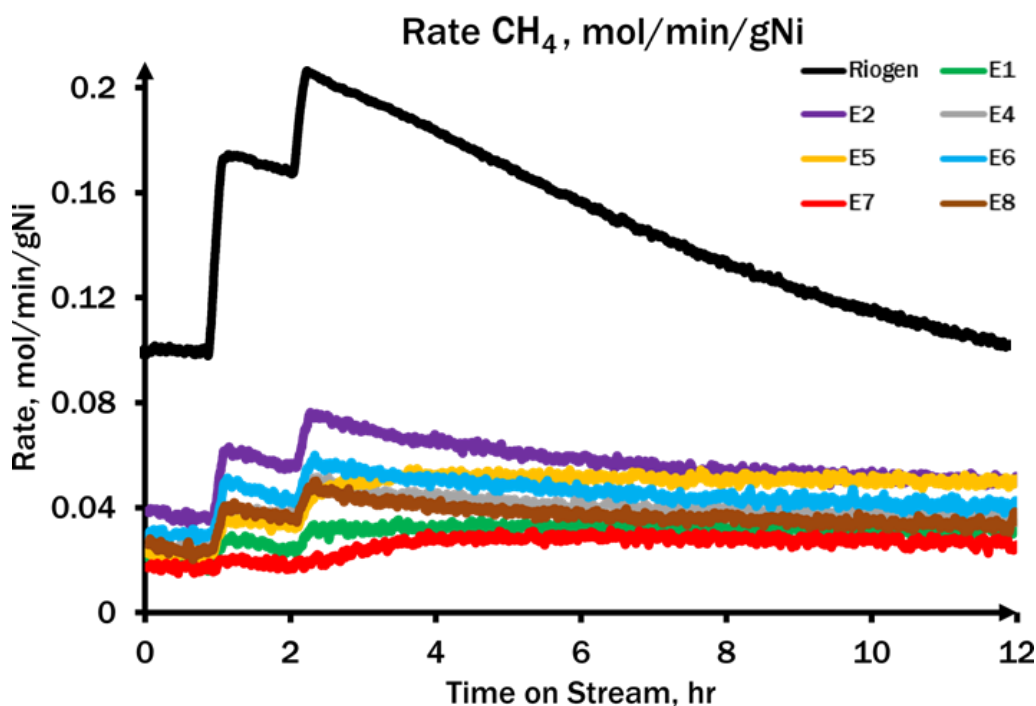


Figure 23 - Activity of ALD coated catalysts compared with Commercial uncoated catalyst

These experiments indicate that the ALD deposition temperature has the maximum positive impact on BET surface area and conversion. The next section describes an improvised annealing process which seems to modify the overcoat structure to have better activity performance than shown in these set of experiments.

3.2. TPSR as means of activating ALD catalyst

The ALD catalysts used here are prepared by the same procedure as outlined in 2.2.1. This section describes a Temperature Programmed Surface Reaction (TPSR) method which could possibly be used as a means to activate the ALD catalyst for better performance.

Temperature programmed techniques are used extensively by the catalysis community to gain insights into catalyst behavior. Temperature is ramped in the reactor at a predetermined rate. By studying the evolution of gases as time passes with increasing temperature, critical information of the catalyst like metal-support interaction, etc. can be deduced. Temperature

Programmed Reaction (TPR) is when H_2 is passed over the catalyst with the temperature being ramped up. A catalyst that reduces earlier indicates lesser metal-support interaction. Temperature Programmed Oxidation (TPO) is when oxygen is passed over a spent catalyst to oxidize the carbon deposited. The temperatures at which the CO_2 signal peak intensity is high indicates the type of carbon. These are broadly classified as Temperature Programmed Surface Reaction (TPSR) technique.

In this work, a TPSR experiment on the uncoated commercial catalyst as well as a 20 cycle ALD coated catalyst was performed. For this article, TPSR will be referred to the process of ramping temperature in process gas, which in our case is 10% CH_4 , 10% CO_2 , 2% Ar, rest He. By ramping the temperature of the reactor and passing DRM gas over the catalyst, we pass the catalysts through drastic conditions of high coking regimes. And this gives information on the catalyst. This kind of study has been performed by earlier researchers with interesting insights [81].

Depending on the nature of carbon formed, 'coking' negatively affects catalyst life either by selectively encapsulating active metal sites (fullerene-like) restricting access to reactant gases or via growth of filamentous nanotubes that usually have minimal influence on activity. The severe build-up of carbon eventually clogs reformer tubes, causing pressure drops leading to plant shutdowns while the catalyst is regenerated or re-packed. Carbon formation occurs to varying degrees over the entire range of possible DRM operating temperatures [39] but is less favorable thermodynamically at temperatures nearing industrial reforming conditions (> 850 °C). Sintering, on the other hand, is minimal at 500 °C but becomes pronounced as reaction temperatures reach these industrial operating conditions. Sintering deactivates a catalyst by accelerating the loss of active metal and support surface area. These challenges are by no means specific to Methane Reforming but are endemic to any industrial process which relies on heterogeneous catalysts, and therefore, addressing the issue of catalyst deactivation has and continues to be a subject of significant interest to researchers in this area. One approach to overcome said limitations is through the synthesis of highly stable, yet active catalysts for DRM. Considering their very high activity and stability, choosing noble-metal catalysts such

as Palladium and Rhodium is undoubtedly the superior option, but their significantly higher cost prohibits their widespread use in the industry. Therefore, relatively inexpensive transition metals, specifically Nickel, are preferred over their more expensive counterparts despite their tendency to deactivate faster.

To mitigate their inherent limitations, research over the past few decades have been directed toward improving Nickel-metal dispersion, achieving smaller crystallite sizes, and better metal-support interaction. Non-conventional synthetic techniques have been investigated as well as the addition of promoters, varying the types of supports, alloying with other active metals even using different supports. Another, more recent technique involves the formation of a protective film or coating around the active catalyst site via techniques like sol-gel, vapor deposition including Atomic Layer Deposition. The concept of these so-called ‘core@shell’ catalysts is gaining traction with the DRM catalysis community primarily due to their reported ability to resist deactivation by sintering and coking of the underlying metal even after very long times on stream.

ALD as a means of catalyst synthesis enables precise control of the deposited film thickness even down to the Angstrom level, hence the moniker ‘Atomic’ Layer Deposition. The technique generally involves sequential, self-limiting surface reactions of two precursors, typically in the gaseous state, with a solid substrate. ALD is a physical vapor phase deposition technique with advantages over conventional chemical vapor deposition (CVD) due to its capacity to deposit highly conformal overcoats with precise thickness and desired composition. Recent advances in scaling up this technology for micron to nano-range powders have generated immense interest in the application of ALD for high-throughput synthesis and coating of catalyst particles [26], [82], [83]. A challenge with using ALD as a means of anchoring down metal crystallites is the nature of the overcoat itself, particularly as the thickness of the overcoat layer increases. This deposited layer imposes additional mass transfer limitations on the reactant gases attempting to gain access to the active metal underneath. To overcome these limitations, the overcoated catalysts have to be pretreated or ‘activated’ to sufficiently increase the porosity of the overcoat. Activation or pre-treatment of

heterogeneous, industrial catalysts, in general, involves controlled calcination, reduction, and/or selective poisoning steps [39]. Careful activation determines the activity, stability, and even selectivity of the final catalyst.

In this chapter, the TPSR as a possible way for activation of a commercial 20 wt% Nickel on Alumina catalyst modified by ALD has been described. DRM gas is passed over the catalysts while ramping the temperature to 800 °C @ 5 °C/min. The temperature ramp creates thermal stresses, thereby possibly rearranging the ALD alumina. This rearrangement has a positive effect on catalyst activity. During the TPSR experiment, the amorphous alumina overcoat deposited by ALD anneals and acts as a secondary substrate for anchoring redispersed Ni crystallites, generated during the annealing process. In addition, a closer look at the catalyst behavior during the TPSR activation process, TEM, SEM images of the catalyst, and Raman spectroscopy provide insight into the effect of the ALD overcoat on enhancing the DRM performance. Interestingly, the type of carbon formed on the ALD catalyst after the TPSR is also distinctly different from that on the Commercial catalyst, thereby opening up a new avenue of exploration for high-value carbon production via ALD catalysts.

3.2.1. TPSR Protocol

All catalyst performance experiments were performed in a compact Microactivity Effi unit from Micromeritics Inc. (USA). A schematic of the experimental setup is shown in Figure 24. Approximately 5.5 mg of catalyst and 505.5 mg of quartz sand (diluent) was loaded into a 9.2 mm diameter quartz reactor. The sample was dried under Helium for 2 hours at 150 °C followed by reduction in 10% H₂/He, ramping the sample temperature until 650 °C at 5 °C/min and holding at that temperature for 1.0 hour. The system was then purged with Helium while cooling down to ambient temperature. The next step is the TPSR which is the highlight of this study. Since this is the first time the ALD overcoat will experience higher temperatures, it can also be termed as ‘annealing’. A mixture of 10%CH₄:10%CO₂:2%Ar diluted in Helium is passed through the catalyst bed at 30 ml/min and the temperature is gradually ramped at a rate of 5 °C/min until 800 °C and held at that temperature for 1.0 hour. This ramping process is called TPSR. The TPSR is followed by purging the system with He. The temperature profile of the reactor during this TPSR process is shown in Figure 25. The

gas analysis of the reaction products is acquired via Cirrus 2 Residual Gas Spectrometer (MKS Instruments, UK).

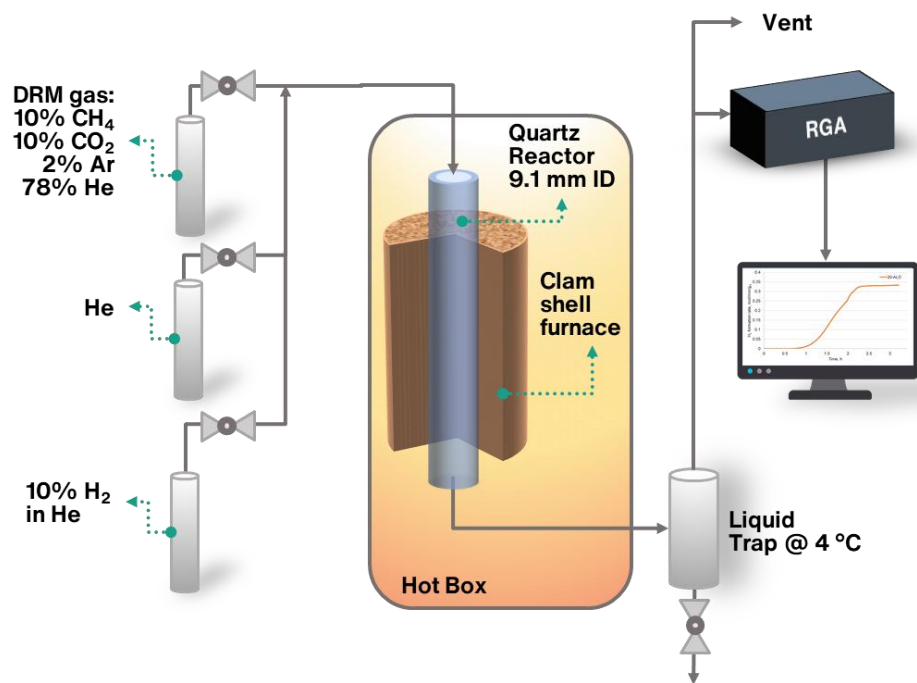


Figure 24 - Experimental Setup for TPSR

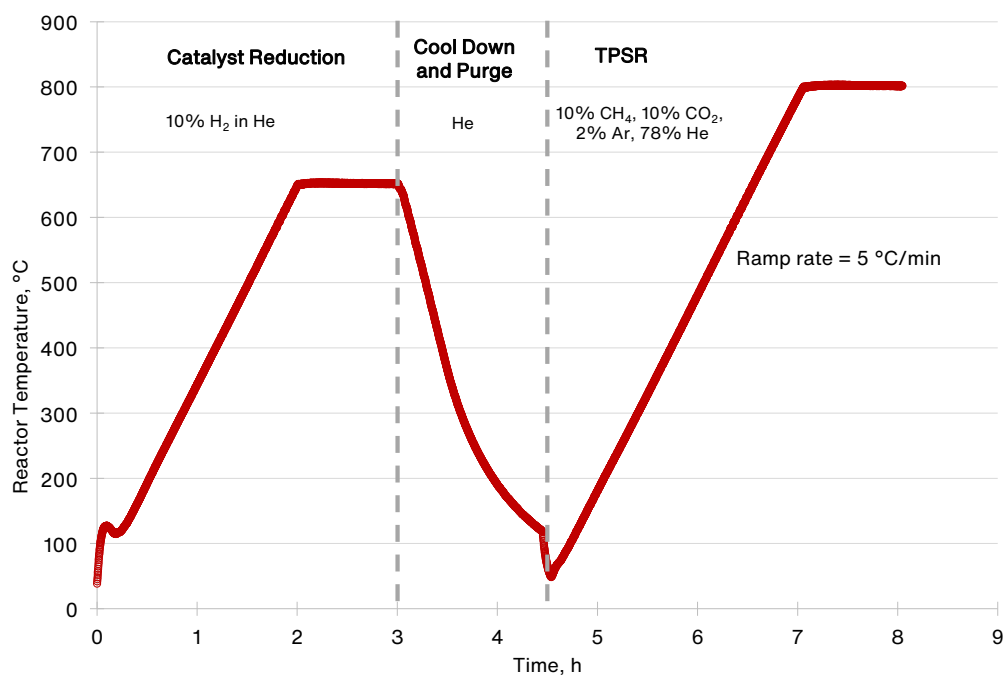


Figure 25 – Catalyst Reduction and Reactor Temperature Profile in the TPSR experiment

3.2.2. TPSR Study – Catalyst Performance and TGA Results

Catalytic Activity Comparison

The CH₄ and CO₂ conversions, H₂/CO ratio, and activity rates in mol/min/g_{Ni} with time for both catalysts, Commercial and 20-ALD, are plotted in Figure 26. Since the amount of active metal (Ni) differs in both the catalysts, a fairer metric to compare catalyst performance is the activity normalized per g of Ni. As shown in Figure 26, as the temperature reaches about 400 °C, which is after an hour, the CH₄ and CO₂ conversions and activity rates start to rise. The carbon formation reaction of methane decomposition is more active in this temperature range, and some activity can also be contributed by the DRM reaction. This also explains why the rate of methane consumption and CO₂ consumption rates are similar. In a pure DRM reaction system, due to the thermodynamics of the reverse water-gas-shift reaction (rWGS), the CO₂ reaction rates are slightly higher than CH₄ rates, as is seen at later temperature ranges. After the reactor has reached the maximum temperature of 800 °C, the 20-ALD catalyst

sustains the activity and shows a typical DRM performance, with the evolution of H₂ and CO. However, the activity of the Commercial catalyst starts to dip after reaching 800 °C. Typically, when a catalyst is coated with any type of overcoat, it is usually expected that the reaction rates will drop due to the additional mass transfer limitation. The objective of adding an overcoat is usually to address the problem of catalyst stability at the expense of sacrificing some access to the active sites and hence reaction rates [62]. However, the results from the current work indicate that this unique combination of ALD and TPSR could provide a pathway to address both challenges. The direct use of 20-ALD catalysts at a particular temperature does not show this behavior. The activity starts quite low and shows a very slow increase, which was further investigated and explained by Littlewood et al. [62]. In comparison, here, it can be seen that with the application of temperature ramp, the activity of the Ni catalyst can be enhanced when compared to that of an uncoated one with 3-4 h of TPSR.

The fluctuation in the H₂/CO ratio in the Commercial catalyst for the first one hour is due to the lack of the CO signal. In the absence of the CO signal, the H₂/CO ratio becomes a very large value. The amount of CO being generated is not enough to make the H₂/CO ratio within the scale of 0-1. In comparison, the H₂/CO ratio plot for 20-ALD shows a much more stable value fluctuating between 0.4 and 0.6 and plateaus around 0.8 towards the end of the run.

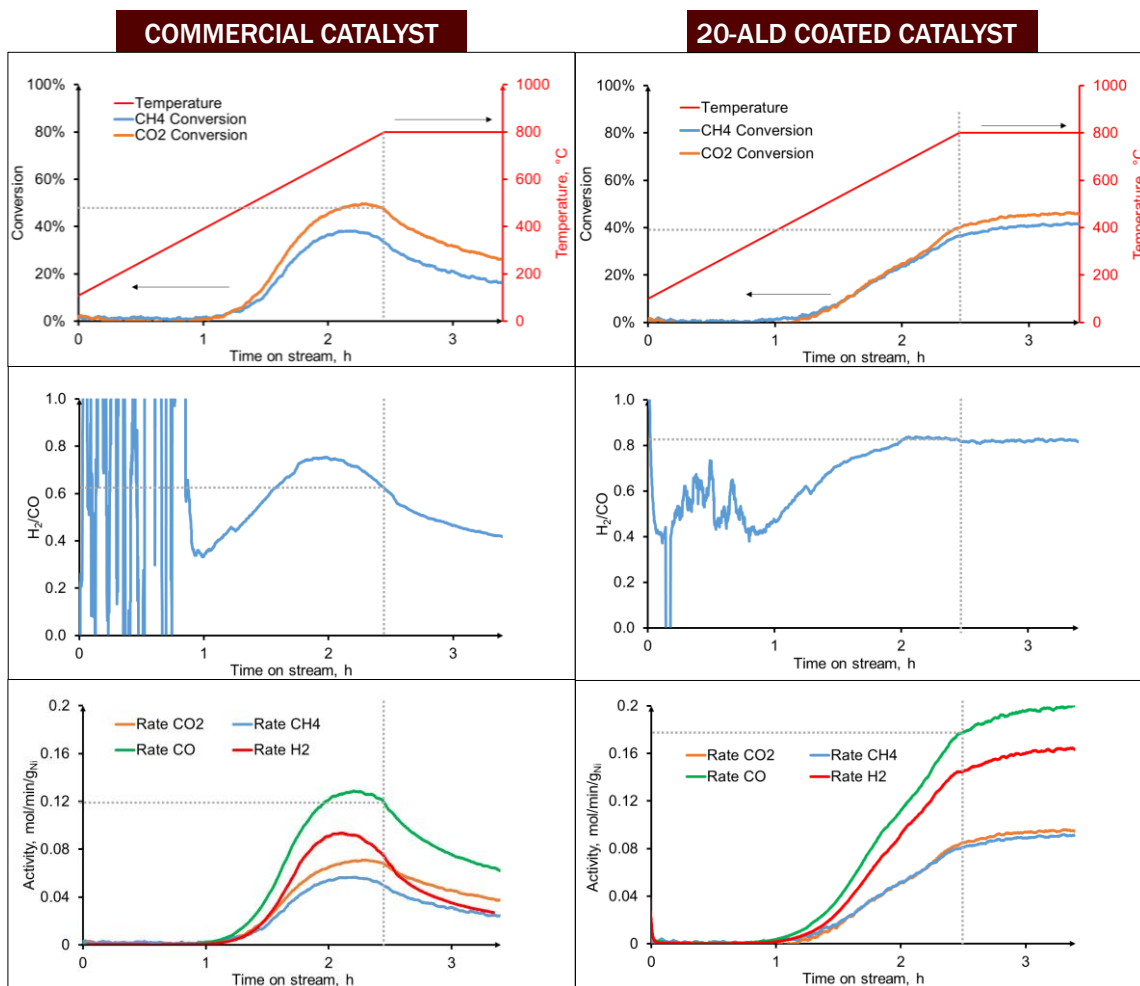


Figure 26 – Comparison of catalytic performance of Commercial and 20-ALD catalysts during TPSR

Contrary to expectations, the 20-ALD catalyst shows good activity (per g Ni) comparable to the uncoated catalyst and also shows better stability throughout the TPSR experiment. We believe the reason for this phenomenon is the increase in dispersion of the Ni active sites throughout the ALD alumina. The temperature ramp provides the necessary annealing conditions for the restructuring of alumina and thereby providing a new medium for the Ni to disperse in. Interestingly, a similar approach was used by Danghyan et al. [84], who reported an increase in catalyst dispersion by application of high pressure on the catalyst during the catalyst synthesis process. They used impregnated Ni on SiO₂ catalysts, diluted it

with fumed SiO_2 support, and then applied pressure in a press to form a pellet which was then broken down to powder. Pressure was applied to both catalysts, with and without fumed silica. It was found that the catalyst, which was diluted with fumed silica, had appreciably more activity than the one without fumed SiO_2 . They explained the increase in activity by stating that the transport of Ni in the fumed silica with the application of pressure was the reason for the increase in catalyst dispersion.

Our TPSR follows a strikingly similar procedure, as shown in Figure 27. In their case, pressure forces Ni to disperse in the new medium. And in our case, we believe the Ni movement through the ALD overcoat whilst being temperature treated is the reason for the better than expected activity of the 20-ALD catalyst. In both cases, an additional medium is needed for the catalyst to disperse in and a driving force is needed for the active metal to disperse in.

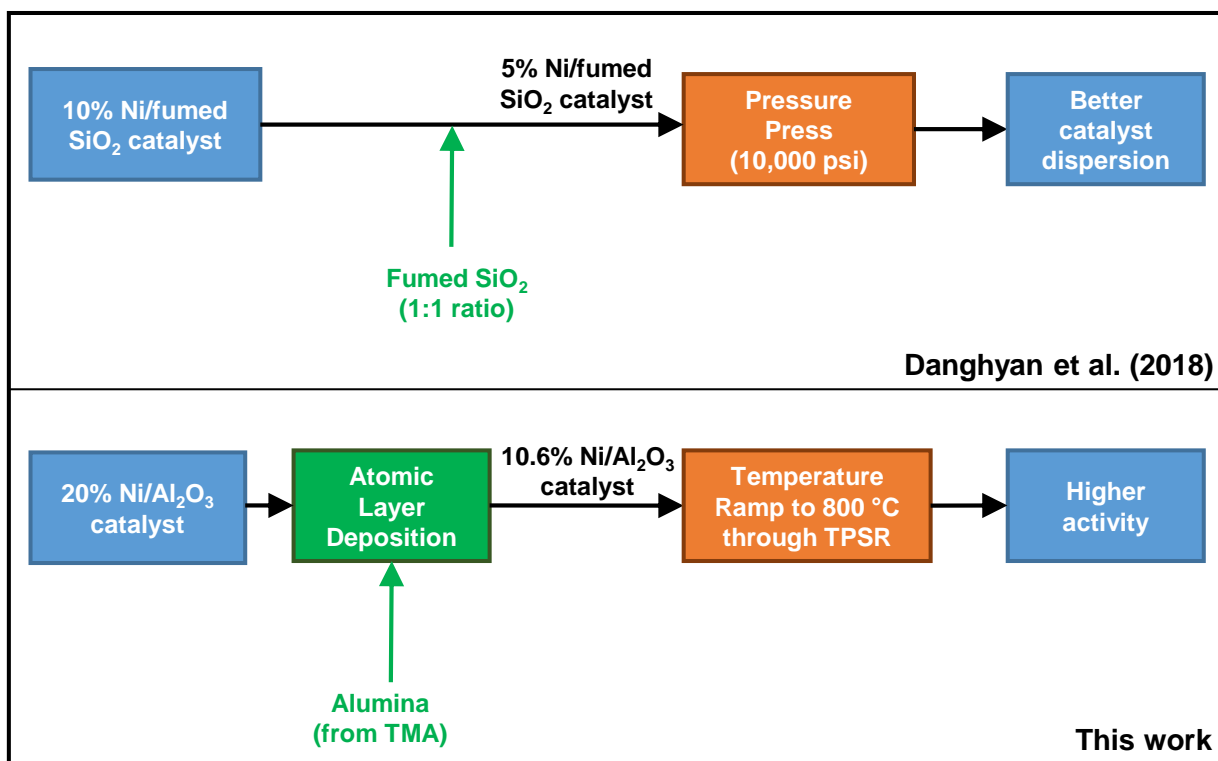


Figure 27 - Comparing TPSR with Pressure Dilution

Two repeat experiments were performed with different batches of catalysts to ascertain the reproducibility of the TPSR behavior. All runs show the characteristic behavior as described earlier. Figure 28 shows the results for 5 mg catalyst and Figure 29 shows the results for 2.5 mg catalyst. The results for 2.5 mg catalyst are slightly different than the one for 5 mg catalyst. The 20-ALD catalyst shows a slightly lower activity compared to the Commercial, yet the slopes of the activity plots toward the end indicate that the Commercial catalyst shows deactivation whereas the 20-ALD catalysts either stay stable or show increasing activity. In either case, the TPSR effect is evident which was unseen in experiments with 20-ALD at a fixed temperature.

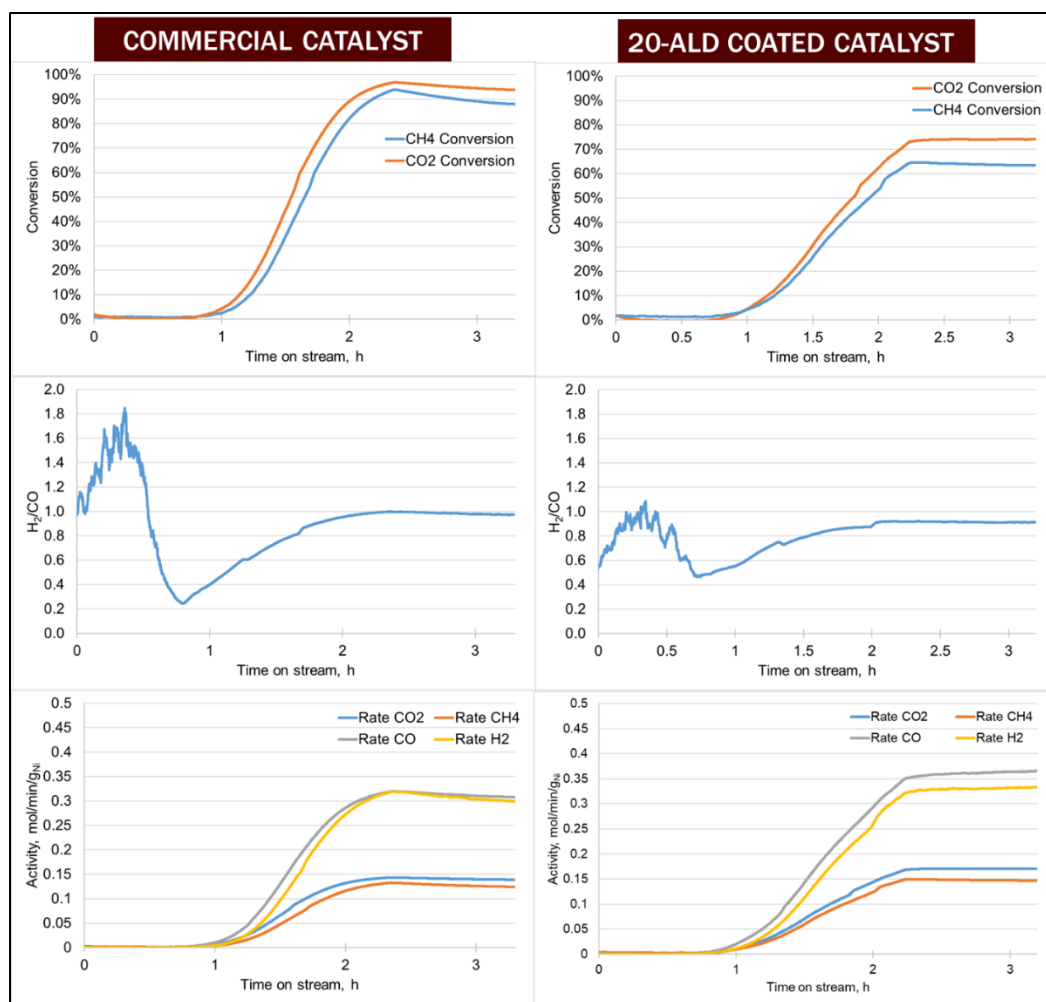


Figure 28 - Repeat TPSR Experiments - 1

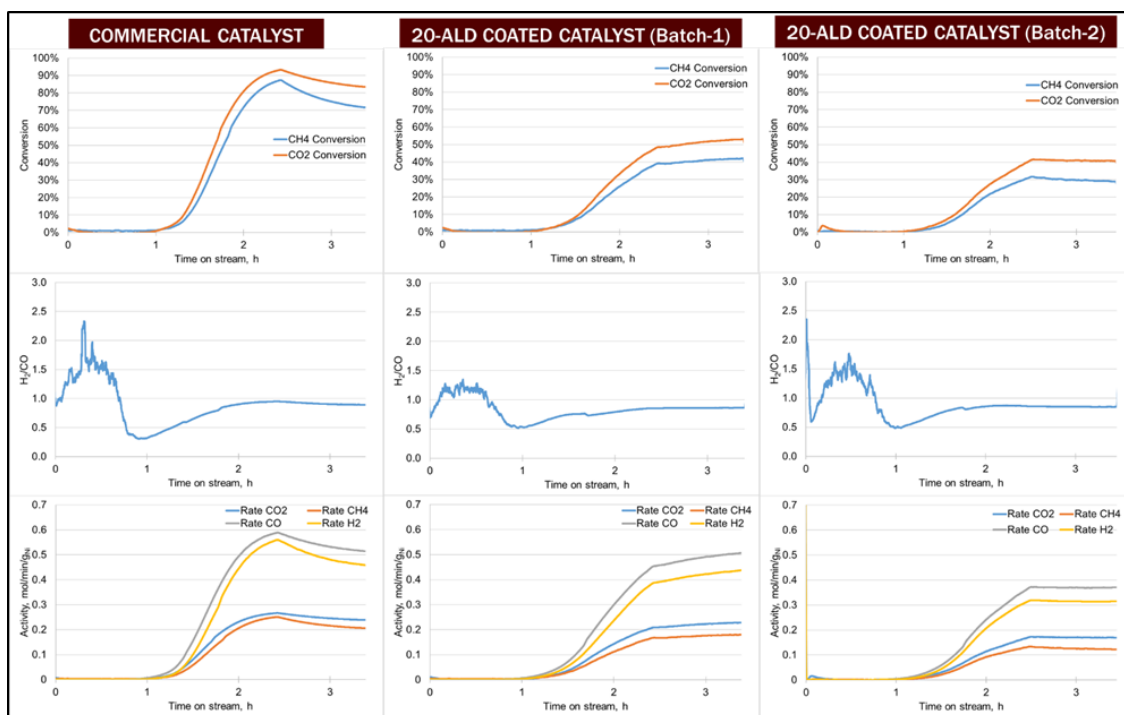


Figure 29 - Repeat TPSR Experiments - 2

TGA Results

A Thermo-Gravimetric Analysis (TGA) was done for the Commercial and 20-ALD catalysts and the results are shown in Figure 30. Since reduction was not possible in the TGA setup, the catalysts had to be reduced externally and then transferred to the TGA for the TPSR experiment. Hence, when the DRM gas starts flowing onto the catalyst, there is some instant catalyst reduction, which is evident from the dip in the catalyst weight. The reduction in catalyst weight is due to the escaping H₂O molecules after reduction. We notice that both the catalysts show an increase in weight and the slope is much steeper at the beginning but starts to become less steep in the second half. The TGA plot of Figure 30 shows cumulative changes in weight. To study the differential changes in weight at different temperatures, the differential weight gain is plotted in Figure 31 for the specific region where coke formation takes place.

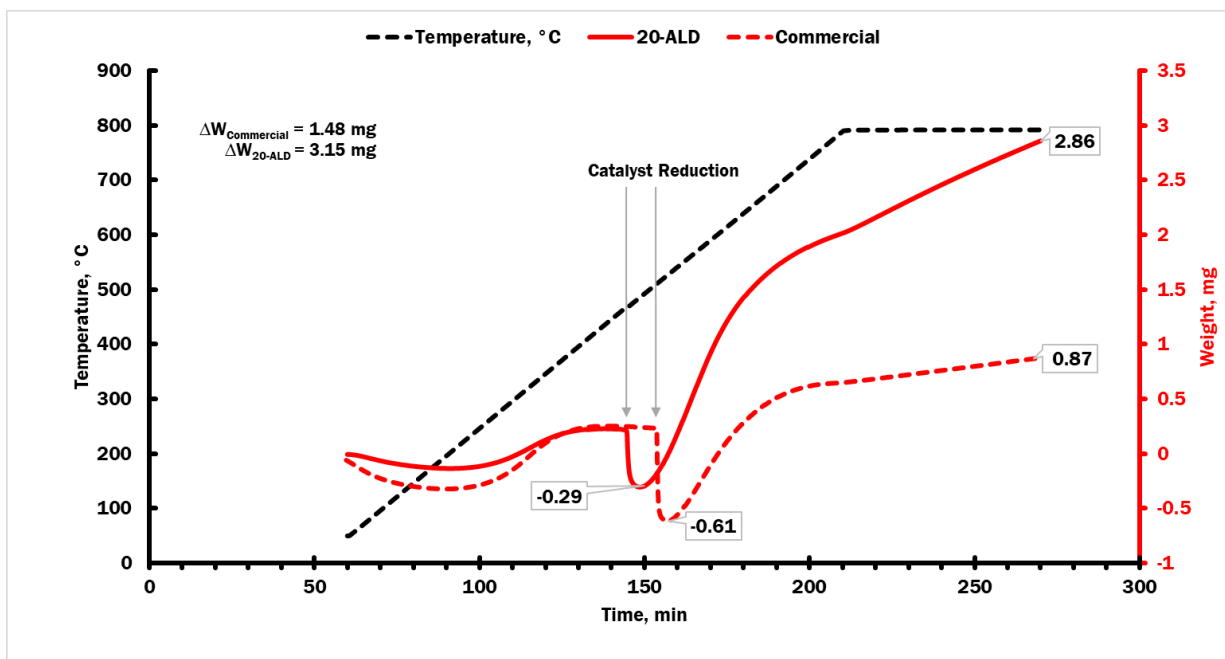


Figure 30 - TGA plots for Commercial and 20-ALD catalysts

The amount of carbon formed on the 20-ALD catalyst is much more than the Commercial catalyst, as shown in Table 7. Comparing this with the activity information in Figure 26 indicates that the 20-ALD catalyst seems to be more active continuing to sustain DRM activity and simultaneously producing carbon. But in the Commercial catalyst, the exposed active sites are quickly encapsulated by the carbon formation and deactivates rapidly. Hence, both the activity, and the carbon formation rates, are lesser than the 20-ALD catalyst.

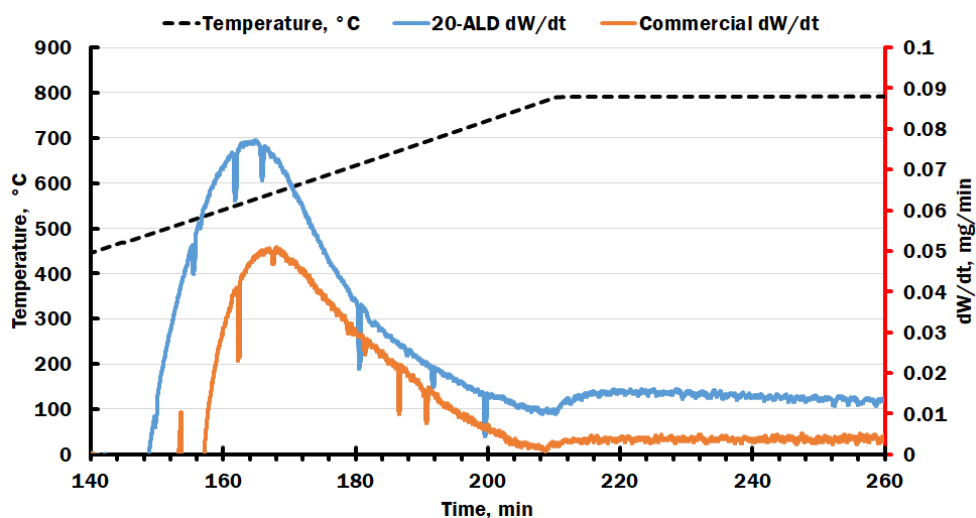


Figure 31 - Differential changes in weights in TGA

Table 7 - Comparison of coke formation rates in TGA experiment

| | Commercial | 20-ALD |
|-----------------------------|------------|--------|
| Ni% (from ICP-OES) | 17.1 | 10.6 |
| ΔW , mg | 1.48 | 3.15 |
| Weight of catalyst, mg | 5 | 5 |
| Time, min | 115 | 125 |
| Coke formed, mg C/mg Ni/min | 0.1505 | 0.4755 |

3.2.3. TPSR Study – Images from SEM, TEM and Raman

SEM Imaging

The spent catalyst samples of both Commercial and 20-ALD were viewed in an SEM microscope and the comparison is shown in Figure 32. The morphology seems distinct in both the spent catalyst samples. The commercial catalyst samples show a typical image of spent catalysts. The shiny part in the back-scattering image is the exposed metal surface. Back-scattering images are helpful to detect higher atomic numbers (heavy elements) than lower atomic numbers, as they appear brighter in the SEM image.

In the 20-ALD catalyst, a distinct feature of the particles is the cracks. These cracks are about 250 nm in width. From the back-scattering image, the shiny surface indicates either Ni or Aluminum (as this is the 20-ALD catalyst). The cracks do not appear in the uncoated catalyst sample and hence, it is highly likely that the ALD overcoat is responsible for the cracks. Cracks in ALD thin films have been reported in the literature. Baumert et al. [85] studied fatigue properties of Si thin films coated with ALD alumina with thickness from 4.2-50 nm. Fatigue tests were done by a resonator and from SEM images, they found cracks of about 50 nm thickness, but they were for the sample with 358 cycles of TMA-Water ALD. In our case, with 20 cycles of ALD, the formation of large cracks of the order of 250 nm can only occur if the alumina deposition has been more than the usual expected. Deposition rates being higher than nominal values is normal in ALD deposition studies [85], but it seems it is much higher in our case. Nevertheless, the reason for these cracks can be attributed to the temperature annealing process. Thermal stress can cause alumina to have cracks. Thermal stress has some other effects on the Ni crystallites at the particle level and this is discussed in the next section which analyzes TEM images.

When ALD is used for barrier applications, the goal is to keep the films without cracks [86]. But in applications like catalysis, some cracks might be advantageous to enhance reaction rates whilst utilizing the benefit of the ALD overcoat. It seems plausible that the cracks are serving a purpose and could facilitate more access to Ni below.

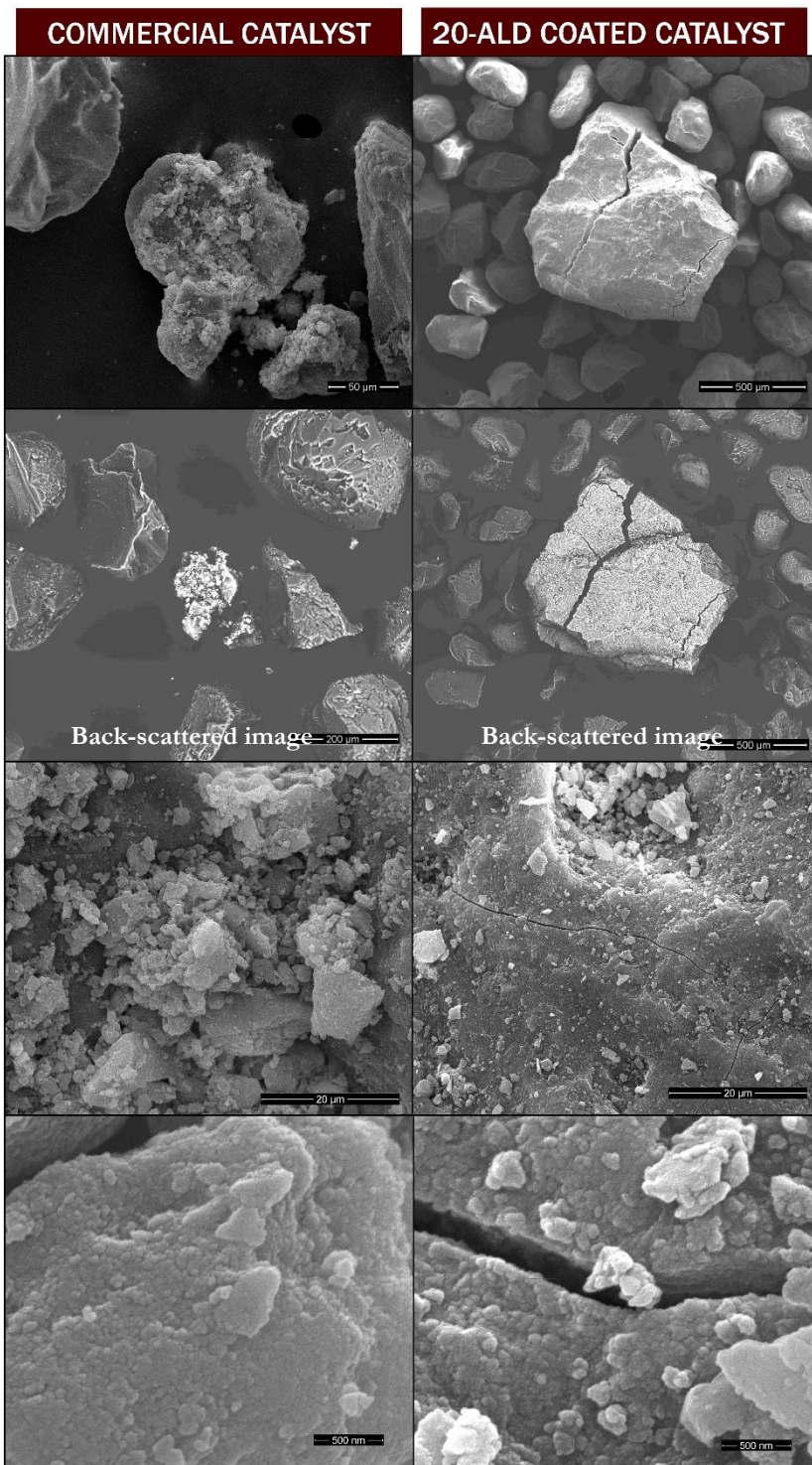


Figure 32 - Comparison of SEM images after TPSR

TEM Imaging

TEM images were taken at different resolution levels to compare the spent catalyst samples of the Commercial and 20-ALD catalyst, and are shown in Figure 33. The elemental mapping of the samples for Al (magenta), C (red) and Ni (blue) are included. The high-resolution image for the Commercial catalysts does show some carbon around the Ni crystallites, though mostly in the amorphous graphitic form.

Interestingly, the HAADF-STEM image of the 20-ALD catalyst has distinct thread-like structures as shown in Figure 33. The first guess was that these are probably multi-walled carbon nanotubes as their diameter is about 10 nm. However, to our surprise, the elemental mapping image showed that the thread-like structures are aluminum. Figure 34 shows the superimposed image of the thread-like structure with the aluminum map and it exactly matches in the two, indicating that the thread-like structures are aluminum.

We hypothesize that the source of these thread-like or needle-like structures in the TEM images of the 20-ALD catalyst is from the ALD over coated alumina. The crystalline alumina support from the Commercial catalyst does not probably play a role in this phenomenon since the TEM images of the uncoated Commercial catalyst do not show any such features, as shown in Figure 33. The temperature ramp in the DRM gas conditions has induced stress in the ALD overcoat and restructured the alumina into the form shown. From the higher activity and carbon formation rate, we hypothesize that this rearranged alumina provides the larger surface area for the Ni to disperse thereby increasing the activity and keeping the Ni exposed. This explanation fits quite well with the hypothesis presented in section 0 and the TEM images lend credence to our hypothesis. Additionally, Karwal et al. [45] studied the formation of nanopore formation on alumina ALD films of ~ 4.9 nm thickness overcoated on γ -alumina nanoparticles. From a modeling study and in-situ SAXS experiments, they found that the annealing temperature had a big effect on the pore radii. The pores started appearing in the 400-500 °C range with a pore radius of ~ 1.5 nm and when the temperature was increased to 1000 °C, the pore radius increased to ~ 1.9 nm. They proposed that the pore formation was

driven by relieving the stress of stressed films due to phase transition of ALD films and/or thermal mismatch between film and substrate. And this matches our system where the substrate is crystalline γ -alumina from the Commercial catalyst, and the ALD overcoat is alumina deposited by our ALD process. Since we have not used in-situ TEM, we are unable to verify if the thread-like structures too start to form around these temperatures. From the TEM images, the thread-like structures have a diameter of about 4 ± 0.5 nm. Similar to the hypothesis we provided in section 0, if the thread-like structures are indeed pores, as suggested by Karwal et al. [45], then they may very well provide the necessary pathway to the reactants till the Ni active sites.

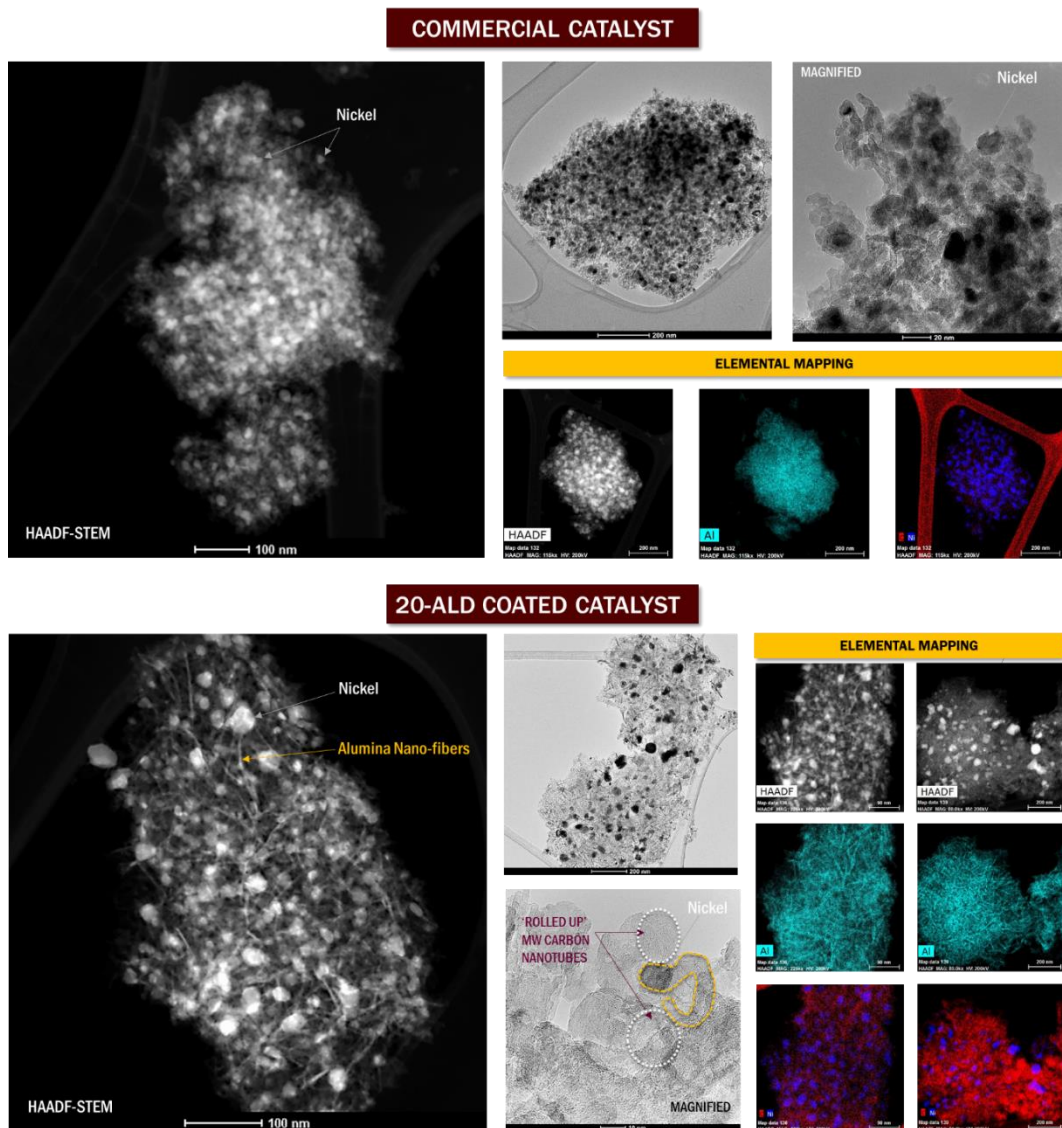


Figure 33 - TEM images of catalysts after TPSR

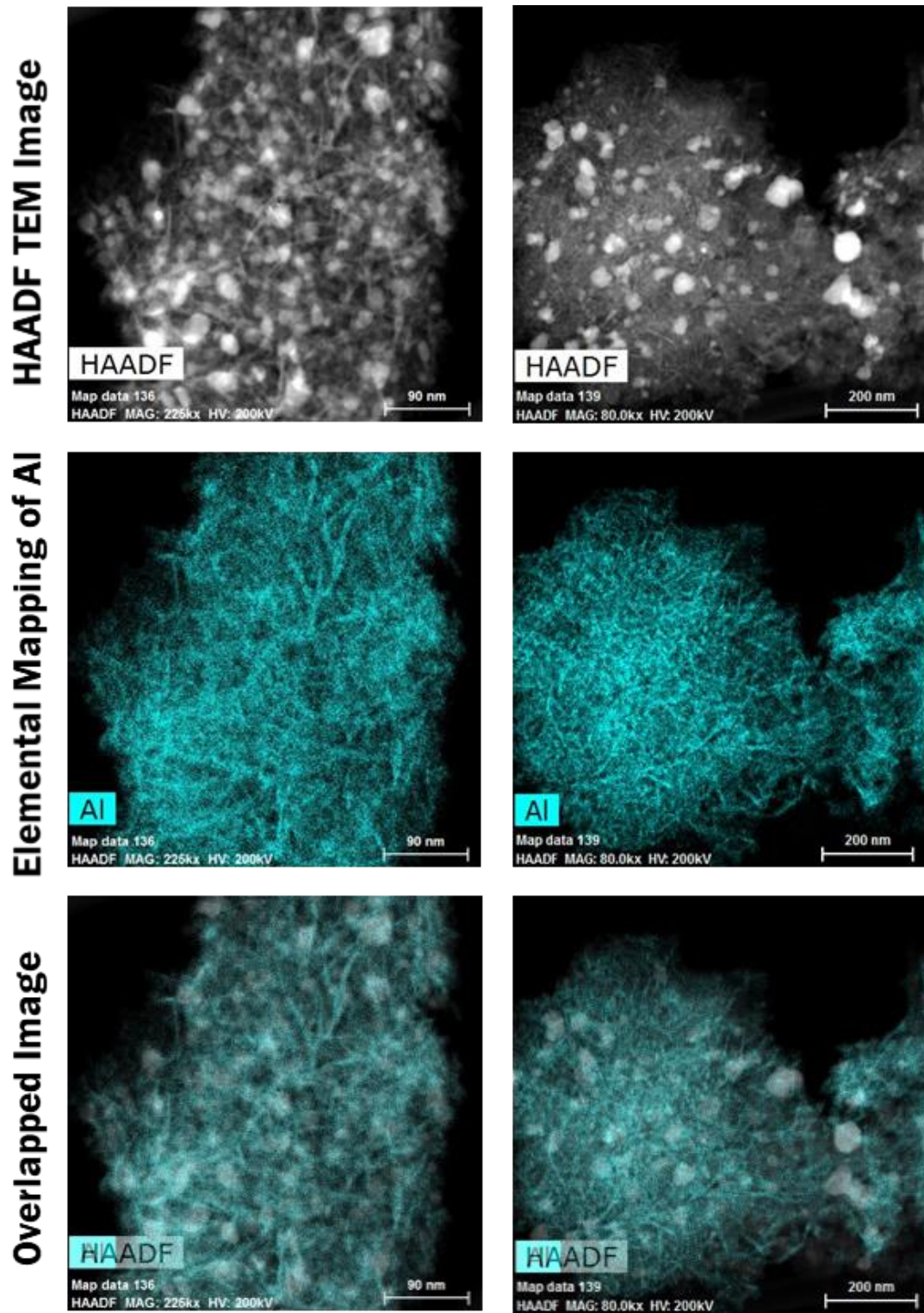


Figure 34 – Magnified images and overlap to show that the needle-like structures are from the amorphous overcoated alumina

Detailed High-resolution imaging to the order of 20 nm shows an interesting carbon formation images in the 20-ALD catalyst. Figure 35 shows a high-resolution image of the spent catalysts of the Commercial and 20-ALD catalyst, focusing on the carbon formed. The Commercial catalyst shows the carbon formation; there is some orderly arrangement but overall, it appears more amorphous. The 20-ALD catalyst image shows distinct layered structures. While some are elongated concentric circles, there are numerous of these structures visible in the TEM images and they are highlighted. These structures have a striking resemblance to carbon onion images from the literature [87], [88]. Carbon Onions are a recent topic under investigation in the carbon community and they are usually described as a few enclosed fullerene-like layers or concentric graphitic shells with a hollow inside, nanodiamond core or fullerene at the center [89].

These onion-like structures are distinct only to the 20-ALD spent catalyst samples. We suspect that the confinement effect by the 20-ALD overcoat along with the temperature ramp is providing the necessary conditions to produce these carbon-onion like structures. Some evidence from Raman, as described in the next section, also supports this hypothesis.

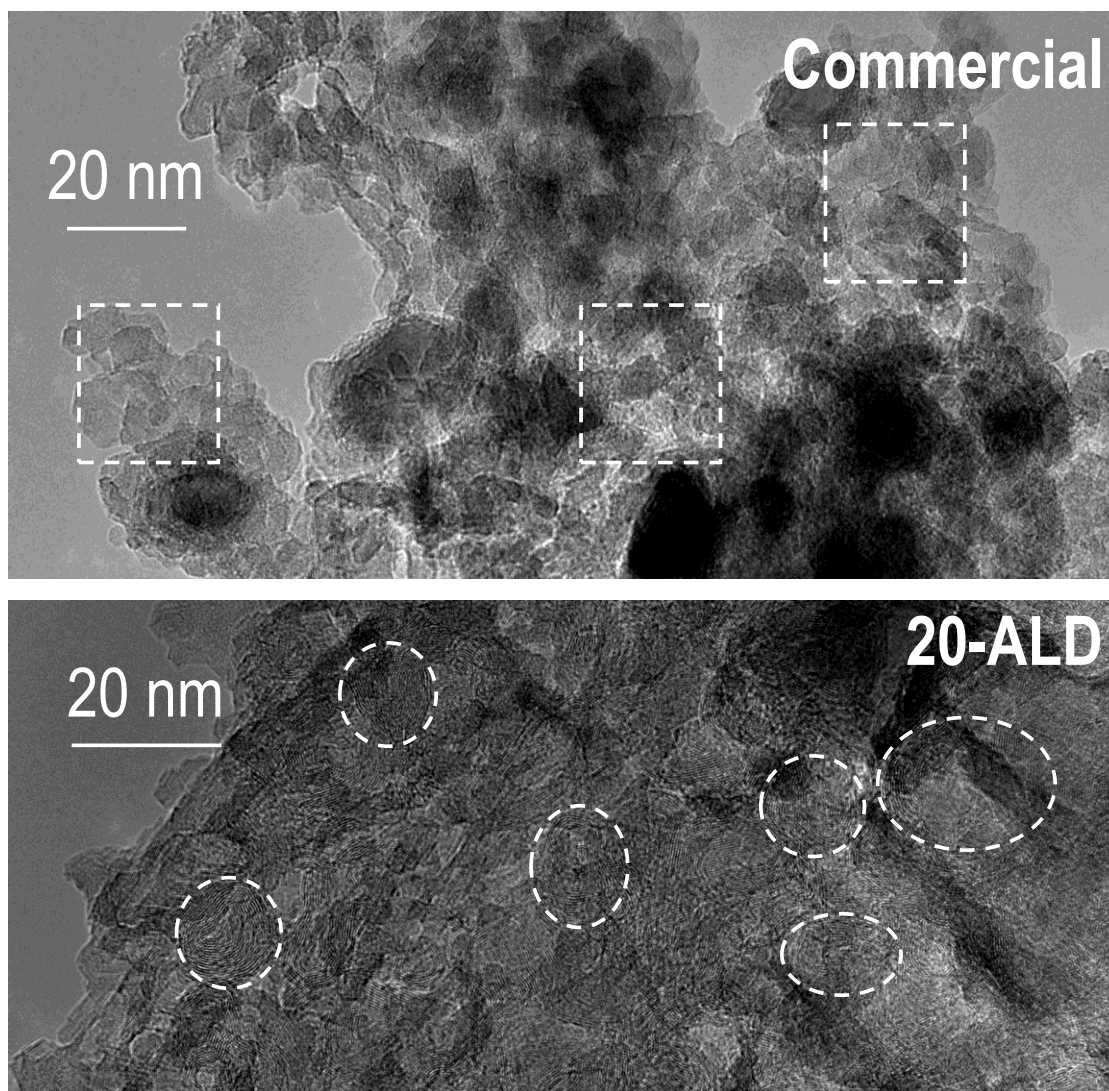


Figure 35 - High-Resolution Images of carbon morphology on Commercial and 20-ALD catalyst

Raman Spectroscopy

Raman spectroscopy was carried to reveal the structural characterizations of the Commercial and 20-ALD catalyst samples, and the spectrum is shown in Figure 36. The Raman spectra of both samples exhibited two characteristic bands, namely D-band ((the symmetric A_{1g} mode) positioned at around 1342 cm⁻¹ attributed to the presence of disordered amorphous carbon and G-band ((E_{2g} mode of sp² carbon atoms) positioned at around 1581 cm⁻¹

corresponded to the tangential vibration of the graphitic carbon atom [90]. The 20-ALD sample exhibits a more prominent D-band, which shows multiwall configurations and indicates more disorder in the structure [91]. The ratio of D and G band intensities can be used to estimate the number of defects in graphitic lattice [92]. As can be seen from Figure 36 and Table 8, the intensity ratio (I_D/I_G) in the 20-ALD sample has increased to almost two times that of the Commercial catalyst. This indicates that the TPSR on 20-ALD catalyst results in carbon with more structural defects in the MWCNTs and hence have more sp^3 bonds. And based on previous Raman studies on Carbon Onions show that the I_D to I_G band ratio is usually above 1 [93], [94].

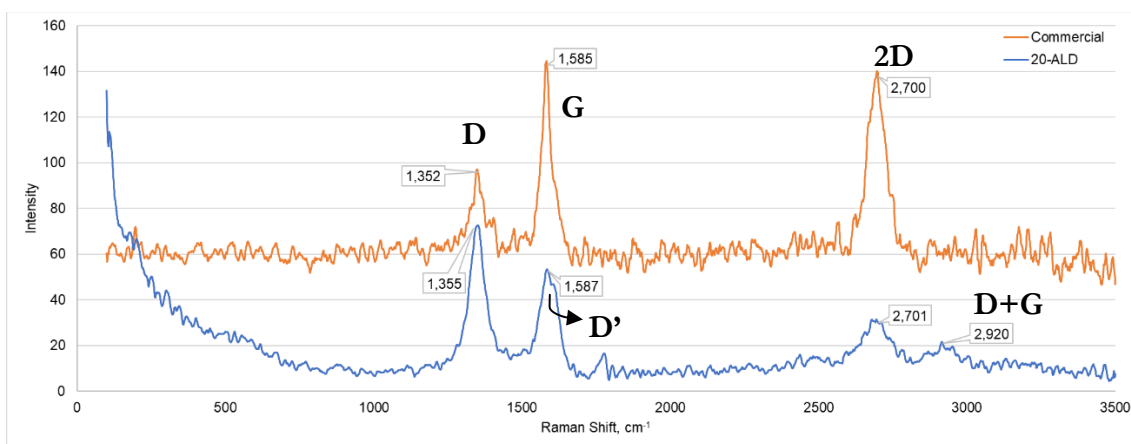


Figure 36 - Raman Shift for spent catalysts - Commercial and 20-ALD

Table 8 - Intensity of Raman bands

| Intensity | D-band | G-band | 2D-band | I_D/I_G | I_{2D}/I_G |
|------------|--------|--------|---------|-----------|--------------|
| Commercial | 95.9 | 144.1 | 139.4 | 0.67 | 0.97 |
| 20-ALD | 71.6 | 52.7 | 30.7 | 1.36 | 0.58 |

Furthermore, the G-band in the 20-ALD sample shows a shoulder peak at around 1620 cm^{-1} denoted as D' peak, which is due to some tangential vibration modes of the impurities/external layers which could not be sandwiched between two layers or could be

associated with functionalization and strain in the C-C bond vibrations [95]. The intensity of the 2D band depends on the number of wall structures in the nanotubes, and the ratio of the I_{2D}/I_G band gives vital information about the number of layers or walls in the carbon nanostructure [96]. It can be seen from Figure 36 that the intensity of the 2D band and the intensity ratio of the I_{2D}/I_G band for the 20-ALD sample has reduced significantly from 0.97 to 0.58 and this confirms multiwall configuration. We also notice the presence of a new band, which is located at around 2900 cm^{-1} . This band is assigned as the combination of D and G, named D+G band [97]. Normally, the intensity of this band increases with the number of disorders in the lattice configuration [98]. The observed Raman characteristics i.e., high I_D/I_G , low I_{2D}/I_G ratio and splitting of G and presence of G+D confirm that compared to the Commercial catalyst sample, the 20-ALD sample exhibits an increase in the number of defects in the lattice structure and an increase in the numbers of walls in the carbon.

It is clear that from the TEM images and Raman Spectroscopy results that the type of carbon is definitely distinct in both the Commercial and 20-ALD catalyst. This shows that despite the motivation for ALD catalysts being protection from sintering and coking, there might be an unexplored avenue of carbon production with unique characteristics over ALD catalysts.

3.2.4. Parameters affecting the TPSR phenomenon

Based on some trial and error experiments that we have performed while investigating the TPSR, we have found that there are some parameters that decide whether the restructuring of alumina happens or not. A non-exhaustive list of parameters that we believe play a role is shown in Table 9. A quick way to detect whether the restructuring as described has taken place or not without imaging the spent catalyst sample is to simply observe the activity during the TPSR experiment. It gives an indication of whether the catalyst is undergoing a transformation or not. Since the 20-ALD catalyst has very low activity compared to uncoated catalysts due to the presence of the large mass transfer limitation, an appreciable increase in activity of the ALD catalyst is an indication that the TPSR restructuring phenomenon suggested here is probably happening.

Of the parameters mentioned in Table 9, the moisture condition of the catalyst before the ALD process seems to be the deciding factor. The same catalyst dried for two hours prior to the deposition process did not show the TPSR result as expected. The 20-ALD catalyst studied in this work was not dried prior to the deposition process. This implies that the moisture content on the Ni active sites prior to the deposition process plays a major role in creating conditions necessary for the subsequent alumina rearrangement.

Since the TPSR process involves crystallization of the ALD alumina, there are other factors related to the crystallization process that can have an impact. Boehmite, which is a hydrated or hydroxyl form of alumina, transforms to γ -alumina between 300 and 450 °C, then to δ -alumina at ~850 °C, θ -alumina at ~1000 °C, and finally α -alumina at ~1125 °C [39]. The alumina crystallization process is also a function of the film thickness, time of annealing, and annealing temperature [99]. Qin et al. [99] investigated the crystallization of alumina thin films on NiAl and found that a crystallization started mainly after 650 °C. For lower temperatures, the time required was longer. Hence, time and temperature are two key parameters that can affect the TPSR outcome. Table 9 provides a starting point to test each of these parameters to optimize the whole system thereby fine-tuning the catalyst characteristics in the desired direction.

Table 9 - Factors affecting TPSR behavior in ALD catalysts (Green: TPSR works, Red: TPSR does not work, Blank: untested)

| Base Catalyst | ALD Process | No. of cycles in ALD | TPSR Gas Medium | TPSR temperature ramp rate | TPSR reactor pressure |
|--|---|----------------------|---|----------------------------|-----------------------|
| Commercial 20% Ni catalyst prepared by | Wet ALD Process (no drying prior to overcoat process) | 20-ALD | CH ₄ -CO ₂ mixture (10% each, 2% Ar, 2% He) | 5 °C/min | Atmospheric Pressure |

| | | | | | |
|--|---|---------------------------|--|---------------------|---------------------------|
| multiple impregnation | | | | | |
| Commercial Ni catalyst – different loading | Dry ALD Process (Dry at 150 °C for two hours prior to overcoat process) | 5-ALD or 10-ALD | He | Any other ramp rate | Higher Operating Pressure |
| Commercial Ni catalyst – different method of preparation | | Higher than 20-ALD cycles | CH ₄ , CO ₂ or any other carbon-containing gas | | |
| Any other catalyst active material and support combination | | | | | |

3.2.5. Effect of TPO after TPSR

Since the TPSR shows that the alumina rearrangement results in better than expected activities for the 20-ALD catalyst, this information can be used to investigate if the process can be used as a pretreatment to catalysts before actual DRM operation. To study this further, the spent catalysts after TPSR were cooled under Helium to room temperature, which was then followed by a Temperature Programmed Oxidation (TPO). The objective is to remove

the carbon deposited on the surface since methane and CO₂ have passed over the catalyst at the coking temperatures of around 500 °C and hence the removal of the coke should enhance the activities of both the Commercial and 20-ALD catalyst. After the TPO, the reactor was again cooled down, a normal reduction was carried out and DRM gas was introduced after the reactor temperature reached 650 °C. The rate of methane consumption, which is a good measure of Ni activity is shown in Figure 37. The 20-ALD catalyst shows a significant increase in activity and is much more stable than the Commercial catalyst which was passed through the same TPSR+TPO. A probable reason for this is that the harsh conditions of the TPSR+TPO caused a lot of sintering so that even after the carbon is removed with a TPO, the activity does not regain the initial activity. To make a fair comparison of the 20-ALD catalyst, the activity is compared with that of a fresh uncoated commercial catalyst without any TPSR. Even here, the Commercial catalyst starts at an activity of about 0.12 mol/min/g_{Ni} but deactivates rapidly within 16 h.

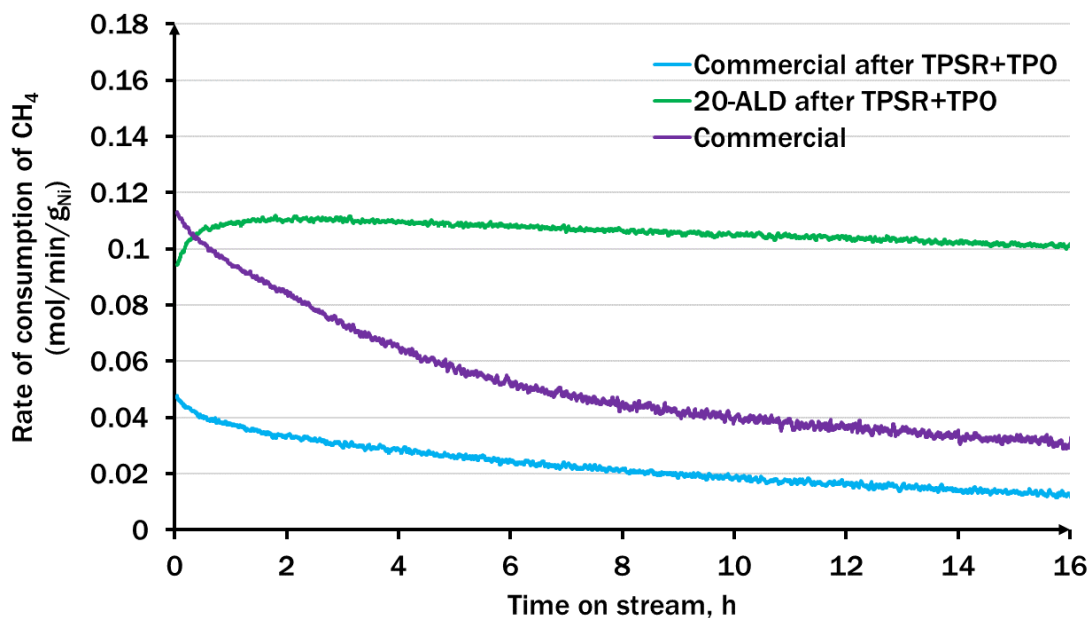


Figure 37 - CH₄ Activity - after TPSR+TPO+Reduction

The H₂/CO ratio of the same run is shown in Figure 38. The 20-ALD catalyst shows a relatively stable H₂/CO ratio between 0.8 and 0.9. However, the other two Commercial

catalysts (with and without TPSR) both rapidly decrease indicating that the DRM activity is reducing. This indicated the TPSR rearrangement of the alumina has probably helped the 20-ALD catalyst to become more resistant to deactivation. The combination of TPO with TPSR seems to help to improve the stability and activity of Ni catalysts.

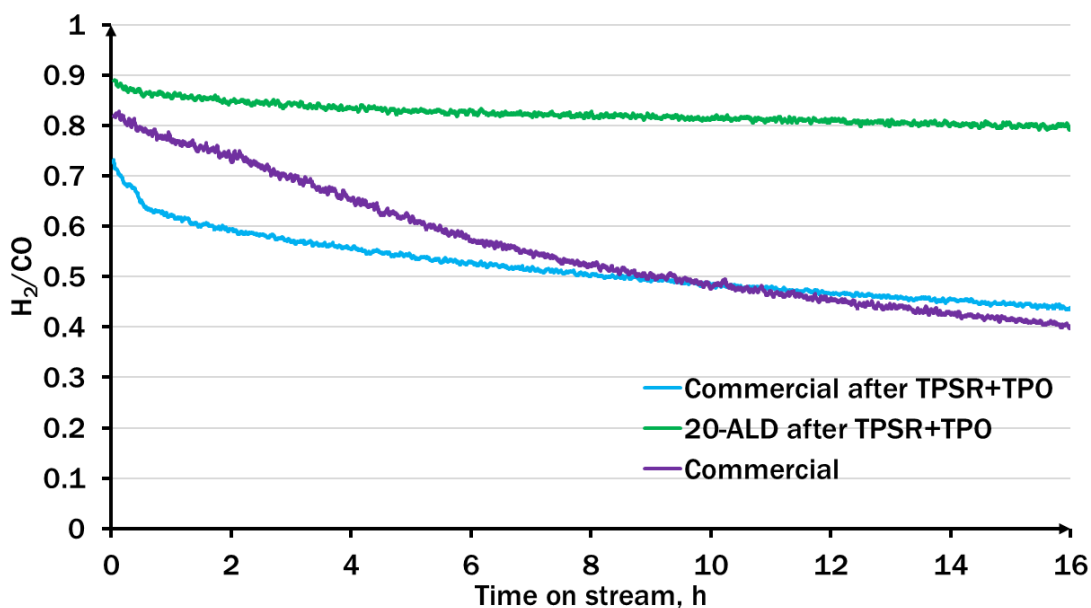


Figure 38 - H₂/CO ratio - after TPSR+TPO+Reduction

As described in Table 9, there are many parameters that impact this behavior and a more detailed investigation in these parameters will help to further improve the catalyst performance.

3.2.6. Conclusions

This work describes a Temperature Programmed Surface Reaction (TPSR) study for Ni catalyst modified by alumina overcoat deposited by the ALD process. By ramping the temperature of the reactor @ 5 °C/min till 800 °C, it was found that the DRM activity over the 20-ALD catalyst shows better activity than the uncoated Commercial catalyst. The TGA experiments show that the amount of coke deposited on the 20-ALD catalyst is much more than that of the uncoated catalyst. The TEM images and Raman spectroscopy indicate that the type of carbon is distinct from that obtained on the uncoated Commercial catalyst, and

we believe it shows close resemblance to the onion-like carbons that are reported in the literature. The workflow followed in this study is illustrated in Figure 39.

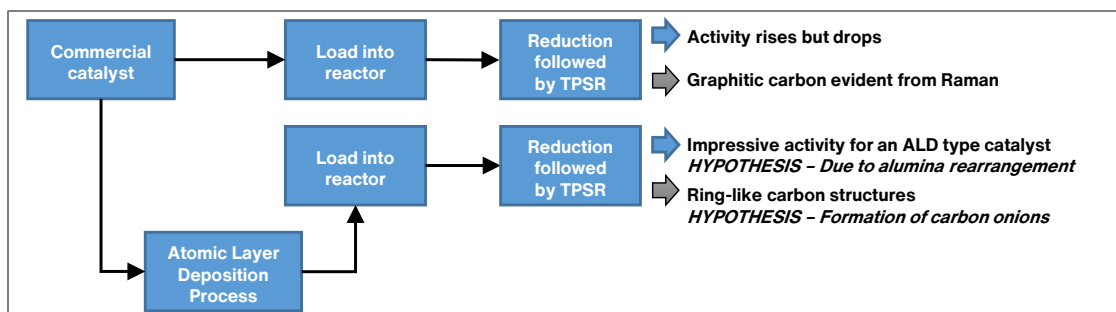


Figure 39 - Workflow in TPSR experiments

As indicated in Table 9, many parameters still need to be investigated for a deeper understanding of the TPSR process on ALD catalysts. Since we have only tested alumina ALD, this opens up a new dimension of surface rearrangement of the overcoat substrate and could be replicated in other systems.

The main objective of using ALD catalysts for DRM was to enhance the catalyst performance and resistance to sintering and coking. Hence, for this application, TPSR can be conceived as an activation protocol to activate the ALD catalyst. After loading the catalyst, TPSR can be performed as a way to enhance the catalyst activity, following it up with an oxidation step to ‘clean’ the surface.

For future work of this study, it is recommended to verify the hypothesis of dispersion increase as the reason for the better activity of the 20-ALD catalyst. A chemisorption experiment done at regular intervals using the protocol described in Chapter 2 could be used for this purpose. Secondly, the probable formation of carbon onions is an interesting finding. Since this particular family of carbon has good applications [100]–[102], it will be interesting to see if the TPSR process can be further modified to maximize the production of this type of high-value carbon.

4. EMISSIONS OF SYNGAS PRODUCTION AND LCA STUDY FOR DRM⁴

Chapters 2 and 3 dealt with the design of catalysts to address the catalyst deactivation problem. However, as noted in chapter 1, catalyst design is not the only challenge in the commercial applicability of DRM. Chapters 4 and 5 will focus on the macro scale of the DRM and its potential for integration in Qatar's natural gas infrastructure. The endotherm for DRM (+247 kJ/mol) is more than that of SMR (+206 kJ/mol) indicating that the reformer duty to process the same amount of natural gas will be more for DRM than SMR. Additionally, as noted in section 1.2, the syngas ratio is different for the competing processes, thereby making a direct comparison unfair. It is naïve to advocate that just because DRM uses CO₂ as a feed, it should be inherently 'greener' than other competing processes. This preposition overlooks the fact that the SMR and DRM produce products of varying quality and the energy required to drive the reaction is different in both. Hence, a systematic approach is necessary to compare different combinations of these processes to truly elucidate if there is an overall reduction of carbon footprint and to look at the operating costs of each of these cases.

4.1. Literature Review

The DRM process has received considerable interest by industry and academia. Ross [103] conducted a survey of DRM related literature and found that more than 1800 papers have been published from 1995 to 2013 on the topic of DRM. As of June 2017, this number stands at 3300+ papers. Most of these papers mention that since DRM utilizes CO₂ as a feed, it must be a solution to reduce CO₂ emissions whilst producing a valuable intermediate, syngas. Justifying this claim has received very little interest compared to the enormous amount of literature on DRM catalysis. There are only a few studies that have considered the impact of DRM on the energy requirement and CO₂ balance of the process, and a short overview of these papers is presented below.

Among the few studies that have addressed the issue of CO₂ balance in the process, Gangadharan et al. [104] compared SMR and SMR+DRM processes through an ASPEN flowsheet simulation to produce syngas (H₂/CO, 3:1) and found that the impact on global warming potential was marginal

⁴ Reproduced with permission from ACS Sustainable Chem. Eng. 2018, 6, 7532–7544 Copyright 2018 American Chemical Society [40]

(~0.5% improvement). Zhang et al. [105] did a similar study but compared SMR with DRM+POX in a combined reformer, and they obtained ~30% reduction in energy costs by the latter case. Since POX is slightly exothermic and DRM is endothermic, co-feeding oxygen and CO₂ seems to have synergistic effects, hence reducing overall energy consumption. Other studies [106]–[108] have simple approaches to estimate the effectiveness of the DRM in reducing CO₂ emissions in syngas production. Some studies have used DRM in parallel with conventional reforming processes while others have studied Combined Reforming (co-feeding all 3 oxidants of steam, oxygen and CO₂). The combined reforming option seems to have more energy advantage than carrying out DRM separately and mixing the product syngas of each process. Roddy [109] listed all factors to be considered while synthesizing syngas networks without specifying any methodology on how it should be done. In a recent study, Martinez-Gomez et al. [110] have optimized the production of syngas from shale gas with economic and safety objectives. Noureldin et al. [111] studied the impact of DRM on CO₂ fixation and more recently, Challiwala et al. [112] considered energy balance around the reformer block for combined reforming case and optimized input flows for the three oxidants (oxygen, steam and CO₂). The system boundaries for both studies was confined to the reformer block and the emissions due to production of oxidants and the upstream emissions of natural gas were not considered. The production of oxidants for conventional reforming (steam and oxygen) are energy intensive processes and must be included in energy assessment studies comparing different reforming technologies.

Secondly, most of the above-mentioned studies consider an almost stoichiometric input flowrates for steam and methane (1:1 to 1.6:1) in the SMR. Industrially, higher steam-to-carbon ratios are maintained to avoid coke formation regime [113]. Experimental results by Yamazaki et al. [114] on commercial reforming catalyst showed that at steam to carbon ratio of 1, the catalyst suffered severe coking and lost its activity in 20 hours. Basini and Piovesan [115] analyzed cost of syngas production at different steam/carbon and oxygen/carbon ratios and concluded that processes at low steam/carbon and oxygen/carbon ratios have significant reductions in syngas production cost of up to 25%. This shows that it is important to account for the steam-to-carbon ratio constraint in such studies, a parameter not accounted in many of the above-mentioned investigations.

In this work [40], the focus is to compare the CO₂ emissions of conventional reforming processes with different reformer networks incorporating a DRM unit in parallel. Additionally, two novel

process concepts are discussed to increase the applicability of DRM over higher syngas ratios. They involve the removal of CO from DRM syngas and addition of H₂ from an external source. All major sources of emissions in each pathway have been quantified and the performance of each case is measured in terms of overall CO₂ emissions and operating costs. An optimization-based approach has been used to find operating points that maximize syngas production and the carbon footprint of these points is calculated. The results point towards the regions of operation and specific scenarios where DRM might have commercial as well as an environmental advantage over conventional processes. The next section lists all the major sources of CO₂ emissions involved in syngas production processes which have been considered in the optimization study.

4.2. Major sources of CO₂ Emissions in Syngas Production – LCA Scope

The EPA defines a greenhouse gas as “any gas that absorbs infrared radiation in the atmosphere” [116]. Carbon dioxide and methane are major greenhouse gases in the syngas production process. The emission of these gases into the atmosphere is one of the major factors responsible for global warming [11]. Both gases have different contributions to global warming and GWP (Global Warming Potential) is used as a metric to combine emissions of different gases. The EPA defines GWP as “a measure of the total energy that a gas absorbs over a particular period of time (usually 100 years), compared to carbon dioxide” [116]. While comparing several competitive processes for syngas production, GWP is chosen as the environmental impact category for computing the carbon dioxide equivalent at each stage of the process. Carbon Dioxide Equivalent is defined as “a metric measure used to compare the emissions from various greenhouse gases based upon their global warming potential (GWP). Carbon dioxide equivalents are commonly expressed as "million metric tons of carbon dioxide equivalents (MMTCO_{2Eq}).” The carbon dioxide equivalent for a gas is derived by multiplying the tons of the gas by the associated GWP” [116].

$$\text{MMTCO}_{2\text{Eq}} = (\text{MMT of the GHG}) \times (\text{GWP of the gas}) \quad (9)$$

Carbon Footprint is used to describe the cumulative effect of greenhouse gases from a person, family, building, organization, or a company [116]. In our research, we have used the term “Carbon Footprint” to describe the cumulative effect of a certain process pathway for syngas production. In

Life Cycle Assessment (LCA) studies, a complete cradle to grave approach is needed to account for all sources of emissions from each stage of a process pathway. In our LCA study, the aim is to track the greenhouse gases over the lifecycle for the chosen syngas production pathways. For that reason, we consider the impact of resource use (methane) and the carbon dioxide generated due to the process pathway chosen. For each pathway, the major CO₂ sources are tracked, and the life cycle stages where no changes are anticipated (such as auxiliary units of power generation) for the pathways are not considered in this study. The Functional Unit is 1 kg of syngas (H₂+CO) at specified H₂:CO molar ratios. The following sections give a detailed description and the assumptions made for the pathways. Figure 40 shows the schematic of all major sources of emissions in the process that have been considered in this study. Details of each case are discussed in later sections.

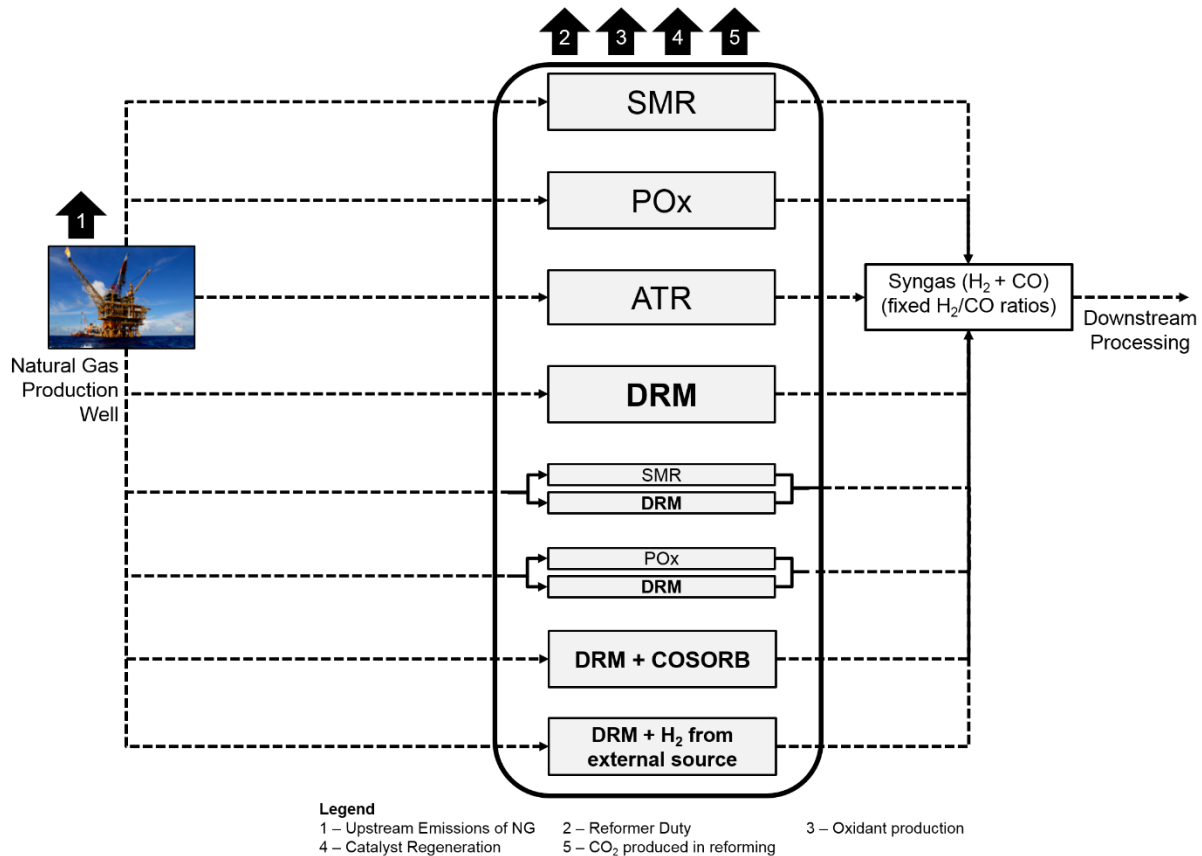


Figure 40 – Schematic showing major sources of emissions considered in the study (Credits are for CO₂ feed in DRM units and hot stream heat integration at reformer outlets)

4.2.1. Upstream emissions of natural gas

Natural gas production at field and its transportation to the plant has its own carbon footprint. GREET (Greenhouse Gases, Regulated Emissions and Energy Use in Transportation Model developed by Argonne National Laboratory) model and software has been used to estimate the upstream emissions from natural gas. Apart from CO₂, the CH₄ and N₂O emissions have to be considered in CO₂ equivalents while calculating total GHG emissions, based on 100-yr GWP (Global Warming Potential) values from IPCC's 2014 Assessment Report [117]. Since CH₄ and N₂O have a 100-yr GWP impact factors of 28 and 265 times respectively when compared to CO₂, the emissions of these gases must be multiplied by these factors. A typical natural gas composition [118] was used with a composition of 95% methane and a molar mass of 16.81 g/mol. Accounting for these in the data from GREET, the upstream emissions are calculated to be about 620.1 g CO₂ emitted per kg of NG delivered at the plant gate, which is about 0.2494 moles of CO₂ emitted per mole of CH₄. There is quite a bit of variation in upstream emissions based on different sources, and this variability mainly arises from the CH₄ leakage in upstream and different methods used to estimate these fugitive emissions. However, the analysis presented here is based on the estimates given above.

4.2.2. Reformer Duty

The reforming reactions are carried out at high temperatures for higher conversions and lower coke formation susceptibility. The reforming reaction of SMR and DRM is endothermic and hence requires heat to be supplied to the system. In the case of POX, the reactant gases are heated to a high temperature of above 1000 °C before being introduced in the reactor. The reformer duty is one of the main energy consumers in the syngas generation unit. An efficiency of 85% has been used in calculations based on industry standards [119]. The carbon dioxide emissions from burning natural gas for energy are considered for the reforming section. Since the reformer outlet gas stream is at high temperature and heats the incoming cold streams, a heat credit is also provided for these syngas streams leaving the reformer based on the approach by Noureldin et al. [111].

4.2.3. Oxidant production

An oxidant is the source of oxygen to produce syngas in reforming. The production of oxidants in each reformer comes with its own greenhouse gas emissions due to energy use and other factors. The CO₂ emissions involved in the production of these oxidants are listed in Table 10.

Table 10 – Carbon footprint for oxidant production. Reprinted from [40]

| Oxidant | Carbon footprint (CO₂ basis) | Notes/Reference |
|-----------------|--|------------------------|
| Steam | 470.8 g/kg steam | GREET® Model |
| Oxygen | 272.9 g/kg O ₂ | GREET® Model |
| CO ₂ | 62.95 g/kg CO ₂ | David and Herzog [120] |

The GREET® Model considers the energy in the generation of steam and production of pure oxygen from the air and reports the associated emissions on the CO_{2c} basis. The carbon footprint for CO₂ reported in the literature is based on CO₂ capture from flue gas (assuming 3% concentration in flue gas based on Natural gas-fired power plant flue gas and capture efficiency of 90%). This is an extremely conservative estimate of the GWP associated with using CO₂ for DRM. If a concentrated CO₂ source is available (for example, CO₂ as a byproduct in the production of ammonia or from midstream acid gas removal section in LNG plants) that can be directly fed to the DRM reactor, this term can be excluded from the calculations.

4.2.4. Catalyst Regeneration

Though equilibrium models based on minimization of Gibbs free energy predict a zero probability of coke formation at high temperatures (>900 °C) and stoichiometric inputs of oxidants and methane, in reality, coke formation can still occur in such conditions[121]. Reformer tubes are usually 10-13 m long and about 100 mm in diameter. In these large tubes, it is quite possible that regions in the tubes might not be at equilibrium due to non-uniform distribution of component flows, channeling, thermal gradients or other effects. Hence, a higher than the stoichiometric ratio of oxidant/methane is used to ensure coke formation is mitigated in industrial reformers.

However, even after all these precautions, there is still a possibility of coke formation due to flow disturbances, etc. When it does occur, the catalyst can be regenerated by burning off the coke. Regeneration can be done on-stream or might need a unit shutdown depending on the severity of coke formation. Catalyst regeneration procedure by burning of coke has been discussed in detail by Rostrup-Nielsen and Lars [121]. Unless mentioned otherwise, catalyst regeneration is accounted for

in our optimization model based on the assumption that each mole of coke formed will be converted to one mole of CO₂ during the coke burning operation ($C + O_2 \rightarrow CO_2$).

4.2.5. Catalyst Preparation

Catalyst preparation on an industrial scale will contribute its own CO₂ emissions to the life cycle emissions of syngas production. In DRM, due to both the input species containing carbon (CH₄ and CO), the coke formation problem is exacerbated and has been studied extensively throughout the literature on DRM. Abdullah et al. [21] present the recent advances in the area of DRM using Ni-based catalysts. Most studies have reported the use of novel catalytic structures, including promoters and bimetallic catalysts to mitigate catalyst deactivation. Amongst the various proposed approaches, one of them is the synthesis of alumina coated nickel nanoparticles[43] prepared by atomic layer deposition technique (ALD).

In this technique, Tri-methyl aluminum (TMA, Al-(CH₃)₃) is used as the overcoat precursor on the catalyst surface. For each mole of aluminum deposited on the catalyst surface, 3 moles of CH₄ are emitted in the ALD deposition process. Due to higher GWP of methane, it becomes important to consider the emissions if frequent catalyst changes are required. In our case, we have assumed the ALD catalyst being replaced every year and the value of this emission source is estimated to be 29.28 μmole CO₂ emitted during catalyst preparation per mole of CH₄ converted. The calculations show that when compared to other sources of emissions (furnace duty, etc.), catalyst preparation contributes less than 0.004% to the total CO₂ emissions and hence this has not been considered in the optimization model. Similarly, for Ni-based catalysts in SMR, CO₂ emissions data from Agarski et al.[122] have been used and the resulting emissions are less than 0.008% of the total SMR emissions. This will not impact the outcome of the optimization model significantly and hence has not been included in the study.

4.2.6. CO₂ production in reforming reactions

Some CO₂ can be produced inside the reformer reactors at reforming conditions, for example, through Boudouard reaction ($2CO \rightarrow CO_2 + C$) and the Water-Gas Shift reaction (WGS, $CO + H_2O \leftrightarrow CO_2 + H_2$). This CO₂ is a penalty for each respective reforming reaction, and this has been considered in the model.

4.3. Optimization Model

4.3.1. Reformer Modeling Equations

The reforming modeling was based on the approach proposed by Nouredin et al. [123] which seeks to minimize the Gibbs free energy of the involved species while accounting for temperature and pressure dependence as well as the possibility of coke formation. Reformer pressure was set at 20 bar in each case. The details of the reforming modeling are shown below. The reformer model is the main part of the overall optimization model. Equations 10-13 are the important equations of the reformer model. The total Gibbs free energy of a system of i^{th} species can be expressed as [124]:

$$G^t = \sum_{i=1}^N n_i \bar{G}_i = \sum_{i=1}^N n_i \mu_i = \sum_{i=1}^N n_i G_i^{\circ} + RT \sum_{i=1}^N n_i \ln \frac{\hat{f}_i}{f_i^{\circ}} \quad (10)$$

where,

G^t → total Gibbs free energy

n_i → number of moles of species i

\bar{G}_i → partial molar Gibbs free energy of species i

μ_i → chemical potential

G_i° → standard Gibbs free energy

R → molar gas constant

T → temperature (K)

\hat{f}_i → fugacity

f_i° → standard state fugacity.

For a reactive ideal gas system, the following assumptions can be made: $G_i^{\circ} = \Delta G_{f_i}^{\circ}$, $\hat{f}_i = y_i \hat{\Phi}_i P$, $f_i^{\circ} = P^{\circ}$ where P is the pressure of the system and P° is 1 bar. Pressure was taken as 20 bar which is a typical operating pressure in industrial reformers [125]. The fugacity coefficients have been calculated based on Peng-Robinson Equation-of-State using TPSI software [126] (Thermodynamic Package Standard Inc. – TPSI Fifteen Fluids). Since all species were not available in the software, some fugacity coefficients were taken from Challiwala et al. [112].

The method of Lagrange's undetermined multipliers is used to find the set of n_i which minimizes G^t for a specified temperature and pressure [124]. Thus, the minimum Gibbs free energy can be expressed as Eq. (11):

$$\sum_{i=1}^N n_i \left(\Delta G_{f_i}^{\circ} + RT \ln \frac{y_i \widehat{\phi}_i P}{P^{\circ}} + \sum_k \lambda_k a_{ik} \right) = 0 \quad (11)$$

where,

$\Delta G_{f_i}^{\circ}$ → standard Gibbs of formation of species i

$\widehat{\phi}_i$ → fugacity coefficient of species i

λ_k → Lagrange multiplier for element k , subject to the mass balance constraints:

$$\sum_i n_i a_{ik} = A_k \quad (12)$$

where,

a_{ik} → number of atoms of the k^{th} element

A_k → total mass of the k^{th} element

For each chemical species, there are N equilibrium equations and w atomic mass balances. This results in a total of $N + w$ equations. There are N unknowns for each n_i of each species i and w Lagrange multipliers λ_k for each element giving a total of $N + w$ unknowns. Hence, there are sufficient number of equations to solve for the unknowns.

The Gibbs free energy minimization method does not require any prior information about chemical reactions. However, the selection of species is very crucial since the addition or omission of important species can lead to erroneous results. This method should only be used for the estimation of product compositions where enough prior practical information is available about the reactive system such as reforming reactions. A high temperature of above 900 °C and well-established catalysts in industrial

reformers ensure that the reaction products are equilibrium limited [125] and do not have any kinetic reaction rate limitations.

Based on the possible products that can form in the reforming reactions, the following chemical species were chosen to model the reforming system: CH_4 (g), CO_2 (g), CO (g), H_2O (g), H_2 (g) and solid carbon modeled as $\text{C}_{(s)}$. To account for the solid carbon in the system Eq. (11) becomes:

$$\sum_{i=1}^{N-1} n_i \left(\Delta G_{f_i}^{\circ} + RT \ln \frac{y_i \varphi_i P}{P^{\circ}} + \sum_k \lambda_k a_{ik} \right) + (n_c \Delta G_{f_{C(s)}}^{\circ}) = 0 \quad (13)$$

4.3.2. Optimization Model Formulation

The objective of the model is to find optimal reformer operating conditions to maximize CO_2 utilization using the DRM process. However, doing so should not result in a reduction of syngas production since it will directly impact plant revenues. To ensure this, an algorithm was developed as shown in Figure 41. The algorithm helps to find optimal solutions that maximize syngas production and minimize overall CO_2 emissions for each reformer case.

Firstly, for a given reformer type, the maximum number of moles of syngas that can be produced at a fixed syngas ratio is determined using stoichiometric targeting method as described by El-Halwagi [127]. This approach determines the target for maximum production of syngas and also the target for the minimum carbon footprint. Because of the conflicting nature of the two objectives, the ϵ -constraint method of multi-objective optimization is used as follows:

Max = Syngas Production

subject to:

- Carbon footprint, $\text{TGHG} \leq \epsilon_n$
 - the value of ϵ_n is iteratively increased starting with the target for minimum carbon footprint
- Carbon footprint equations (Equations 14-16)
 - $\text{TGHG} = \sum (\text{Carbon footprint of the process in moles of } \text{CO}_2 \text{e})_i$
- Reforming modeling equations (explained later)

- H₂:CO ratio (changed iteratively)

The calculation of carbon footprint for each block involves CO₂ emissions associated with the corresponding pathway. The equations used to calculate the CO₂ emissions of individual reformers are listed below.

| | |
|--|------|
| $\begin{aligned} \left(\begin{array}{c} \text{Carbon} \\ \text{footprint} \\ \text{of SMR} \end{array} \right) &= \left(\begin{array}{c} \text{CO}_2\text{e in Reformer} \\ \text{Outlet} \end{array} \right) + \left(\begin{array}{c} \text{CO}_2\text{e of SMR Furnace Duty} \\ \text{supplied by NG} \end{array} \right) + \left(\begin{array}{c} \text{CO}_2\text{e of Upstream emissions} \\ \text{of NG (fuel + feed)} \end{array} \right) \\ &+ \left(\begin{array}{c} \text{CO}_2\text{e due to} \\ \text{steam production} \end{array} \right) + \left(\begin{array}{c} \text{CO}_2\text{e of Catalyst} \\ \text{Regeneration - burning of coke} \end{array} \right) \\ &- \left(\begin{array}{c} \text{CO}_2\text{e credit due to reformer outlet heat integration and} \\ \text{reduction in upstream emissions due to reduced use of NG} \end{array} \right) \end{aligned}$ | (14) |
| $\begin{aligned} \left(\begin{array}{c} \text{Carbon} \\ \text{footprint} \\ \text{of POX} \end{array} \right) &= \left(\begin{array}{c} \text{CO}_2\text{e in Reformer} \\ \text{Outlet} \end{array} \right) + \left(\begin{array}{c} \text{CO}_2\text{e of POX Furnace Duty} \\ \text{supplied by NG} \end{array} \right) + \left(\begin{array}{c} \text{CO}_2\text{e of Upstream emissions} \\ \text{of NG (fuel + feed)} \end{array} \right) \\ &+ \left(\begin{array}{c} \text{CO}_2\text{e due to} \\ \text{oxygen production} \end{array} \right) + \left(\begin{array}{c} \text{CO}_2\text{e of Catalyst} \\ \text{Regeneration - burning of coke} \end{array} \right) \\ &- \left(\begin{array}{c} \text{CO}_2\text{e of credit due to reformer outlet heat integration and} \\ \text{reduction in upstream emissions due to reduced use of NG} \end{array} \right) \end{aligned}$ | (15) |
| $\begin{aligned} \left(\begin{array}{c} \text{Carbon} \\ \text{footprint} \\ \text{of DRM} \end{array} \right) &= \left(\begin{array}{c} \text{CO}_2\text{e in Reformer} \\ \text{Outlet} \end{array} \right) + \left(\begin{array}{c} \text{CO}_2\text{e of DRM Furnace Duty} \\ \text{supplied by NG} \end{array} \right) + \left(\begin{array}{c} \text{CO}_2\text{e of Upstream emissions} \\ \text{of NG (fuel + feed)} \end{array} \right) \\ &+ \left(\begin{array}{c} \text{CO}_2\text{e due to} \\ \text{CO}_2 \text{ capture} \end{array} \right) + \left(\begin{array}{c} \text{CO}_2\text{e of Catalyst} \\ \text{Regeneration - burning of coke} \end{array} \right) \\ &- \left(\begin{array}{c} \text{CO}_2\text{e of credit due to reformer outlet heat integration and} \\ \text{reduction in upstream emissions due to reduced use of NG} \end{array} \right) - \left(\begin{array}{c} \text{CO}_2 \text{ in Reformer} \\ \text{Feed} \end{array} \right) \end{aligned}$ | (16) |

The last term in equation 16 represents the carbon fixation capability of DRM. When the value of this term exceeds the sum of all the other terms, it means the whole syngas generation unit acts a net CO₂ sink. If not, then the process has net CO₂ emissions even after including DRM. The following additional constraints were also applied in the Optimization model:

$$\text{Syngas Ratio} = \frac{\sum_i n_{\text{out},\text{H}_2}}{\sum_i n_{\text{out},\text{CO}}}$$

Individual Reforming Operating Temperature (°C) [113]:

$$\text{SMR: } T \geq 850, T \leq 950$$

$$\text{POX : } T \geq 1300, T \leq 1400$$

$$\text{ATR: } T \geq 950, T \leq 1100$$

Total Methane to each reformer: $\sum n_{in,CH_4} = 1$

Oxygen flow (for ATR and POX): $n_{in,O_2} \geq 0, n_{in,O_2} \leq 2$

CO₂ flow (for DRM): $n_{in,CO_2} \geq 0, n_{in,CO_2} \leq 2$

Steam – to – Carbon (S/C) Ratio = $\frac{n_{in,H_2O}}{n_{in,CH_4} + n_{in,CO_2}}$

For SMR, $n_{in,H_2O} \geq 2, n_{in,H_2O} < 4$

For POX, $n_{in,H_2O} = 0.1 \times n_{in,CH_4}$

For DRM, $n_{in,H_2O} = 0.1 \times (n_{in,CH_4} + n_{in,CO_2})$

Apart from these constraints, other constraints included in each case have been given in respective sections. A fixed amount of steam is included in every reactor to maintain the steam-to-carbon (S/C) ratio based on industrial practice. The S/C ratios have been input as constraints and were adapted from Dybkjaer and Aasberg-Petersen [113].

The proposed optimization formulation was used repeatedly to cover various ratios of H₂:CO. For each ratio, the upper bound on the carbon footprint was increased iteratively starting with the target minimum footprint and increasing the bound until the maximum target for syngas production is achieved. Figure 41 illustrates the implemented flowchart.

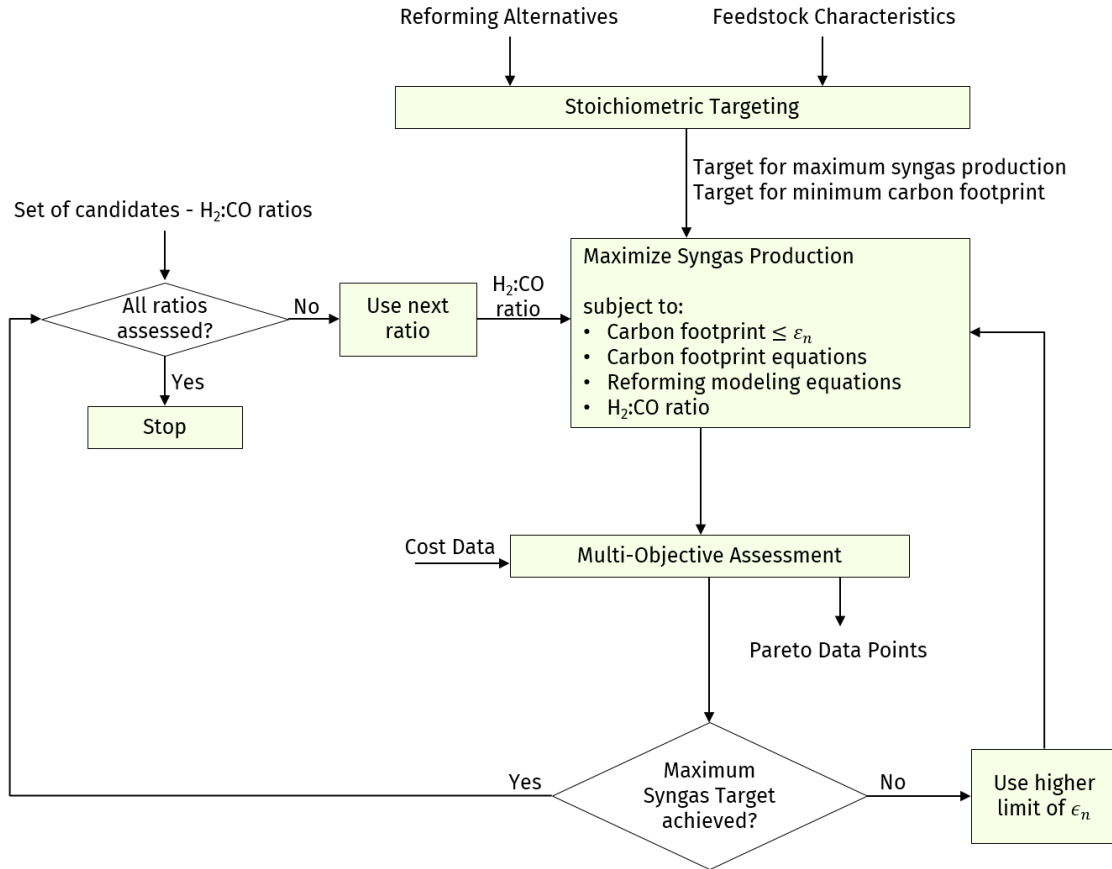


Figure 41 – Solution Approach. Reprinted from [40]

Once the optimization model was formulated, various cases have been studied for different syngas ratios. The LINGO® solution includes all process details such as input flows of oxidant and reformer temperature. All the carbon footprint equations for each reformer case are formulated in the LINGO program and the solution gives a direct result of the overall CO₂ emissions of the optimized reformer network in terms of kg CO₂/kg syngas at specific H₂/CO ratio. The time to reach solution was in the range of 1-10 minutes on an Intel i7 core machine of 3.4 GHz processor speed with 8 GB RAM.

To effectively compare the performance of DRM, whether as a stand-alone reformer or in combination with other existing reforming technologies, several cases have been considered in this study, and the details are listed in Table 11.

Table 11 – Cases considered for study. Reprinted from [40]

| Reforming Technology | | Case No. | S/C ratio constraint[113] | Oxidants |
|---|---|----------|-----------------------------|-----------------------------------|
| Conventional Reforming Technologies | SMR | 1 | 2-4 | Steam |
| | POX | 2 | 0.1 | Oxygen and Steam |
| | ATR | 3 | 0.6-0.9 | Oxygen and Steam |
| Dry Reforming of Methane | DRM | 4 | 0.1 | Steam and CO ₂ |
| Parallel Combinations | POX + DRM in parallel | 5a | 0.1 for each | Oxygen, Steam and CO ₂ |
| | SMR + DRM in parallel | 5b | 2-4 for SMR and 0.1 for DRM | Oxygen, Steam and CO ₂ |
| DRM + COSORB | Captured CO used as Reformer fuel | 6a | 0.1 for DRM | Steam and CO ₂ |
| | Captured CO sold as feedstock | 6b | 0.1 for DRM | Steam and CO ₂ |
| DRM + H₂ from external source | DRM Syngas combined with H ₂ from an external source | 7 | 0.1 for DRM | Steam and CO ₂ |

Case Nos. 1, 2, and 3 are the industry benchmarks and are established commercial processes. Any new proposed process should have a significant improvement over these processes in terms of CO₂ emissions or operating costs, to be considered for commercialization.

Case 4 refers to the DRM case. Cases 5a and 5b are combinations of DRM with other conventional processes (POX and SMR, respectively) in parallel as shown in parallel reformers in Figure 42.

Cases 6a, 6b, and 7 are novel combinations considered with the aim of increasing the DRM syngas ratio. Case 6 consists of a DRM unit operating at industrial reforming conditions (similar to 4)

followed by a COSORB (CO Sorption) unit to capture CO from the DRM syngas. This will help in enhancing the syngas ratio of DRM syngas. But since the COSORB unit has its own CO₂ emissions and operating costs, it is important to quantify the benefit for various operating conditions. Two separate cases are considered – one where the captured CO is used as a fuel in the DRM Reformer furnace and case 6b referring to the use of the captured CO as feedstock in an external plant. In case 7, supplemental H₂ is used from an external source (e.g., an Ethylene plant) to increase the syngas ratio of DRM syngas. To the best of our knowledge, these two scenarios (Cases 6 and 7) have not been studied in the literature in combination with DRM for syngas production.

The Optimization Model solution gives the operating conditions of the reformer to attain the desired objectives. Figure 42 shows the optimization variables for a single reformer and the parallel reformers cases. The results of the LINGO® optimization are discussed in the next section.

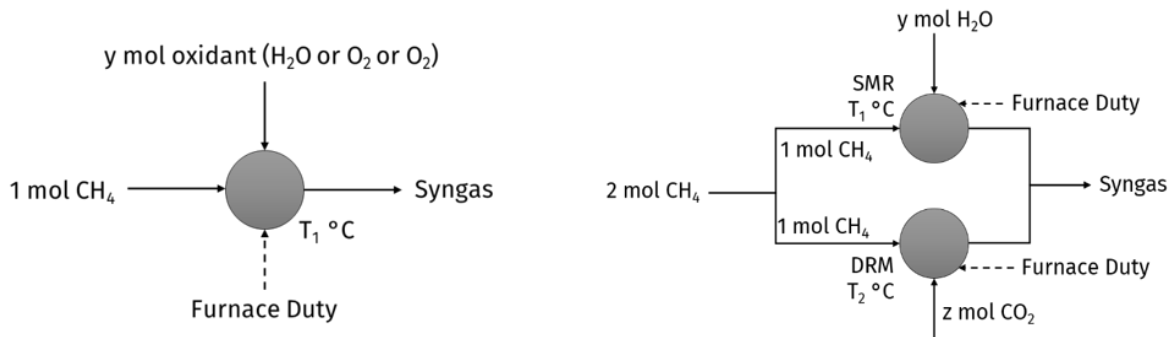


Figure 42 – Optimization variables in single reformer (Cases 1-4) and parallel reformers (Cases 5a, 5b). Reprinted from [40]

4.3.3. Comparing cost of syngas production

The relative cost of syngas production by different processes has been calculated based on the feedstock costs as shown in Table 12.

Table 12 – Feedstock Costs. Reprinted from [40]

| Raw Material/Utility | Unit Cost | Notes/Reference |
|-----------------------------|------------------|---|
| Methane | \$2.8/MMBtu | US Energy Information Administration (EIA) Data [128] for October, 2017 |
| Steam (20 bar) | \$7/tonne | TLV Steam Unit Cost Calculator[129] |
| Oxygen | \$35/tonne | Vora et al.[130] |

Assuming that CO₂ is sourced from a source which needs no further treatment, CO₂ is assumed to be available without any cost. Examples of such streams are the CO₂ streams in the natural gas processing plants where the captured CO₂, which is of high quality is usually released into the atmosphere. The operating cost for each reformer case is based on the feedstock costs of natural gas and oxidants, fuel costs for the furnace duties, and cost savings due to heat integration. In the special case of DRM+COSORB, the cost of COSORB unit operation, and the profit from selling CO to an external customer was also considered (where applicable). It should be noted that cost comparisons of different technologies should be only done at the same syngas ratios.

4.4. Results

The results from the optimization model are discussed in this section. The environmental metric to compare different reforming processes is the overall carbon footprint (kg CO₂/kg syngas produced) for specific syngas ratios and the operating cost is compared based on \$/kmol of syngas. Results for each case as outlined in Table 11 are discussed in separate sub-sections.

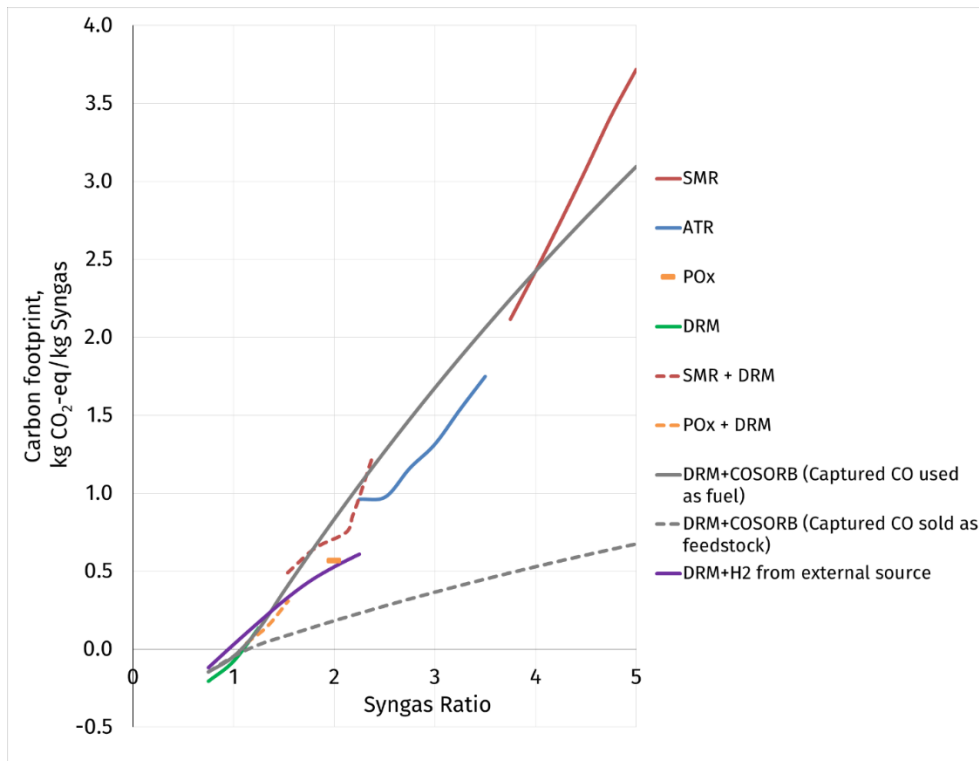


Figure 43 – Carbon footprint of syngas production for various processes. Reprinted from

[40]

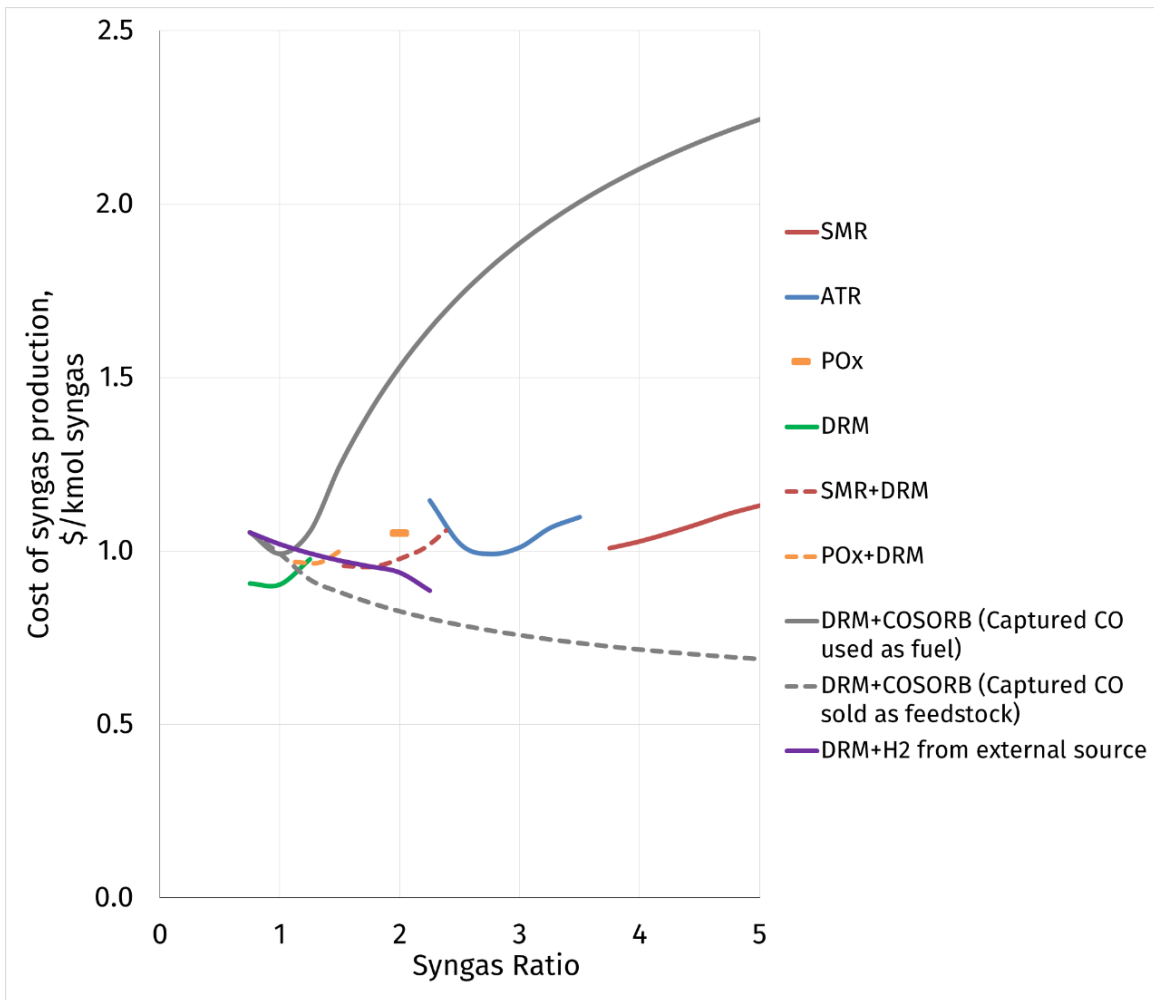


Figure 44 – Cost of syngas production by various processes. Reprinted from [40]

4.4.1. Conventional Reforming Technologies

For SMR, the steam-to-carbon ratio is set to a minimum of 2 and at this ratio and between operating temperature of 850 °C and 950 °C, syngas produced has a H₂/CO ratio of about 3.75. Any additional steam introduced will result in syngas with higher H₂/CO ratios. Typical industrial steam reformers operate at these high steam-to-carbon ratios primarily to prevent coke formation and also in some cases to maintain a higher partial pressure of H₂ in downstream synthesis. E.g., some methanol plants operate at a higher than required H₂ in the methanol synthesis loop[131]. As shown in Figure 43, SMR is the only available technology to produce high H₂/CO ratio syngas. Oxygen or CO₂ does not help to meet the stoichiometric requirements and hence SMR is the only option. As evident from Figure

43, SMR has a significantly high carbon footprint due to the excess steam required based on the S/C constraint set for SMR.

In Partial Oxidation, where pure oxygen is the only oxidant used, based on equilibrium calculations, the syngas produced has a H_2/CO ratio of about 1.8. Since a constraint of S/C ratio of 0.1 was added as per industrial conditions, the syngas produced here has a slightly higher syngas ratio closer to 2.

In Auto-thermal Reformer (ATR), an S/C of 0.6 to 0.9 is allowed and hence ATR is able to produce syngas of higher H_2/CO ratios than POX. Due to the subsequent addition of steam at increasing syngas ratio which moves it from slightly exothermic range (POX) to a highly endothermic region (SMR), we see a sharp increase in the overall carbon footprint due to increasing furnace duties.

These results will be the benchmark and all new reforming options will be compared to these carbon footprints at different syngas ratios to quantify the benefit of newer proposed solutions.

The operating cost of SMR, ATR, and POX at different syngas ratios is shown in Figure 44. The operating cost for SMR shows an increase due to the increased use of steam and reformer duties to produce higher syngas ratios. The ATR has an option between oxygen and steam. As the syngas ratio increases beyond 2.25, oxygen contribution decreases, and steam contribution increases. The ATR operating cost shows a decreasing trend due to oxidant cost (steam is cheaper than oxygen) and the increasing trend is due to increasing energy costs (moving from exothermic POX to endothermic SMR).

4.4.2. Dry Reforming of Methane

A DRM unit operating as a stand-alone unit will only be able to produce low syngas ratios due to stoichiometric limitations. Figure 43 shows the carbon footprint of syngas produced by DRM for the syngas ratio from 0.75 to 1.25. Syngas with H_2/CO ratio of 1.25 is made possible due to some steam used to maintain the S/C ratio of 0.1 and when some methane is converted to coke releasing the hydrogen. This coke is later removed by burning during the catalyst regeneration process. As indicated in Figure 43, it is possible for DRM to operate in the negative region of the y-axis, (indicating that the DRM unit acts as a net CO_2 sink) albeit at low syngas ratios (1 and less than 1).

Though the Optimization model can choose temperatures between 700 °C to 1100 °C, it invariably selects the highest temperature (1100 °C) to maximize the syngas production. Intuitively, many studies on DRM claim that lowering the operating temperature could reduce overall CO₂ emissions. However, since conversions are limited at low temperatures, carbon footprint per mole of syngas produced increases. Detailed analysis of DRM at low temperatures is shown in section 5.4, which proves that a high temperature in the DRM reactor reduces the overall carbon footprint per kg of syngas produced.

Since the DRM is limited by the syngas ratio it can operate in, parallel combinations of SMR+DRM and POX+DRM are considered to investigate if such a combination would have benefit in terms of reduction in overall CO₂ emissions.

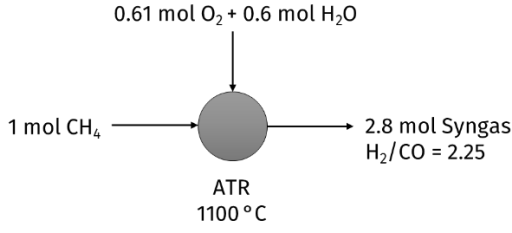
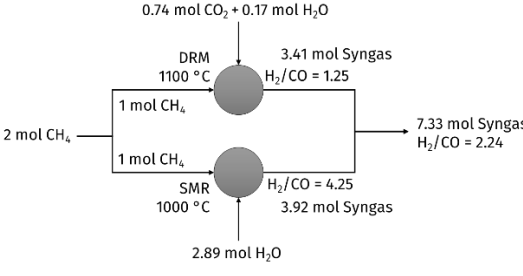
4.4.3. Parallel Combinations

Parallel reforming cases have been studied where an equally sized DRM unit is placed parallel to existing SMR and POX unit. Each model solution of DRM was paired with every model solution of SMR and POX. Since all existing points were found by maximizing syngas production, among all available points, the points of lowest carbon footprint were selected and plotted as shown in Figure 43 and the operating cost comparison is shown in Figure 44.

As is evident from the comparison of carbon footprints in Figure 43, the parallel combination has no benefit in terms of reduction of overall CO₂ emissions. However, in some operating regions of syngas ratios, there is an economic benefit in using the parallel combination.

For syngas ratio of 2.25, the SMR+DRM in parallel configuration is cheaper (~11%) than an ATR but has same CO₂ emissions as shown in Table 13. The reason being that the SMR unit has a minimum S/C ratio of 2 which in turn increases the emissions of that unit, diminishing the benefit of the DRM reformer working in parallel.

Table 13 – Comparison of Model solutions for syngas ratio = 2.25. Reprinted from [40]

| Process network to minimize overall carbon footprint | CO ₂ e Carbon footprint* (kg CO ₂ /kg Syngas, H ₂ /CO = 2.25) | Cost of Production (\$/kmol syngas) |
|---|--|--|
|  | 0.96 | 1.15 |
|  | 0.96 | 1.02 |

Similarly, for syngas ratio of 1.5, a POX+DRM parallel combination will have about 58% lesser CO₂ emissions than a SMR+DRM parallel combination but will be slightly more expensive (~5%). Details of the solution of the Optimization Model are shown in Table 14.

This comparison study illustrates the significance of using an optimization-based approach to study reforming network configurations which have many interlinked parameters built in their models. However, all these combinations produce net CO₂ even after incorporating an equally sized DRM reformer in parallel.

Table 14 – Comparison of Model solutions for syngas ratio = 1.5. Reprinted from [40]

| Process network to minimize overall carbon footprint | CO ₂ e Carbon footprint* (kg CO ₂ /kg Syngas, H ₂ /CO = 1.54) | Cost of Production (\$/kmol syngas) |
|--|--|--|
| | 0.31 | 1.01 |
| | 0.49 | 0.96 |

*Over the system boundary, CO₂ fixation occurs if this value is negative, CO₂ is emitted if this value is positive

4.5. Conclusion

This chapter describes the optimization model and the LCA approach used to assess different syngas production pathways. From the results, it is evident that parallel reformer combinations of DRM with existing conventional reformers do not have an appreciable reduction in both the CO₂ emissions or cost incentive over existing processes. Yet, the very low carbon footprint of the pure DRM process appears to have potential, and hence a different approach than parallel combinations has been used. While designing any process pathway, the objective is to enhance the syngas ratio while still leveraging the CO₂ utilization capability of DRM. Two process synthesis concepts are explored in the next chapter. The first process, called DRM+COSORB involves removing the CO from DRM syngas, thereby producing two streams – one with a high H₂/CO ratio and another with pure CO. The second process involves supplementing a stand-alone DRM syngas with an external hydrogen source. Both these proposed processes and their potential is described in further detail in Chapter 5.

5. NOVEL TECHNOLOGIES FOR DRM PROCESSES

This chapter describes the potential of two process pathways involving DRM for the production of syngas with high H_2/CO ratio. As described in the previous chapter, since the parallel combinations of DRM with commercially available processes do not result in a reduction in carbon footprint, the processes studied here will avoid the use of any currently available syngas production pathways. Instead, the focus will be to use different approaches to boost the H_2/CO ratio of the DRM syngas.

5.1. DRM + COSORB

DRM can achieve a near-zero carbon footprint as shown in Figure 43, but this happens only at low syngas ratios of around 1. To work around the bottleneck of the syngas ratio, CO removal from syngas produced by DRM has been studied as an option to boost $H_2:CO$ ratio of DRM syngas. To employ this, an industrially tested process called COSORB has been used. COSORB has been extensively studied [132]–[134] and commercial plants are in operation [135]. COSORB is a typical absorption/desorption process with a toluene-based solvent containing $CuAlCl_4$, which is shown in Figure 45 [136]. This process has many benefits over other separation processes such as cryogenic separation or copper liquor process [137].

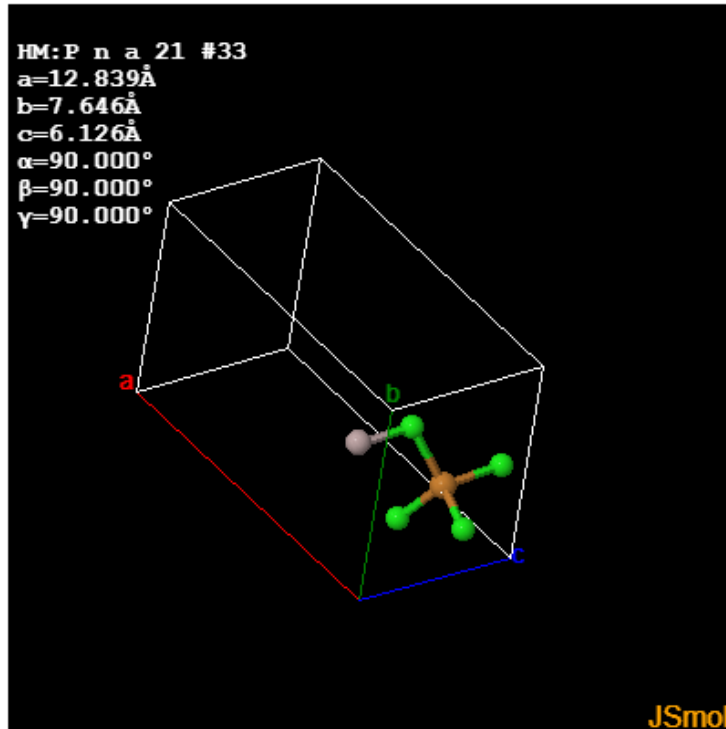


Figure 45 - CuAlCl_4 molecule [136]

Figure 46 shows the proposed process concept wherein the DRM syngas is sent to the COSORB unit to capture CO. Since the product syngas still needs some CO, the COSORB unit can be operated below its maximum separation efficiency thereby reducing energy consumption and allowing just enough CO to remain in the syngas stream. Two cases have been considered based on the destination of the captured CO. It can either be used as a furnace fuel [138] in the DRM reformer or as a fresh CO feedstock for any other downstream petrochemical application, as shown in Figure 46.

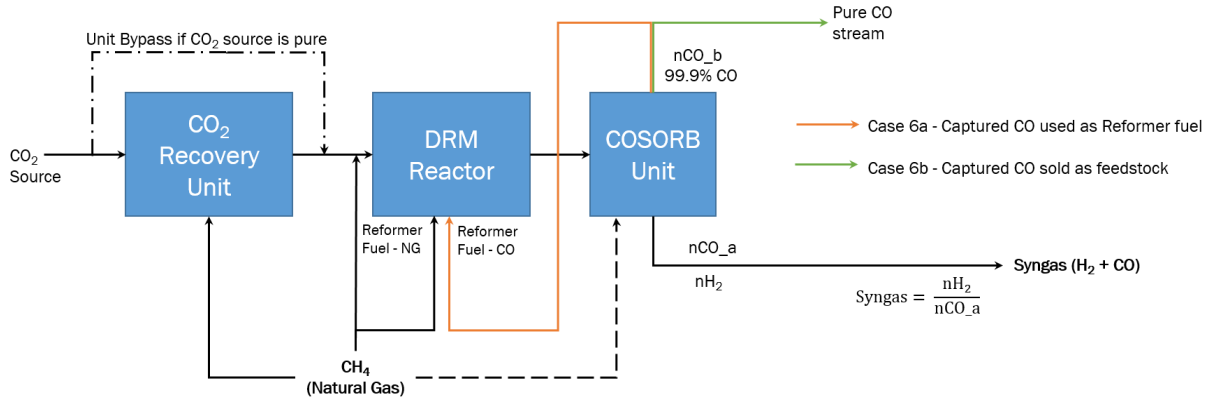


Figure 46 – Proposed DRM+COSORB Process. Reprinted from [40]

The carbon footprint comparison results and operating costs are shown in Figure 43 and Figure 44 respectively. If the captured CO is used as a fuel, the overall carbon footprint exceeds conventional reformers up to a syngas ratio of 4. This can be attributed to the lower calorific value of CO which is 282.8 kJ/mol whereas, for methane from natural gas, the calorific value is 890.8 J/mol. And combustion of both methane and CO yields CO₂ which is a penalty. However, when CO is not used as a fuel and all fuel requirements are met by natural gas alone, the carbon footprint is considerably lesser than conventional reformers at all high syngas ratios.

Comparing the operating cost for both the processes, the cost of operating DRM+COSORB when CO is used as a fuel is much higher than conventional processes. Assuming a sale price of \$75/tonne for the captured CO [123], the operating cost is significantly lesser than that of existing processes as shown in Figure 44.

This shows that the second case in which CO is sold to an external plant has a reduction in terms of CO₂ emissions as well as significant cost benefit when compared to existing processes at high syngas ratios of 2 and 3. This comparison is shown in Figure 47.

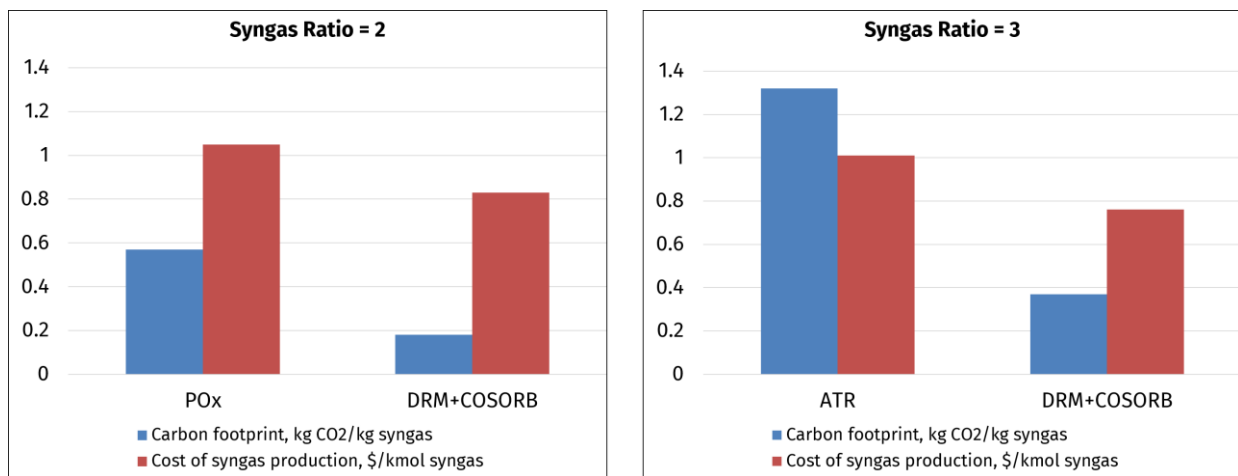


Figure 47 - Comparison of POX/ATR and DRM+COSORB (Captured CO sold as feedstock case) for syngas ratio of 2 and 3. Reprinted from [40]

This shows that the proposed process concept of DRM+COSORB when the captured CO is sold to an external plant has great potential in terms of reduction in CO₂ emissions as well as being competitive in terms of operating costs for syngas production at high syngas ratios. The challenge for this process is finding a suitable customer who can utilize the captured CO as feedstock. A patent application has been filed for the DRM+COSORB process and it is shown in Appendix C.

5.2. DRM + H₂ from external source

The other approach is to supplement the DRM syngas with external hydrogen available elsewhere. Any viable source of hydrogen can be considered but, in this study, we have considered ethylene plant as the hydrogen source. In a typical ethylene plant, the hydrogen obtained after dehydrogenation of ethane is usually used as fuel in the furnaces [139] as shown in Figure 48. Though it is not a preferred fuel due to its low heating value [140], a typical ethylene plant does not usually have a hydrogen sink like a hydrocracker in an oil refinery. This presents an opportunity for mass integration with a DRM unit wherein the hydrogen can be blended with DRM to produce syngas of higher H₂:CO ratio and the hydrogen fuel can be substituted by methane in natural gas. Figure 48 shows this mass integration concept.

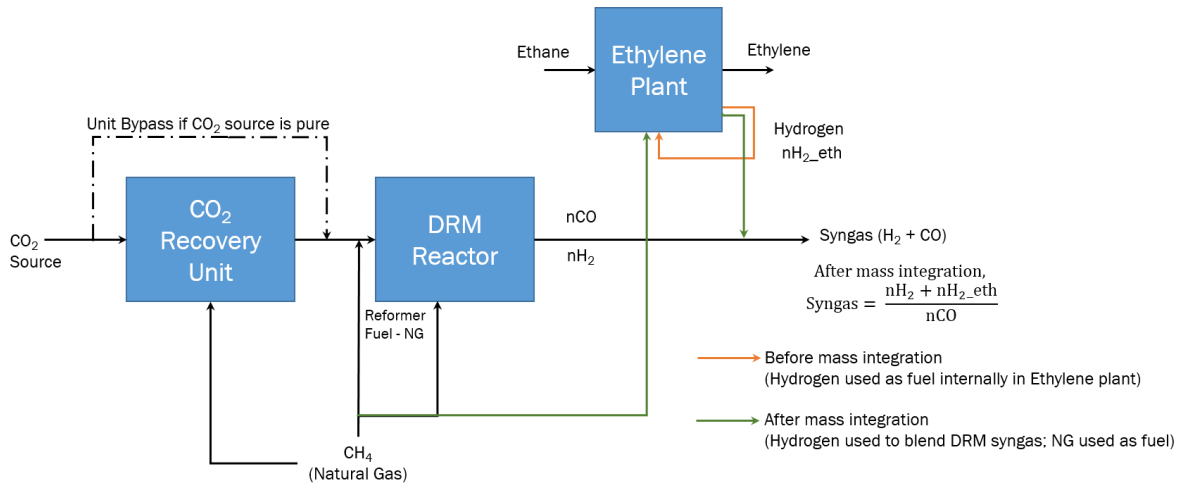


Figure 48 - DRM and Ethylene Plants before and after mass integration. Reprinted from [40]

The number of hydrogen moles available per mole of methane fed to the DRM Reformer was limited to a maximum of 2. The mass integration should consider that the size of both units will be interlinked and hence the DRM capacity will be limited by the amount of hydrogen available from the Ethylene plant.

The hydrogen fuel on combustion does not yield CO₂ and hence the CO₂ generated due to methane combustion must be included in the carbon footprint of the syngas production unit. Additionally, the upstream emissions for natural gas fuel should also be included. The amount of methane needed can be calculated by equating the energy duty that was initially supplied by hydrogen (Calorific Value of Hydrogen is 284 kJ/mol), as shown in Equation 17.

$$n_{\text{CH}_4} = \frac{284 \times n_{\text{H}_2}}{890.8} \quad (17)$$

The carbon footprint results and operating costs comparison are shown in Figure 43 and Figure 44 respectively. The results indicate reductions in both, the CO₂ emissions and operating costs. For syngas ratio of 2, there is a slight reduction of 7% in the overall CO₂ emissions and 11% reduction in operating costs over a POX unit. This proves that in cases where a sufficiently large hydrogen stream

is available, it is cheaper and more environmentally friendly to substitute the hydrogen fuel with natural gas and use the hydrogen to boost syngas ratio of DRM syngas.

5.3. Potential for integration of DRM+COSORB process in an industrial city

The analysis presented in section 5.1 shows that DRM can be combined with a CO separation process after the reformer to produce syngas with reduced carbon footprint and operating costs when compared to commercial benchmark processes. This sub-section provides an overview of the potential of DRM in process pathways requiring varying H_2/CO ratios. A schematic of the processes considered is shown in Figure 49 and they are described in further detail in further sub-sections.

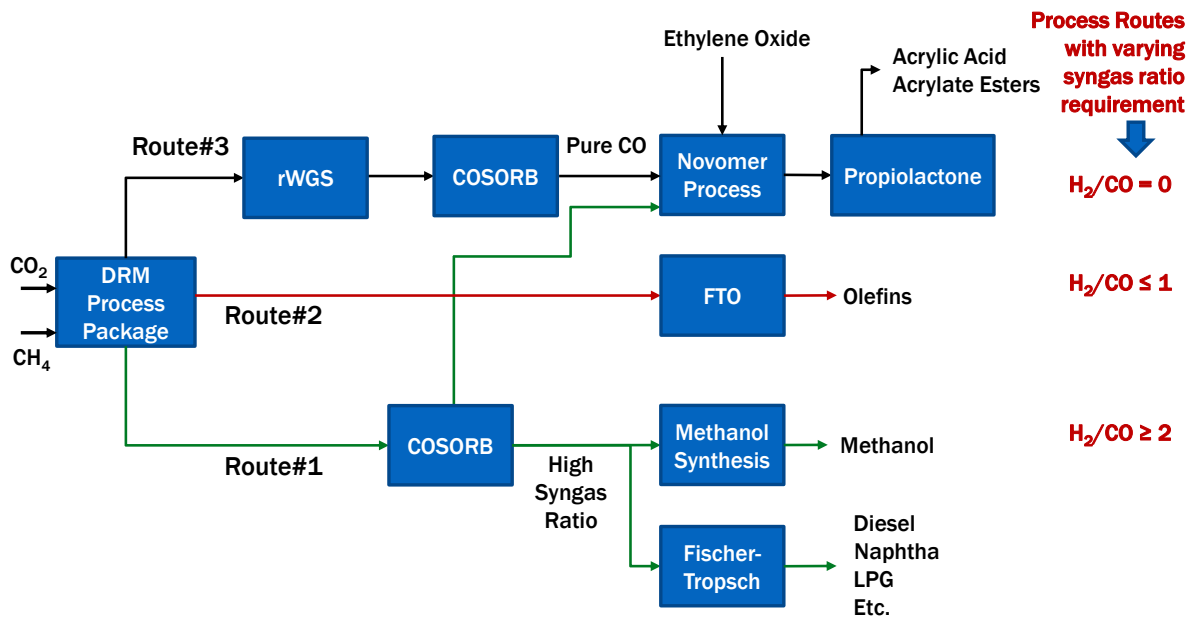


Figure 49 - DRM Process utilized for different pathways based on H_2/CO requirement

5.3.1. Processes requiring H_2/CO ratio ~ 2

As described in section 5.1, to produce a syngas with H_2/CO of 2 and above, a COSORB unit to separate the CO will enhance the syngas ratio of DRM thereby making it suitable for processes like methanol synthesis and Fischer-Tropsch.

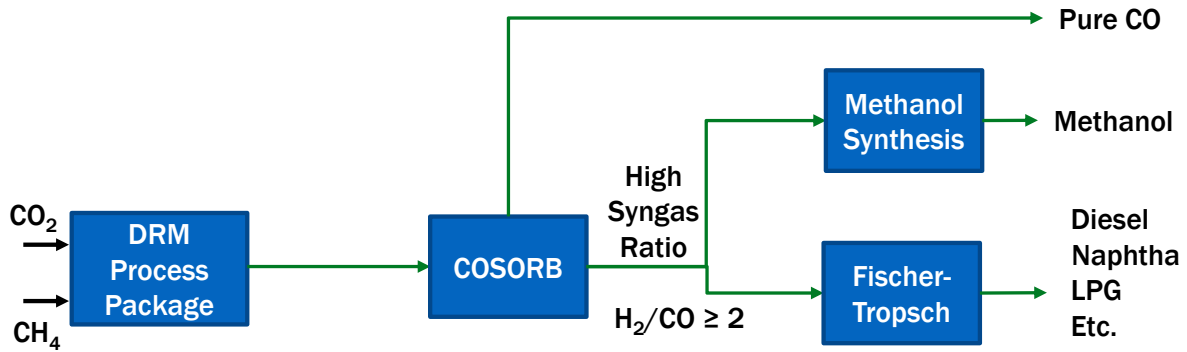


Figure 50 - DRM for $H_2/CO=2$

It should be noted that for this combination to be competitive with existing processes, the CO_2 source should be pure enough to warrant no further purification cost. Even a small cost of \$25/tonne can make the operating costs of this process equal to that of other processes like POX. From the stoichiometry of the DRM reaction, we can estimate the amount of pure CO_2 needed and the size of the CO capture plant required to produce the high H_2/CO ratio from the DRM+COSORB process. Two GTL plant sizes are shown and as is evident from Table 15, the CO capture plants are quite large and presumably the CAPEX associated with these plants will be high. Additionally, the amount of CO_2 needed is about 19,000 t/d for a 32,000 bbl/d GTL plant. An additional constraint is that this stream should be a pure stream, further constraining the number of streams that can be used for DRM. LNG plants where the acid gas removal in mid-stream processes produce a large CO_2 concentrated stream will be highly desirable as a candidate for DRM CO_2 source.

Table 15 - Estimation of the COSORB plant capacity

| GTL plant capacity (bbl/d) | Approximate NG used, MSCF/d | Pure CO_2 needed, t/d | Avoids the use of Oxygen, t/d | CO Capture Capacity, t/d |
|----------------------------|-----------------------------|-------------------------|-------------------------------|----------------------------|
| 32,000 | 320 | 19,152 | 7,000 | 12,178 |
| 128,000 | 1,280 | 76,606 | 28,000 | 48,711 |

5.3.2. Processes requiring H_2/CO ratio ~ 1

The COSORB unit, as described in the previous section will be quite large as the whole syngas stream will have to be passed through the COSORB unit for the CO separation. Multiple parallel trains may be anticipated as the single train capacities might exceed the requirement of a normal-sized GTL plant.

If it is desirable to use the DRM syngas with a low H_2/CO ratio directly as a feedstock, then Fischer-Tropsch to Olefins (FTO) is a promising pathway. Figure 51 shows the Olefin-to-Paraffin molar ratios as a function of different H_2/CO ratios from a previous experimental campaign [141]. As H_2/CO ratios decrease, the O/P ratio increases. In the absence of a hydrogen-rich atmosphere, double bonds are invariably formed between carbon atoms. Though the olefins are undesirable in the typical Fischer-Tropsch, the process makes economic sense if the objective is to utilize a low H_2/CO ratio syngas. Galvis and de Jong [142] presented a review of catalysts in literature for the production of lower olefins from syngas. Catalysts like Fe-Na-S/CNF and Fe-Mn/MgO have a CO conversion of about 80% and C_2 - C_4 olefin selectivity of about 50%. Since olefins are valuable products, this route is a promising pathway to utilize the DRM syngas without any syngas ratio adjustment step.

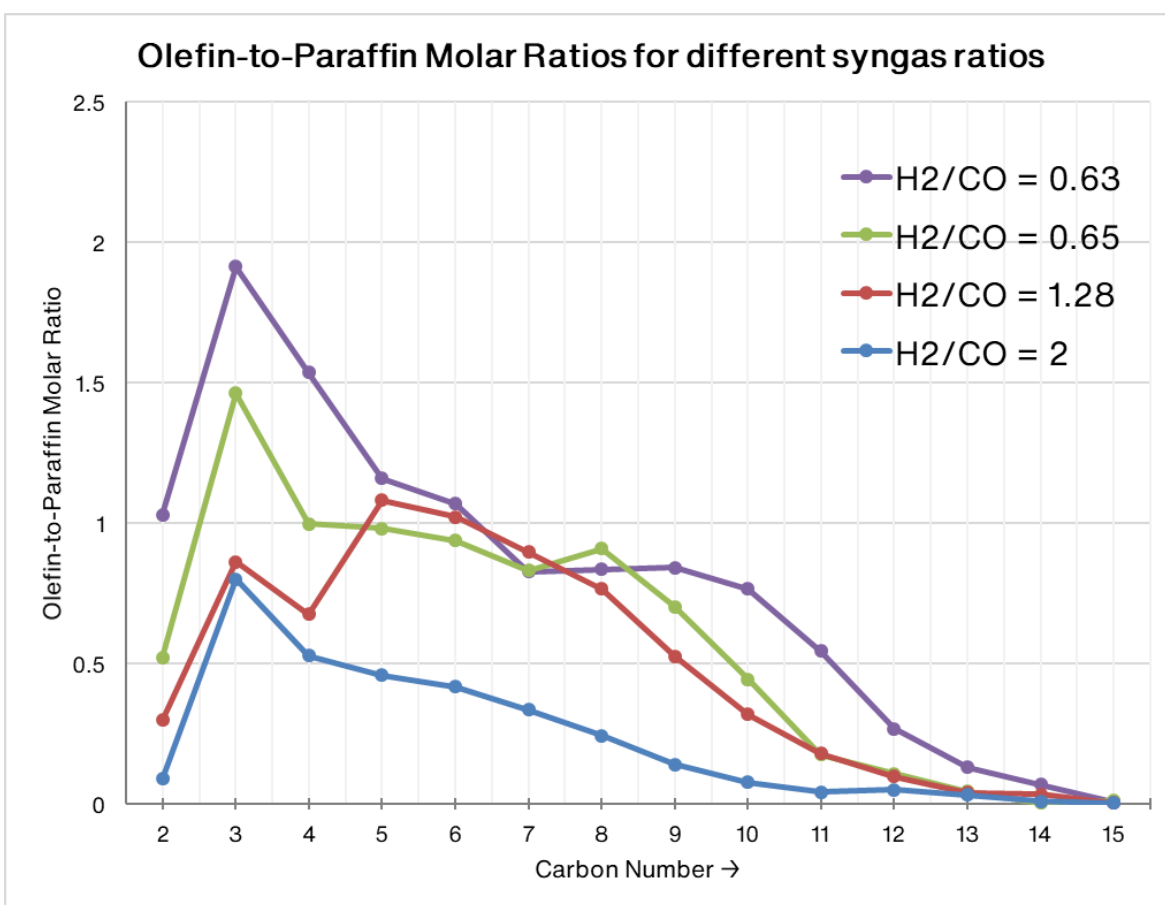


Figure 51 - O/P ratios for different H_2/CO ratio syngas. Reprinted from [141]

El-Halwagi [143] discusses a metric, called MISR to quickly predict the economic potential of process pathways without the need for time-consuming detailed techno-economic assessments. MISR stands for Metric for Inspecting Sales and Reactants and is defined as follows:

$$MISR = \frac{\sum_{p=1}^{N_{products}} (\text{Annual production rate of product } p \times \text{Selling price of product } p)}{\sum_{r=1}^{N_{reactants}} (\text{Annual feed rate of reactant } r \times \text{Purchased price of reactant } r)}$$

MISR > 1: Process may be considered for detailed analysis, higher values of MISR desirable

MISR ≤ 1: Process is not economically viable

A high MISR value indicates good economic potential but further analysis is required. An MISR of 1 and low can be discarded from further study as no matter how efficient a process is, it might not be economically feasible.

Based on the stoichiometry of the FTO reactions, MISR is calculated for FTO processes, and the prices used for reactants and products are shown in Table 16.

Table 16 - Prices considered for MISR calculation

| Reactant/Product | Feedstock Cost/Selling Price | |
|------------------|------------------------------|----------|
| CH ₄ | 167 | \$/tonne |
| CO ₂ | 50 | \$/tonne |
| C ₂ = | 1500 | \$/tonne |
| C ₃ = | 882 | \$/tonne |
| C ₄ = | 1000 | \$/tonne |

For all the C₂ to C₄ olefins, MISR lies between 5 and 9 as shown in Table 17, which indicates that this is a promising pathway and this should be shortlisted for further assessment.

Table 17 - MISR Estimation for C₂-C₄ Olefins

| Olefin | CH ₄ needed, tonnes | CO ₂ needed, tonnes | Olefin produced, tonnes | MISR |
|------------------|--------------------------------|--------------------------------|-------------------------|------|
| C ₂ = | 16 | 44 | 28 | 8.6 |
| C ₃ = | 24 | 66 | 42 | 5.1 |
| C ₄ = | 32 | 88 | 56 | 5.7 |

5.3.3. Processes requiring H₂/CO ratio ~ 0

An H₂/CO ratio of 1 indicates that H₂ content is zero and it is desired to maximize the CO content. A carbonylation process by a company, Novomer, uses CO to convert a C₂ feedstock, ethylene oxide to a C₃ feedstock, propiolactone, as shown in Figure 52. Propiolactone is a cyclic compound that can be easily converted to other high-value products like acrylic acid at low to moderate temperatures. The CO from the DRM process can now be studied as the source of the CO instead of other commercial syngas generation processes.

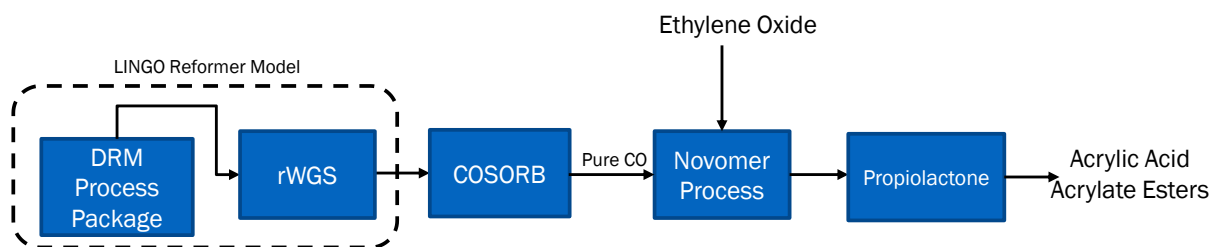
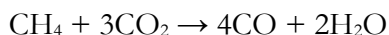


Figure 52 - Utilization of DRM to produce CO as feedstock for Propiolactone

Since a high CO content is desired, the feed to the DRM unit can be tuned to maximize CO. The stoichiometric reaction for that would be as follows:



This reaction is also called ‘Super Dry Reforming’ [144] and uses 3 moles of CO₂ per mole of methane consumed. This is input as a constraint to the LINGO model. However, due to the equilibrium limitations, some H₂ still remains as shown in Table 18.

Table 18 - Results from Optimization Model for CO₂/CH₄=3

| | |
|---|---------------------------------------|
| Input feed: CO ₂ /CH ₄ =3 | |
| H ₂ /CO ratio of syngas | 0.4 |
| N _{CO} /N _{CH₄} | 2.85 |
| N _{H₂} /N _{CH₄} | 1.14 |
| Cost of Production | \$0.93/kmol |
| Carbon footprint of syngas production | -0.4097 kg CO ₂ /kg Syngas |

This indicates that further treatment may be required to purify the CO stream. Hence, a COSORB unit will still be required to produce the CO stream. Accounting for the COSORB unit emissions and operating costs, we can estimate the cost and carbon footprint of CO production by this 'Modified DRM+COSORB' process, which is shown in Figure 53 and Figure 54. The Modified DRM+COSORB shows a significant decrease in operating cost when compared with a POX+COSORB unit. The carbon footprint is still impressively in the negative region which indicates that till the CO generation, the whole process is still CO₂ negative, and this is due to the high molar ratio of CO₂/CH₄ in the feed of 3.

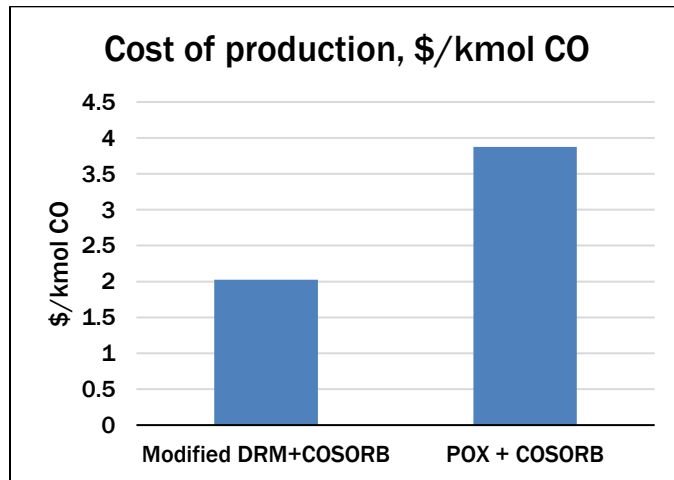


Figure 53 - Estimated production cost of CO

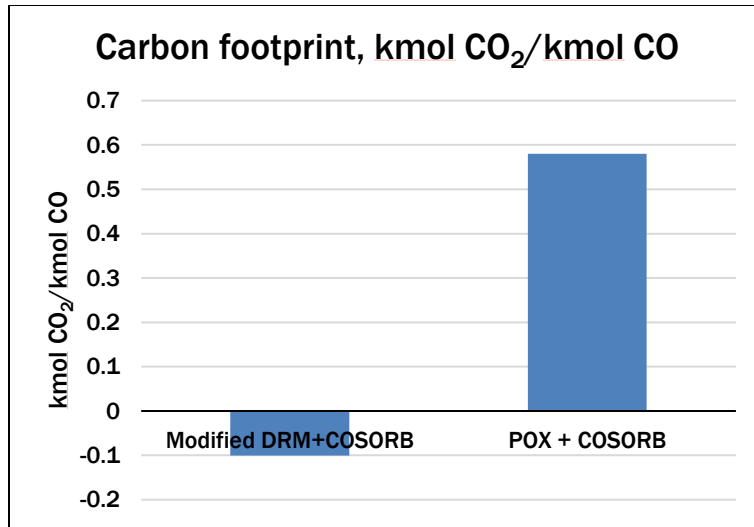


Figure 54 - Carbon footprint of CO production

5.4. Carbon footprint and Operating Costs for Methane Decomposition

In all the analysis in this chapter, carbon deposition was given a penalty as it was converted to CO₂ in the carbon footprint equation. Hence, after maximizing syngas, when we minimize the overall carbon footprint, the operating points which involve methane decomposition are discarded. The methane decomposition reaction, if allowed produces 2 moles of valuable hydrogen in the absence of any oxidant. To better understand the relation of operating temperature and overall CO₂ emissions, the reformer operating temperature was fixed at 1100 °C, 900 °C, and 700 °C, and the overall CO₂ emissions were computed using the model.

By extending the syngas ratio range and allowing for coke formation, this will set the targets of CO₂ emissions using only DRM if a future generation catalyst is developed that can handle large amounts of coke. The regeneration process will have a major impact on the CO₂ balance and hence both cases are considered – coke burnt in air to regenerate the catalyst and coke removed physically as solid carbon. Catalyst Regeneration by burning in air is a well-established procedure widely followed in the oil and gas industry, but the case of physical removal is a hypothetical case and has been included to study the magnitude of impact of catalyst regeneration on overall CO₂ emissions.

DRM is studied at 3 different temperatures – with different cases based on the catalyst regeneration procedure. Coke formation is allowed, and this enhances the syngas ratio that can be produced by

DRM. Coke originating from the carbon in methane will release the hydrogen thus boosting the syngas ratio. The first case (solid line) refers to the typical catalyst regeneration procedure practiced in the industry of burning coke in air at high temperatures. Whereas the second case (dotted line) refers to the removal of coke by a physical process so that the coke is removed as solid carbon and is not converted to CO₂.

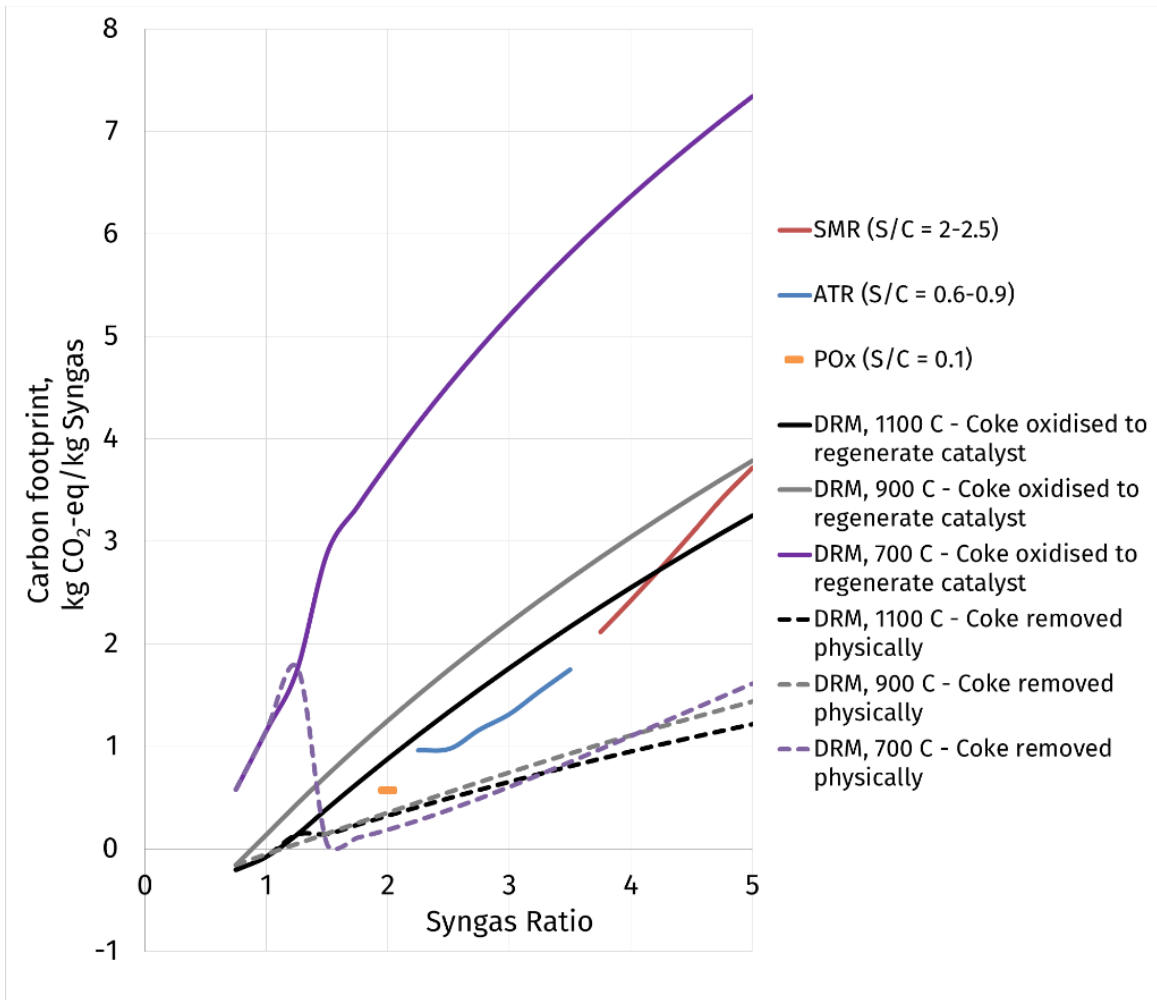


Figure 55 – Carbon footprint Comparison for DRM (higher syngas ratios with coke formation allowed). Reprinted from [40]

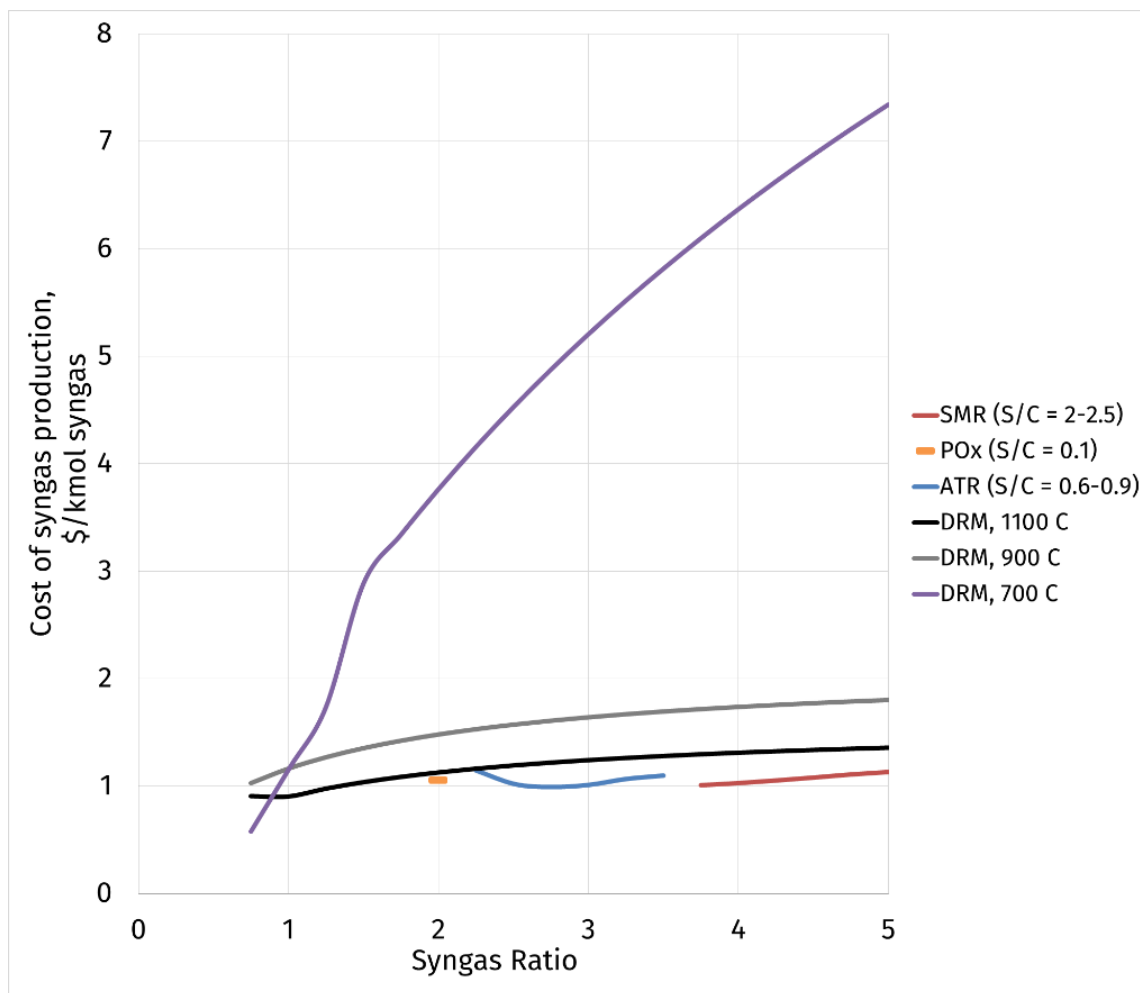


Figure 56 – Operating Cost Comparison for DRM (higher syngas ratios with coke formation allowed). Reprinted from [40]

The results for the DRM operating at 700 °C, 900 °C and 1100 °C are shown in and Figure 56. The carbon footprint comparison clearly shows that reducing the operating temperature of DRM does not necessarily reduce carbon footprint/mole of syngas produced. This substantiates the need for higher temperatures and DRM experimental studies should be performed at these temperatures to simulate realistic reformer conditions.

Secondly, the overall carbon footprint is highly dependent on the type of catalyst regeneration employed. At high syngas ratios of 2 and 3, even if a DRM catalyst is able to recover sufficient activity after regeneration, the overall carbon footprint will still be more than that of POX and ATR

respectively. The carbon footprint at higher syngas ratios is lesser than conventional processes only if a method is found to remove the coke as solid carbon.

However, for both cases of catalyst regeneration, the cost of syngas production exceeds that of conventional technologies at all syngas ratios as shown in Figure 56. These results provide guidance to future DRM experimental studies towards operating conditions with lower carbon footprints. For the hypothetical case of coke removed as solid carbon, if the coke is sold, this will significantly alter the process economics of this case.

DRM at low temperature (around 700 °C) results in a large amount of coke formation and low conversions resulting in prohibitive operating costs. The CO₂ balance is highly impacted by coke management. Burning off coke with air makes the CO₂ emissions of the overall process exceed that of conventional processes. If the coke can be removed physically without affecting the catalyst performance, only then can the DRM produce syngas of high syngas ratios with lower CO₂ emissions.

5.5. Conclusion

This chapter identifies the scenarios where syngas produced from DRM can have a lower carbon footprint and competitive operating costs when compared to conventional processes. The appropriate pathway depends on the H₂/CO ratio requirement of downstream processing units.

For H₂/CO requirement of 2 and above, the DRM+COSORB process is a promising pathway, however the CO captured should be sold to an external customer at \$75/tonne and the CO₂ used for DRM should be available without any associated purification costs.

For H₂/CO requirement of 1, the FTO pathway seems to have good economic potential. The sensitivity of CO₂ purification cost would depend on the process pathway being compared.

For H₂/CO requirement of 0, which means a pure CO stream, the CO₂/CH₄ feed ratio to DRM can be tuned to maximize CO production and this pathway has much lower carbon footprint and operating cost when compared to conventional syngas production pathways.

The analysis presented here highlights the area where DRM assisted processes show potential and also identifies scenarios where DRM does not have an impact on overall plant carbon footprint and process economics.

6. CONCLUSIONS AND FUTURE WORK

This work uses a multi-scale approach in addressing the challenges of the DRM reaction system. In the catalysis work, the first part deals with comparing the dynamic changes in in-situ dispersion for uncoated Commercial catalyst and 5-ALD catalyst. A binary in-situ H₂-CO chemisorption technique was used for estimating the dispersion of Ni over 40 h TOS. The rate of decrease in dispersion for the uncoated Commercial catalyst was $\sim 0.11\%h^{-1}$ as opposed to $0.025\%h^{-1}$ for the 5-ALD catalyst. The alumina overcoat on the 5-ALD catalyst helps sustain the dispersion better, for the 40 h of DRM. TEM imaging was used as a more direct measure of sintering. The average crystallite size for the Commercial catalyst increased from 8.5 nm to 24.5 nm, while for the same time-on-stream in the DRM atmosphere, the 5-ALD catalyst maintains its original average crystallite size of about 8.7 nm. The coke formation rate in the 5-ALD catalyst was almost half that of the Commercial catalyst.

In the second part of the catalysis work, 20-ALD catalysts were annealed and the effect of different parameters of the annealing process was investigated. The parameters chosen were Deposition Temperature, Annealing Temperature, and Heating Rate. It was found that Deposition Temperature has the maximum effect and affect the BET surface area and catalytic activity positively. A modification of the annealing process, wherein the temperature was ramped to 800 °C at the rate of 5 °C/min was performed whilst flowing DRM gas over the catalyst. It was found that the catalyst activity of the 20-ALD is better and more stable than the uncoated Commercial catalyst. TEM and SEM images seem to suggest the slow crystallization of alumina in the overcoat. TEM images and Raman spectroscopy show distinct carbon onions formation. The parameters which affect this phenomenon were listed.

Chapters 4 and 5 are focused on the macro-scale of the work. Chapter 4 reports a detailed assessment of the Life Cycle Analysis for several syngas production processes. The study included an optimization model as well that was built in LINGO to estimate the carbon emissions and operating cost of each reforming pathway. This study presents a systematic approach to evaluate the impact of DRM on the carbon footprint of existing syngas production units. The optimization-based approach helped to find operating conditions for each reformer type and their overall CO₂ emissions are compared for specific H₂/CO ratios. All major emission sources in the syngas production process have been accounted for.

The carbon footprint comparison of different processes indicates that DRM has a negative and very low carbon footprint at low syngas ratios of 1 and below. For parallel combination of reformer units to produce a syngas of higher H_2/CO ratio, any addition of a DRM unit in parallel with existing reforming processes does not result in a reduction of overall CO_2 emissions and in some cases might increase overall CO_2 emissions slightly. This indicates that the syngas ratio is the main bottleneck in utilizing the carbon fixation potential of DRM. Of all the cases considered in the study, it was found that the DRM+COSORB process has a substantial reduction of overall CO_2 emissions as well as a reduction in operating costs (provided that the captured CO after syngas ratio adjustment is sold an external customer and the required CO_2 is available without any additional purification costs). By avoiding the route of combination with other syngas production technologies, DRM+COSORB utilizes the CO_2 utilization potential of DRM whilst producing two valuable streams – a high H_2/CO ratio syngas and a pure CO stream. Due to the novelty of the process, a patent application has been filed for the DRM+COSORB process [145]. One aspect that should be highlighted is that the captured CO must be utilized as a feedstock and not burnt as fuel to maintain the LCA benefit from the CO_2 life cycle perspective. The CO_2 source quality also has an important role to play in the overall process economics. The CO_2 feed for DRM should be sourced from a pure stream with no energy being spent to purify the CO_2 stream. A probable candidate for such a stream would be the CO_2 stream from the acid gas recovery unit of an LNG plant. Using the results of the study, various downstream pathways were identified based on the H_2/CO ratio requirement of the processes. If the DRM syngas is to be used directly, without any H_2/CO ratio adjustment step, the Fischer-Tropsch to Olefins route is promising and has a high economic potential based on the preliminary economic assessment. In this case, even if CO_2 is sourced from flue gas, with about \$50/tonne, the process still shows potential and hence warrants further analysis. More detailed simulation studies of this process and experimental studies for proof-of-concept will be needed to prove the techno-economic viability of this path for syngas production. If pure CO is the desired product, DRM is an excellent choice. This is because, through the ‘Super Dry Reforming’ route, the CO yield per mole of methane can be highly enhanced compared to other processes.

The results presented here can guide further experimental studies on DRM towards a more holistic approach of studying the overall picture of CO_2 emissions throughout the plant, instead of merely

focusing on the reformer unit and using CO₂ conversion as the metric to compare different options. Since the optimization model presented here deals with the production of synthesis gas, which is the starting raw material for a variety of petrochemicals, it can be readily combined with existing downstream emissions models to compare the environmental and economic performance of different pathways to produce the same product. This will pave the way for incorporating CO₂ in natural/shale gas monetization pathways in individual plants and eco-industrial parks integrating materials from multiple plants [146]–[148].

The unique aspect of this work is the emphasis on all major issues of the DRM process. As demonstrated, the findings in the catalyst design can aid in designing more efficient ALD catalysts with the right annealing conditions to enhance the porosity of the ALD overcoat and enhancing the catalytic performance. Combined with the LCA model, which has the capability to estimate the carbon footprints and operating costs for various pathways, this contribution addresses each challenge of the DRM process at the micro and macro-scale. The promising catalysts identified, experimental techniques, and processes identified by the LCA study show good potential for DRM, thereby paving the way for his work to be continued to the next stage of scale-up for further investigations. The tools and experimental methods developed herein will be quite valuable in the design of more efficient ALD catalysts and the overall process development of DRM for commercialization. Directions of future research anticipated in this area are listed below:

- For ALD catalysis, the use of commercial pellet catalyst modified by ALD should be explored to ensure that the same TPSR protocol gives the same results as that for the powder catalyst
- The hypothesis of an increase in dispersion by TPSR should be verified - a chemisorption experiment performed before and after TPSR can help to study changes in dispersion
- For the process engineering part of DRM, a detailed COSORB model needs to be formulated with a focus on the absorber column to get better estimates of energy consumption and product quality
- Incorporation of carbon tax into the analysis which would provide some financial incentive for DRM assisted processes.

REFERENCES

- [1] EIA, “Natural gas explained,” 2019. [Online]. Available: <https://www.eia.gov/energyexplained/natural-gas/use-of-natural-gas.php>.
- [2] V. Swarup, “Energy Outlook: Role of Natural Gas, 12th Natural Gas Conversion Symposium.” San Antonio, TX, 2019.
- [3] J. Clark, “Bond Enthalpies.” [Online]. Available: [https://chem.libretexts.org/Bookshelves/Physical_and_Theoretical_Chemistry_Textbook_Maps/Supplemental_Modules_\(Physical_and_Theoretical_Chemistry\)/Thermodynamics/Energies_and_Potentials/Enthalpy/Bond_Enthalpies](https://chem.libretexts.org/Bookshelves/Physical_and_Theoretical_Chemistry_Textbook_Maps/Supplemental_Modules_(Physical_and_Theoretical_Chemistry)/Thermodynamics/Energies_and_Potentials/Enthalpy/Bond_Enthalpies).
- [4] A. Al-Douri, D. Sengupta, and M. M. El-Halwagi, “Shale gas monetization - A review of downstream processing to chemicals and fuels,” *J. Nat. Gas Sci. Eng.*, vol. 45, no. 17, pp. 436–455, Sep. 2017.
- [5] Andrea P. Ortiz-Espinoza *et al.*, “Design, simulation and techno-economic analysis of two processes for the conversion of shale gas to ethylene,” *Comput. Chem. Eng.*, vol. 107, pp. 237–246, May 2017.
- [6] S. Pérez-Uresti, J. Adrián-Mendiola, M. El-Halwagi, and A. Jiménez-Gutiérrez, “Techno-Economic Assessment of Benzene Production from Shale Gas,” *Processes*, vol. 5, no. 3, 2017.
- [7] P. Thiruvenkataswamy, F. T. Eljack, N. Roy, M. S. Mannan, and M. M. El-Halwagi, “Safety and techno-economic analysis of ethylene technologies,” *J. Loss Prev. Process Ind.*, vol. 39, pp. 74–84, 2016.
- [8] V. M. Ehlinger, K. J. Gabriel, M. M. B. Noureldin, and M. M. El-Halwagi, “Process Design and Integration of Shale Gas to Methanol,” *ACS Sustain. Chem. Eng.*, vol. 2, pp. 30–37, 2014.
- [9] C. Karakaya and R. J. Kee, “Progress in the direct catalytic conversion of methane to fuels and chemicals,” *Prog. Energy Combust. Sci.*, vol. 55, pp. 60–97, 2016.
- [10] H. E. Alfadala and M. M. El-Halwagi, “Qatar’s chemical industry: Monetizing natural gas,” *Chem. Eng. Prog.*, vol. 113, no. 2, pp. 38–41, 2017.
- [11] Ottmar Edenhofer *et al.*, “Working Group III Contribution to the Fifth Assessment Report of the Intergovernmental Panel on Climate Change (IPCC),” 2014.
- [12] US EPA, “Overview of Greenhouse Gases,” 2015. [Online]. Available: <https://www.epa.gov/ghgemissions/overview-greenhouse-gases>. [Accessed: 25-Sep-2017].
- [13] O. Edenhofer, “Mitigation of Climate Change Working Group III Contribution to the Fifth

- Assessment Report of the Intergovernmental Panel on Climate Change,” 2014.
- [14] M. Aresta, A. Dibenedetto, and A. Angelini, “The changing paradigm in CO₂ utilization,” *J. CO₂ Util.*, vol. 3, no. 4, pp. 65–73, 2013.
- [15] A. Al-Mamoori, A. Krishnamurthy, A. A. Rownaghi, and F. Rezaei, “Carbon Capture and Utilization Update,” *Energy Technol.*, vol. 5, no. 6, pp. 834–849, 2017.
- [16] F. Manenti, “CO₂ as feedstock: a new pathway to syngas,” *Comput. Aided Chem. Eng.*, vol. 37, no. December, pp. 1049–1054, 2015.
- [17] P. M. Mortensen and I. Dybkjær, “Industrial Scale Experience on Steam Reforming of CO₂-Rich Gas,” *Appl. Catal. A Gen.*, vol. 495, pp. 141–151, 2015.
- [18] L. S. Tan, K. K. Lau, M. A. Bustam, and A. M. Shariff, “Removal of high concentration CO₂ from natural gas at elevated pressure via absorption process in packed column,” *J. Nat. Gas Chem.*, vol. 21, pp. 7–10, 2012.
- [19] A. Abdulrasheed, A. A. Jalil, Y. Gambo, M. Ibrahim, H. U. Hambali, and M. Y. Shahul Hamid, “A review on catalyst development for dry reforming of methane to syngas: Recent advances,” *Renew. Sustain. Energy Rev.*, vol. 108, no. November 2018, pp. 175–193, 2019.
- [20] D. Pakhare and J. Spivey, “A review of dry (CO₂) reforming of methane over noble metal catalysts,” *Chem. Soc. Rev.*, vol. 43, no. 5, p. , 2014.
- [21] B. Abdullah, N. Azeanni, A. Ghani, D.-V. N. Vo, N. A. Abd Ghani, and D.-V. N. Vo, “Recent advances in dry reforming of methane over Ni-based catalysts,” *J. Clean. Prod.*, vol. 162, pp. 170–185, Sep. 2017.
- [22] S. Afzal *et al.*, “Controlling the rate of change of Ni dispersion in commercial catalyst by ALD overcoat during dry reforming of methane,” *Int. J. Hydrogen Energy*, vol. 45, pp. 12835–12848, 2020.
- [23] Dori Yosef Kalai, “Dry reforming of methane: catalyst development and thermodynamic analysis,” 2015.
- [24] R. Dębek, M. Motak, T. Grzybek, M. Galvez, and P. Da Costa, “A Short Review on the Catalytic Activity of Hydrotalcite-Derived Materials for Dry Reforming of Methane,” *Catalysts*, vol. 7, no. 12, p. 32, 2017.
- [25] G. Zhang, J. Liu, Y. Xu, and Y. Sun, “A review of CH₄–CO₂ reforming to synthesis gas over Ni-based catalysts in recent years (2010–2017),” *Int. J. Hydrogen Energy*, vol. 43, no. 32, pp. 15030–15054, 2018.

- [26] B. J. O'Neill *et al.*, “Catalyst Design with Atomic Layer Deposition,” *ACS Catal.*, vol. 5, p. 1804–1825, 2015.
- [27] “Riogen 20% Ni/Al₂O₃,” 2016. [Online]. Available: <https://shop.riogeninc.com/product.sc?productId=6182&categoryId=2>.
- [28] “Alumina Price,” *Forbes*, 2018. [Online]. Available: <https://www.forbes.com/sites/timtreadgold/2018/09/26/high-alumina-prices-underline-surprise-strength-in-bulk-commodities/#1c05b5a753c7>.
- [29] Indexmundi, “Platinum Commodity Prices,” 2020. [Online]. Available: <https://www.indexmundi.com/commodities/?commodity=platinum>.
- [30] C. Song, “Global challenges and strategies for control, conversion and utilization of CO₂ for sustainable development involving energy, catalysis, adsorption and chemical processing,” *Catal. Today*, vol. 115, no. 1–4, pp. 2–32, 2006.
- [31] M. S. S. Challiwala *et al.*, “A combined thermo-kinetic analysis of various methane reforming technologies: Comparison with dry reforming,” *J. CO₂ Util.*, vol. 17, pp. 99–111, 2017.
- [32] S. Afzal, D. Sengupta, M. M. El-Halwagi, and N. Elbashir, *Minimizing CO₂ emissions for syngas production units using Dry Reforming of Methane*, vol. 40. 2017.
- [33] Hydrocarbon Processing, *2019 Gas Processes Handbook*. 2019.
- [34] S. Ewald, S. Standl, and O. Hinrichsen, “Characterization of nickel catalysts with transient methods,” *Appl. Catal. A Gen.*, vol. 549, no. September 2017, pp. 93–101, 2018.
- [35] M. A. Cauqui *et al.*, “Some contributions of electron microscopy to the characterisation of the strong metal–support interaction effect,” *Catal. Today*, vol. 77, no. 4, pp. 385–406, 2003.
- [36] H. Friedrich, P. E. de Jongh, A. J. Verkleij, and K. P. de Jong, “Electron Tomography for Heterogeneous Catalysts and Related Nanostructured Materials,” *Chem. Rev.*, vol. 109, no. 5, pp. 1613–1629, 2009.
- [37] M. Che and C. O. Bennett, “The Influence of Particle Size on the Catalytic Properties of Supported Metals,” *Adv. Catal.*, vol. 36, pp. 55–172, Jan. 1989.
- [38] G. Prieto, J. Zečević, H. Friedrich, K. P. De Jong, and P. E. De Jongh, “Towards stable catalysts by controlling collective properties of supported metal nanoparticles,” *Nat. Mater.*, vol. 12, no. 1, pp. 34–39, 2013.
- [39] C. H. Bartholomew and R. J. Farrauto, *Fundamentals of Industrial Catalytic Processes*, Second Edi. Hoboken, NJ, USA: John Wiley & Sons, Inc., 2005.

- [40] S. Afzal, D. Sengupta, A. Sarkar, M. M. El-Halwagi, and N. O. Elbashir, "Optimization Approach to the Reduction of CO₂ Emissions for Syngas Production Involving Dry Reforming," *ACS Sustain. Chem. Eng.*, vol. 6, p. 7532–7544, 2018.
- [41] H. Van Bui, F. Grillo, and J. R. Van Ommen, "Atomic and molecular layer deposition: off the beaten track," *Chem. Commun. Chem. Commun.*, vol. 53, no. 53, pp. 45–71, 2017.
- [42] Y. Zhao, Y. Kang, H. Li, and H. Li, "CO₂ conversion to synthesis gas *via* DRM on the durable Al₂O₃/Ni/Al₂O₃ sandwich catalyst with high activity and stability," *Green Chem.*, vol. 20, no. 12, pp. 2781–2787, 2018.
- [43] E. Baktash, P. Littlewood, R. Schomäcker, A. Thomas, and P. C. Stair, "Alumina coated nickel nanoparticles as a highly active catalyst for dry reforming of methane," *Appl. Catal. B Environ.*, vol. 179, pp. 122–127, 2015.
- [44] B. J. O. Neill *et al.*, "Stabilization of Copper Catalysts for Liquid-Phase Reactions by Atomic Layer Deposition," *Angew. Chemie*, vol. 125, pp. 14053–14057, 2013.
- [45] T. Li *et al.*, "Tailoring nanopore formation in atomic layer deposited ultrathin films," *J. Vac. Sci. Technol. A Vacuum, Surfaces, Film.*, vol. 36, no. 1, p. 01A103, 2017.
- [46] C. H. Bartholomew, "Sintering kinetics of supported metals: new perspectives from a unifying GPLE treatment," *Appl. Catal. A Gen.*, vol. 107, no. 1, pp. 1–57, 1993.
- [47] J. Sehested, J. A. P. Gelten, and S. Helveg, "Sintering of nickel catalysts: Effects of time, atmosphere, temperature, nickel-carrier interactions, and dopants," *Appl. Catal. A Gen.*, vol. 309, no. 2, pp. 237–246, 2006.
- [48] F. B. Rasmussen, J. Sehested, H. T. Teunissen, A. M. Molenbroek, and B. S. Clausen, "Sintering of Ni/Al₂O₃ catalysts studied by anomalous small angle X-ray scattering," *Appl. Catal. A Gen.*, vol. 267, pp. 165–173, 2004.
- [49] M. Claeys, S. Kelly, E. Van Steen, K. Visagie, I. Krylov, and S. Africa, "Development of a magnetometer for in-situ catalyst characterization," *Time*, no. c, pp. 2–3, 1947.
- [50] D. G. Mustard and C. H. Bartholomew, "Determination of metal crystallite size and morphology in supported nickel catalysts," *J. Catal.*, vol. 67, no. 1, pp. 186–206, 1981.
- [51] J. Sehested, J. A. P. Gelten, I. N. Remediakis, H. Benggaard, and J. K. Nørskov, "Sintering of nickel steam-reforming catalysts: Effects of temperature and steam and hydrogen pressures," *J. Catal.*, vol. 223, no. 2, pp. 432–443, 2004.
- [52] J. R. Rostrup-Nielsen, "Some Principles Relating to the Regeneration of Sulfur-Poisoned

- Nickel Catalyst,” *J. Catal.*, vol. 21, pp. 171–178, 1971.
- [53] Paal and Manon, *Hydrogen Effects in Catalysis: Fundamentals and Practical Applications*. CRC Press, 1987.
- [54] M. M. D. Baker and E. K. Rideal, “The adsorption of carbon monoxide by nickel,” *Trans. Faraday Soc.*, vol. 51, pp. 1597–1601, 1955.
- [55] J. Lapujoulade and K. S. Neil, “Chemisorption of hydrogen on the (111) plane of nickel,” *J. Chem. Phys.*, vol. 57, no. 8, pp. 3535–3545, 1972.
- [56] G. Wedler, H. Papp, and G. Schroll, “The Interaction of Hydrogen and Carbon Monoxide on Polycrystalline Nickel Films at Temperatures up to 353 K,” *J. Catal.*, vol. 38, pp. 153–165, 1975.
- [57] F. Notheisz, A. G. Zsigmond, and M. Bartok, “Determination of the Surface Area of Nickel Catalyst by a Chromatographic Pulse Method (Carbon Monoxide-Hydrogen Titration),” *J. Chromatogr.*, vol. 241, pp. 101–102, 1982.
- [58] C. H. Bartholomew, R. B. Pannell, and J. L. Butler, “Support and crystallite size effects in CO hydrogenation on nickel,” *J. Catal.*, vol. 65, no. 2, pp. 335–347, 1980.
- [59] B. J. O’Neill, C. Sener, D. H. K. Jackson, T. F. Kuech, and J. A. Dumesic, “Control of thickness and chemical properties of atomic layer deposition overcoats for stabilizing Cu/ γ -Al₂O₃ catalysts,” *ChemSusChem*, vol. 7, no. 12, pp. 3247–3251, 2014.
- [60] J. R. H. Ross, M. C. F. Steel, and A. Zeini-Isfahani, “Evidence for the Participation of Surface Nickel Aluminate in the Steam Reforming of Methane over Nickel/Alumina Catalysts,” *Journal Catal.*, vol. 52, pp. 280–290, 1978.
- [61] D. Häussermann *et al.*, “Is the CO₂ Methanation on Highly Loaded Ni-Al₂O₃ Catalysts Really Structure-Sensitive?,” *Appl. Catal. B Environ.*, vol. 247, no. December 2018, pp. 200–219, 2018.
- [62] P. Littlewood, S. Liu, E. Weitz, T. J. Marks, and P. C. Stair, “Ni-alumina dry reforming catalysts: Atomic layer deposition and the issue of Ni aluminate,” *Catal. Today*, no. August 2018, 2019.
- [63] J. L. Carter, J. A. Cusumano, and J. H. Sinfelt, “Catalysis over supported metals. V. The effect of crystallite size on the catalytic activity of nickel,” *J. Phys. Chem.*, vol. 70, no. 7, pp. 2257–2263, 1966.
- [64] T. Nakayama, M. Arai, and Y. Nishiyama, “Formation of pitted particles and redispersion in

- supported nickel catalysts during heating in oxygen and hydrogen,” *J. Catal.*, vol. 79, no. 2, pp. 497–500, 1983.
- [65] M. Argyle and C. Bartholomew, “Heterogeneous Catalyst Deactivation and Regeneration: A Review,” *Catalysts*, vol. 5, no. 1, pp. 145–269, Feb. 2015.
- [66] K. Morgan, A. Goguet, and C. Hardacre, “Metal redispersion strategies for recycling of supported metal catalysts: A perspective,” *ACS Catal.*, vol. 5, no. 6, pp. 3430–3445, 2015.
- [67] L. Silvester, A. Antzara, G. Boskovic, E. Heracleous, A. A. Lemonidou, and D. B. Bukur, “NiO supported on Al₂O₃ and ZrO₂ oxygen carriers for chemical looping steam methane reforming,” *Int. J. Hydrogen Energy*, vol. 40, no. 24, pp. 7490–7501, 2015.
- [68] T. D. Gould, A. Izar, A. W. Weimer, J. L. Falconer, and J. W. Medlin, “Stabilizing Ni Catalysts by Molecular Layer Deposition for Harsh, Dry Reforming Conditions,” *ACS Catal.*, vol. 4, no. 8, pp. 2714–2717, 2014.
- [69] K. O. Christensen, D. Chen, R. Lødeng, and A. Holmen, “Effect of supports and Ni crystal size on carbon formation and sintering during steam methane reforming,” *Appl. Catal. A Gen.*, vol. 314, no. 1, pp. 9–22, 2006.
- [70] T. W. Hansen, A. T. Delariva, S. R. Challa, and A. K. Datye, “Sintering of Catalytic Nanoparticles : Particle Migration or Ostwald Ripening ?,” *Acc. Chem. Res.*, vol. 46, no. 8, pp. 1720–1730, 2013.
- [71] C. H. Bartholomew and R. B. Pannell, “The stoichiometry of hydrogen and carbon monoxide chemisorption on alumina- and silica-supported nickel,” *J. Catal.*, vol. 65, no. 2, pp. 390–401, 1980.
- [72] S. Svelle and M. Bjørgen, “Selective Catalysts for Petrochemical Industry - Shape Selectivity in Microporous Materials,” in *Selective Nanocatalysts and Nanoscience: Concepts for Heterogeneous and Homogeneous Catalysis*, A. Zecchina, S. Bordiga, and E. Groppo, Eds. Wiley-VCH Verlag GmbH & Co. KGaA, 2011, p. 249.
- [73] P. Rallapalli, P. K. Prabhakaran, D. Patel, R. S. Somani, R. V. Jasra, and H. C. Bajaj, “Sorption studies of CO₂, CH₄, N₂, CO, O₂ and Ar on nanoporous aluminum terephthalate [MIL-53(Al)],” *J. Porous Mater.*, no. April, 2010.
- [74] G. Férey, “Hybrid porous solids: past, present, future,” *Chem. Soc. Rev.*, vol. 37, no. 1, pp. 191–214, 2008.
- [75] M. A. Cameron, I. P. Gartland, J. A. Smith, S. F. Diaz, and S. M. George, “Atomic Layer

- Deposition of SiO₂ and TiO₂ in Alumina Tubular Membranes: Pore Reduction and Effect of Surface Species on Gas Transport,” *Langmuir*, vol. 16, no. 19, pp. 7435–7444, 2002.
- [76] A. Giehr, L. Maier, S. A. Schunk, and O. Deutschmann, “Thermodynamic Considerations on the Oxidation State of Co/Al₂O₃ and Ni/Al₂O₃ Catalysts under Dry and Steam Reforming Conditions,” *ChemCatChem*, vol. 10, no. 1, pp. 751–757, 2018.
- [77] C.H. Bartholomew, “Response to Comments on ‘Nickel-Support Interactions: Their Effects on Particle Morphology, Adsorption, and Activity Selectivity Properties,’” *Ind. Eng. Chem. Prod. Res. Dev.*, vol. 21, p. 523, 1982.
- [78] J. Lu *et al.*, “Coking- and Sintering-Resistant Palladium Catalysts Achieved Through Atomic Layer Deposition,” *Science (80-.)*, vol. 335, no. 6073, pp. 1205–1208, 2012.
- [79] K. O. Christensen, “Steam reforming of methane on different nickel catalysts,” PhD thesis, Norwegian University of Science and Technology, 2005.
- [80] H. S. Benggaard *et al.*, “Steam Reforming and Graphite Formation on Ni Catalysts,” *J. Catal.*, vol. 209, no. 2, pp. 365–384, 2002.
- [81] B. H. Sakakini and A. S. Verbrugge, “Temperature-programmed surface reaction as a means of characterizing supported-metal catalysts and probing their surface reactivity,” *J. Chem. Soc. Faraday Trans.*, vol. 93, pp. 1637–1640, 1997.
- [82] A. Goulas and J. R. Van Ommen, “Scalable Production of Nanostructured Particles using Atomic Layer Deposition,” *KONA Powder Part. J.*, vol. 31, pp. 234–246, 2014.
- [83] A. W. Weimer, “Particle atomic layer deposition,” *J Nanopart Res*, vol. 21, no. 9, 2019.
- [84] V. Danghyan, S. Calderon Novoa, A. Mukasyan, and E. E. Wolf, “Pressure dilution, a new method to prepare a stable Ni/fumed silica catalyst for the dry reforming of methane,” *Appl. Catal. B Environ.*, vol. 234, no. November 2017, pp. 178–186, 2018.
- [85] E. K. Baumert, P. O. Theillet, and O. N. Pierron, “Fatigue-resistant silicon films coated with nanoscale alumina layers,” *Scr. Mater.*, vol. 65, no. 7, pp. 596–599, 2011.
- [86] P. F. Carcia, R. S. McLean, M. H. Reilly, M. D. Groner, and S. M. George, “Ca test of Al₂O₃ gas diffusion barriers grown by atomic layer deposition on polymers,” *Appl. Phys. Lett.*, vol. 89, no. 3, pp. 1–4, 2006.
- [87] Z. Qiao, J. Li, N. Zhao, C. Shi, and P. Nash, “Graphitization and microstructure transformation of nanodiamond to onion-like carbon,” *Scr. Mater.*, vol. 54, no. 2, pp. 225–229, 2006.

- [88] K. Bogdanov *et al.*, “Annealing-induced structural changes of carbon onions: High-resolution transmission electron microscopy and Raman studies,” *Carbon N. Y.*, vol. 73, pp. 78–86, 2014.
- [89] K. VL and B. YuV, “Nanodiamond graphitization and properties of onion-like carbon,” in *Synthesis, properties and applications of ultrananocrystalline diamond*, V. aYa Gruen DM, Shenderova OA, Ed. Dordrecht: Springer, 2005, pp. 199–216.
- [90] C. Santangelo, S.; Messina, G.; Faggio, G.; Lanza, M.; Milone, “Evaluation of crystalline perfection degree of multi-walled carbon nanotubes: correlations between thermal kinetic analysis and micro-Raman spectroscopy,” *J. Raman Spectrosc.*, vol. 42, no. 4, pp. 593–602, 2011.
- [91] K. A. Rasmussen, K.; Mast, J.; De Temmerman, P.-J.; Verleysen, E.; Waegeneers, N.; Van Steen, J.; Pizzolon, J. C.; De Temmerman, L.; Van Doren, E.; Jensen, “Multi-walled carbon nanotubes, NM-400, NM-401, NM-402, NM-403: characterisation and physico-chemical properties,” *JRC Repos. NM-series Represent. Manuf. Nanomater.*, 2014.
- [92] C. A. Allegri, M.; Perivoliotis, D. K.; Bianchi, M. G.; Chiu, M.; Pagliaro, A.; Koklioti, M. A.; Trompeta, A.-F. A.; Bergamaschi, E.; Bussolati, O.; Charitidis, “Toxicity determinants of multi-walled carbon nanotubes: the relationship between functionalization and agglomeration,” *Toxicol. Reports*, vol. 3, pp. 230–243, 2016.
- [93] M. Zeiger, N. Jäckel, V. N. Mochalin, and V. Presser, “Review: Carbon onions for electrochemical energy storage,” *J. Mater. Chem. A*, vol. 4, no. 9, pp. 3172–3196, 2016.
- [94] K. Bogdanov *et al.*, “Annealing-induced structural changes of carbon onions: High-resolution transmission electron microscopy and Raman studies,” *Carbon N. Y.*, vol. 73, pp. 78–86, 2014.
- [95] V. Lehman, J. H.; Terrones, M.; Mansfield, E.; Hurst, K. E.; Meunier, “Evaluating the characteristics of multiwall carbon nanotubes,” *Carbon N. Y.*, vol. 49, no. 8, pp. 2581–2602, 2011.
- [96] B. Heise, H.; Kuckuk, R.; Ojha, A.; Srivastava, A.; Srivastava, V.; Asthana, “Characterisation of carbonaceous materials using Raman spectroscopy: a comparison of carbon nanotube filters, single- and multi-walled nanotubes, graphitised porous carbon and graphite,” *J. Raman Spectrosc. An Int. J. Orig. Work all Asp. Raman Spectrosc. Incl. High. Order Process. also Brillouin Rayleigh Scatt.*, vol. 40, no. 3, pp. 344–353, 2009.
- [97] M. Saito, R.; Hofmann, M.; Dresselhaus, G.; Jorio, A.; Dresselhaus, “Raman spectroscopy of graphene and carbon nanotubes,” *Adv. Phys.*, vol. 60, no. 3, pp. 413–550, 2011.

- [98] M. Bokobza, L.; Rahmani, “Carbon nanotubes: Exceptional reinforcing fillers for silicone rubbers,” *KGK. Kautschuk, Gummi, Kunststoffe*, vol. 62, no. 3, pp. 112–117, 2009.
- [99] H. Qin, P. Sutter, and G. Zhou, “The crystallization of amorphous aluminum oxide thin films grown on NiAl (100),” *J. Am. Ceram. Soc.*, vol. 97, no. 9, pp. 2762–2769, 2014.
- [100] D. M. Anjos *et al.*, “Pseudocapacitance and performance stability of quinone-coated carbon onions,” *Nano Energy*, vol. 2, no. 5, pp. 702–712, 2013.
- [101] D. Pech *et al.*, “Ultra-high-power micrometre-sized supercapacitors based on onion-like carbon,” *Nat. Nanotechnol.*, vol. 5, no. 9, pp. 651–654, 2010.
- [102] J. K. McDonough and Y. Gogotsi, “Carbon onions: Synthesis and electrochemical applications,” *Electrochem. Soc. Interface*, vol. 22, no. 3, pp. 61–66, 2013.
- [103] J. R. H. Ross, “Syngas Production Using Carbon Dioxide Reforming: Fundamentals and Perspectives,” in *Transformation and Utilization of Carbon Dioxide*, B. M. Bhanage and M. Arai, Eds. Berlin, Heidelberg: Springer Berlin Heidelberg, 2014, pp. 131–161.
- [104] P. Gangadharan, K. C. Kanchi, and H. H. Lou, “Evaluation of the economic and environmental impact of combining dry reforming with steam reforming of methane,” *Chem. Eng. Res. Des.*, vol. 90, no. 11, pp. 1956–1968, 2012.
- [105] Y. Zhang, S. Zhang, H. H. Lou, J. L. Gossage, and T. J. Benson, “Steam and dry reforming processes coupled with partial oxidation of methane for CO₂ emission reduction,” *Chem. Eng. Technol.*, vol. 37, no. 9, pp. 1493–1499, 2014.
- [106] D. Treacy and J. R. H. Ross, “The Potential of the CO₂ reforming of CH₄ as a method of CO₂ mitigation. A thermodynamic study,” *Prepr. Pap.-Am. Chem. Soc., Div. Fuel Chem.*, vol. 49, no. 1, pp. 126–127, 2004.
- [107] H. Er-rbib, C. Bouallou, and F. Werkoff, “Production of synthetic gasoline and diesel fuel from dry reforming of methane,” *Energy Procedia*, vol. 29, pp. 156–165, 2012.
- [108] X. Tao *et al.*, “CH₄-CO₂ reforming by plasma - Challenges and opportunities,” *Prog. Energy Combust. Sci.*, vol. 37, no. 2, pp. 113–124, 2011.
- [109] D. J. Roddy, Dermot J. Roddy, D. J. Roddy, and Dermot J. Roddy, “A syngas network for reducing industrial carbon footprint and energy use,” *Appl. Therm. Eng.*, vol. 53, no. 2, pp. 299–304, 2013.
- [110] J. Martínez-Gomez, F. Nápoles-rivera, J. M. J. M. Ponce-Ortega, and M. M. M. M. M. El-Halwagi, “Optimization of the production of syngas from shale gas with economic and safety

- considerations,” *Appl. Therm. Eng.*, vol. 110, pp. 678–685, 2017.
- [111] M. M. B. Noureldin, N. O. Elbashir, K. J. Gabriel, and M. M. El-Halwagi, “A process integration approach to the assessment of CO₂ fixation through dry reforming,” *ACS Sustain. Chem. Eng.*, vol. 3, no. 4, pp. 625–636, 2015.
- [112] M. S. Challiwala, M. M. Ghouri, P. Linke, M. M. El-Halwagi, and N. O. Elbashir, “A combined thermo-kinetic analysis of various methane reforming technologies: Comparison with dry reforming,” *J. CO₂ Util.*, vol. 17, pp. 99–111, 2017.
- [113] I. Dybkjær and K. Aasberg-Petersen, “Synthesis Gas Technology Large-Scale Applications,” *Can. J. Chem. Eng.*, vol. 94, no. 4, pp. 607–612, 2016.
- [114] O. Yamazaki, K. Tomishige, and K. Fujimoto, “Development of highly stable nickel catalyst for methane-steam reaction under low steam to carbon ratio,” *Appl. Catal. A Gen.*, vol. 136, no. 1, pp. 49–56, 1996.
- [115] L. Basini and L. Piovesan, “Reduction on Synthesis Gas Costs by Decrease of Steam/Carbon and Oxygen/Carbon Ratios in the Feedstock,” *Ind. Eng. Chem. Res.*, vol. 37, no. 1, pp. 258–266, 1998.
- [116] C. C. D. US EPA, “Glossary of Climate Change Terms.” [Online]. Available: <https://www3.epa.gov/climatechange/glossary.html#G>. [Accessed: 26-Sep-2017].
- [117] G. Myhre *et al.*, “Anthropogenic and Natural Radiative Forcing,” *Clim. Chang. 2013 Phys. Sci. Basis. Contrib. Work. Gr. I to Fifth Assess. Rep. Intergov. Panel Clim. Chang.*, vol. 9781107057, pp. 659–740, 2013.
- [118] Union Gas, “Chemical Composition of Natural Gas - Union Gas.” [Online]. Available: <https://www.uniongas.com/about-us/about-natural-gas/Chemical-Composition-of-Natural-Gas>. [Accessed: 26-Sep-2017].
- [119] X. D. Peng, “Analysis of the Thermal Efficiency Limit of the Steam Methane Reforming Process,” *Ind. Eng. Chem. Res.*, vol. 51, pp. 16385–16392, 2012.
- [120] J. David and H. Herzog, “THE COST OF CARBON CAPTURE,” *Energy*, pp. 13–16, 2000.
- [121] J. Rostrup-Nielsen and L. J. Christiansen, *CATALYTIC SCIENCE SERIES : CONCEPTS IN SYNGAS MANUFACTURE, Volume 9*. Singapore, US, US: Imperial College Press, 2011.
- [122] B. Agarski *et al.*, “Comparative life cycle assessment of Ni-based catalyst synthesis processes,” *J. Clean. Prod.*, vol. 162, pp. 7–15, Sep. 2017.

- [123] M. M. B. B. Noureldin, N. O. Elbashir, and M. M. El-Halwagi, "Optimization and selection of reforming approaches for syngas generation from natural/shale gas," *Ind. Eng. Chem. Res.*, vol. 53, no. 5, pp. 1841–1855, 2014.
- [124] M. J. Smith, H. C. Van Ness, and M. M. Abbott, *Introduction to Chemical Engineering Thermodynamics*. Mc-Graw Hill, 2001.
- [125] P. M. Mortensen and I. Dybkjær, "Industrial scale experience on steam reforming of CO₂-rich gas," *Appl. Catal. A Gen.*, vol. 495, pp. 141–151, 2015.
- [126] "Thermodynamic Package Standard Inc.," *TPSI Fifteen Fluids*. [Online]. Available: http://www.tpsi.us/TPSI_WebPage_InitPlaceholder.htm.
- [127] M. M. El-Halwagi, *Sustainable design through process integration : fundamentals and applications to industrial pollution prevention, resource conservation, and profitability enhancement*. Butterworth-Heinemann, 2012.
- [128] "U.S. Energy Information Administration (EIA) - Data," 2017. [Online]. Available: <https://www.eia.gov/naturalgas/data.php#prices>. [Accessed: 20-Jun-2017].
- [129] "Calculator: Steam Unit Cost | TLV - A Steam Specialist Company (International)." [Online]. Available: <http://www.tlv.com/global/TLV/calculator/steam-unit-cost.html>. [Accessed: 20-Jun-2017].
- [130] Shailesh Vora *et al.*, "DOE/NETL Advanced Carbon Dioxide Capture R&D Program : Technology Update," 2013.
- [131] K. M. R. Al-Hitmi, "QAFAC: carbon dioxide recovery plant," *Sustain. Technol. Syst. Policies*, vol. 22, no. April, pp. 2012–2014, 2012.
- [132] D. J. Haase, P. M. Duke, and J. W. Cates, "CO recovery and purification," *Hydrocarbon Processing*, vol. 61, no. 3, pp. 103–107, 1982.
- [133] N. N. N. Dutta and G. S. S. Patil, "Developments in CO separation," *Gas Sep. Purif.*, vol. 9, no. 4, pp. 277–283, 1995.
- [134] A. Kohl and R. B. Nielsen, "Miscellaneous Gas Purification Techniques," *Gas Purif.*, pp. 1296–1373, 1997.
- [135] A. Keller and R. Schendel, "The Use of COSORB II to recover High-Purity Carbon Monoxide from a Feed Gas," in *AIChE Summer Meeting*, 1988, pp. 1–9.
- [136] "Jmol: an open-source Java viewer for chemical structures in 3D." [Online]. Available: <http://www.jmol.org/>.

- [137] D. J. Haase, "New solvent cuts costs of carbon monoxide recovery," *Chemical Engineering*, pp. 52–54, Aug-1975.
- [138] D. G. Walker, "Carbon Monoxide as a Fuel," *166th Natl. Meet. Am. Chem. Soc. Div. Fuel Chem.*, pp. 78–83, 1973.
- [139] I. Glasgow, "(53an) Economics of Hydrogen Purification in an Ethylene Plant | AIChE Academy," in *2017 Spring Meeting and 13th Global Congress on Process Safety*, 2017.
- [140] H. H. Gunardson and J. M. Abrardo, "Produce CO-rich synthesis gas," *Hydrocarb. Process.*, vol. 78, no. 4, pp. 87–92, 1999.
- [141] S. (Texas A. U. Afzal, "Modeling Fischer-Tropsch Product Distribution of a cobalt based catalyst in Different Reaction Media," Texas A&M University, 2015.
- [142] H. M. Torres Galvis and K. P. De Jong, "Catalysts for Production of Lower Olefins from Synthesis Gas: A Review," *ACS Catal.*, vol. 3, pp. 2130–2149, 2013.
- [143] M. M. El-Halwagi and M. M. El-Halwagi, "Benchmarking Process Performance Through Overall Mass Targeting Benchmarking," *Sustain. Des. Through Process Integr.*, pp. 63–88, 2012.
- [144] L. C. Buelens, V. V Galvita, H. Poelman, C. Detavernier, and G. B. Marin, "Super-dry reforming of methane intensifies CO₂ utilization via Le Chatelier's principle," *Science (80-.)*, vol. 354, no. 6311, pp. 449–453, 2016.
- [145] N. Elbashir, S. Afzal, M. El-Halwagi, and D. Sengupta, "Processing methane for syngas Production with reduced CO₂ emissions," WO 2019/194694 A2.
- [146] M. M. El-Halwagi, "A Shortcut Approach to the Multi-scale Atomic Targeting and Design of C–H–O Symbiosis Networks," *Process Integr. Optim. Sustain.*, vol. 1, no. 1, pp. 3–13, Jan. 2017.
- [147] M. M. B. Noureldin and M. M. El-Halwagi, "Synthesis of C-H-O Symbiosis Networks Mohamed," *AIChE J.*, vol. 61, no. 4, pp. 1242–1262, Apr. 2015.
- [148] D. M. Al-Mohannadi and P. Linke, "On the systematic carbon integration of industrial parks for climate footprint reduction," *J. Clean. Prod.*, vol. 112, pp. 4053–4064, Jan. 2016.
- [149] "UW Madison Geology 777 - Vacuum Systems." [Online]. Available: <https://slideplayer.com/slide/17482754/>.
- [150] B. Jenninger and P. Chiggiato, "CAS tutorial on RGA Interpretation of RGA spectra." [Online]. Available: https://indico.cern.ch/event/565314/contributions/2285748/attachments/1467497/2273709/RGA_tutorial-interpretation.pdf. [Accessed: 11-Jun-2018].

- [151] O. B. Malyshev and K. J. Middleman, “*In situ* ultrahigh vacuum residual gas analyzer ‘calibration,’” *J. Vac. Sci. Technol. A Vacuum, Surfaces, Film.*, vol. 26, no. 6, pp. 1474–1479, 2008.
- [152] C. R. Tilford, “Process monitoring with residual gas analysers (RGAs): limiting factors,” *Surf. Coatings Technol.*, vol. 68/69, p. 708, 1994.

APPENDIX A
RGA SETUP, MS AND GC CALIBRATION

This section described the Residual Gas Analyzer setup and the method used to calibrate the Mass Spectrometer. It is called ‘residual’ since it can detect ppm level of gases. There is a vacuum chamber in the RGA, as shown in Figure 57 [149] where the gases are ionized and their partial pressures are shown on the screen. The ion detector separates the ions based on the mass-to-charge ratio (m/z).



Figure 57 - Residual Gas Analyzer. Reprinted from [149]

There are three main components in both types of RGAs:

- an ion source - turns molecules into ions
- a mass analyzer - ions are sorted out according to mass by the mass analyzer, which does so by employing electric and magnetic fields
- detector - calculates the mass-to-charge ratio

The final display of data is referred to as a mass scan or a mass spectrum. From experience of using the RGA, it is important to keep moisture content going into the RGA at a minimum. If a lot of water gets into the RGA, it takes almost a day to dry the RGA until the readings normalize back to normal.

In-situ Calibration to get RS factors

Each gas has a Relative Sensitivity (RS) factor. The partial pressure of each gas has to be converted using the RS factor before the % composition can be calculated. Using RGA for quantification of gas mixtures requires frequent calibration prior to each experiment. This is also seen in studies relating to RGA [150]–[152] where it has been suggested that the drift in the relative sensitivities of gases in the

RGA means that in-situ calibration is a must if quantitative analysis is desired. The method of calibration is described in Figure 58.

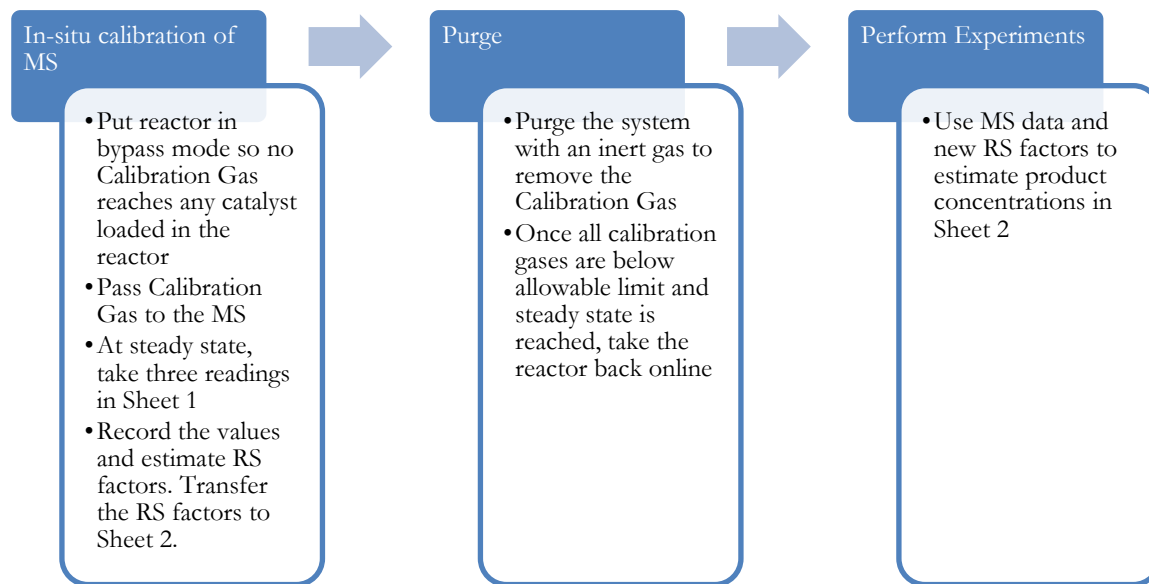


Figure 58 - Suggested workflow for using Mass Spec in experiments

One-point calibration is performed using calibration gas (10% CH₄, 10% CO₂, 10% H₂, 10% CO, 2% Ar, 58% He). After stabilization of RGA partial pressure values, three values are taken at intervals of approx. 10 min. Then, the Relative Sensitivity (RS) of each gas is calculated using the following equation:

$$RS_i = \frac{PP_i}{\%_i} \times \frac{\%_{Ar}}{PP_{Ar}} \quad \text{Eq (A1)}$$

PP_i → Partial Pressure of Gas i in Torr

$\%_i$ → Known Concentration of Gas i used

After calibration, DRM gas (10% CH₄, 10% CO₂, 2% Ar, 78% He) is passed through the RGA to get accurate inlet gas composition. The readings are collected in reactor-bypass mode to avoid any adsorption, etc. affecting the response. Once the partial pressure signals have stabilized, the values are recorded and the composition of the DRM inlet gas is quantified via Eq (A2). This completes the calibration procedure, and the last recorded calibration values are used for data analysis. During an

experimental run, the partial pressure values of each gas are recorded, and the data analysis is performed per the procedure below:

The %_{*i*} of each gas is calculated based on the following equation:

$$\%_i = \frac{\left(\frac{PP_i}{RS_i}\right)}{\sum_1^n \left(\frac{PP_i}{RS_i}\right)} \times 100 \quad \text{Eq (A2)}$$

Since Argon (2%) is the internal standard in the DRM gas mixture, the relation can be used as the basis for quantification:

$$\text{Moles Argon In} = \text{Moles Argon Out}$$

The outlet STP flowrate is thus calculated from:

$$(0.02) \times F^{\text{inlet, STP}} = (\%_{Ar}) \times F^{\text{outlet, STP}} \quad \text{Eq (A3)}$$

Based on RGA data, STP flows of all other gases can be calculated by:

$$F_i^{\text{outlet, STP}} = (i\%) \times F^{\text{outlet, STP}} \quad \text{Eq (A4)}$$

In this way, Conversion and Rate of Reaction can be calculated:

$$\text{Conversion, } X_{CH_4} = \left(\frac{F_{CH_4}^{\text{inlet, STP}} - F_{CH_4}^{\text{outlet, STP}}}{F_{CH_4}^{\text{inlet, STP}}} \right) \times 100 \quad \text{Eq (A5)}$$

$$\text{Rate of Reaction, } r_{CH_4} = \left(\frac{F_{CH_4}^{\text{inlet, STP}} - F_{CH_4}^{\text{outlet, STP}}}{22,414 \times m_{cat}} \right) \times 1000, \left(\frac{\text{mol}}{\text{min.g}_{cat}} \right) \quad \text{Eq (A6)}$$

The reliability check is done by calculating mole balance over entire system boundary using the following equation:

$$\text{Carbon Error}\% = \left(\frac{F_{CH_4}^{\text{inlet, STP}} + F_{CO_2}^{\text{inlet, STP}} - F_{CH_4}^{\text{outlet, STP}} - F_{CO_2}^{\text{outlet, STP}} - F_{CO}^{\text{outlet, STP}}}{F_{CH_4}^{\text{inlet, STP}} + F_{CO_2}^{\text{inlet, STP}}} \right) \times 100 \quad \text{Eq (A7)}$$

$$\text{Helium Error}\% = \left(\frac{F_{He}^{\text{inlet, STP}} - F_{He}^{\text{outlet, STP}}}{F_{He}^{\text{inlet, STP}}} \right) \times 100 \quad \text{Eq (A8)}$$

Since Helium is another inert apart from Argon, it serves as a reliability check on the quality of calculated data. The error values should be reasonably low and well within empirical error limits. Most of the errors for both Carbon and Helium are less than 5%, with only one run giving an error of ~10%. The coke formation rate should not be estimated from this carbon balance, as coke formation rates are much lower than the tolerance limits of our quantification system. Hence, only TPO data will be a reliable measure of the amount of coke formed.

NB: Although water is condensed using the liquid trap, we observe little to no condensation, which is probably due to liquid carryover. Nonetheless, quantification of water is not performed.

GC Calibration and Data Analysis

Data Analysis using a GC is more straight forward than an RGA. In a Gas Chromatograph, calibration for Peak Area (PA) of gases v/s their Mole Flows was done at different flowrates using Argon as Internal Standard. A typical calibration chart is shown in Figure 59.

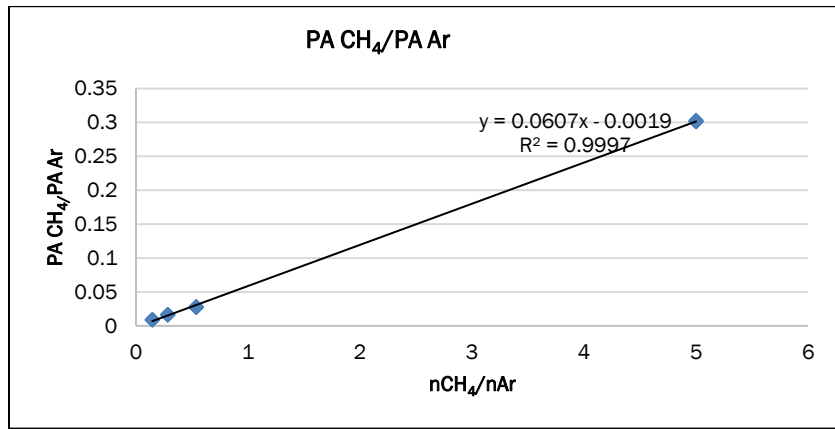


Figure 59 - Typical Calibration Chart for PA ratio v/s Molar ratio

For each run, specific equations to obtain n_i (number of moles of gas i flowing out) are used to calculate amount of particular gas flowing out. Number of moles flowing in is obtained from MFC. Hence, conversion and reaction rates can be calculated on a molar basis.

$$\text{Conversion, } X_{CH_4} = \left(\frac{n_{CH_4}^{inlet, STP} - n_{CH_4}^{outlet, STP}}{n_{CH_4}^{inlet, STP}} \right) \times 100 \quad \text{Eq(A9)}$$

$$\text{Rate of Reaction, } r_{CH_4} = \left(\frac{n_{CH_4}^{inlet, STP} - n_{CH_4}^{outlet, STP}}{m_{cat}} \right) \times 1000, \left(\frac{mol}{min.g_{cat}} \right) \quad \text{Eq(A10)}$$

APPENDIX B

EFFECT OF DILUENT SAND ON CATALYTIC ACTIVITY

Figure 60 illustrates the setup of the Micro-Activity Reactor at TAMUQ. The reactor is enclosed in a hot box. The outlet gases are connected to a cold trap maintained at 4 °C to condense the water. The outlet gases can be analyzed in both the GC and the RGA. The GC and RGA cannot be operated simultaneously as the vacuum draw of RGA will prevent gas flow to the GC inlet line.

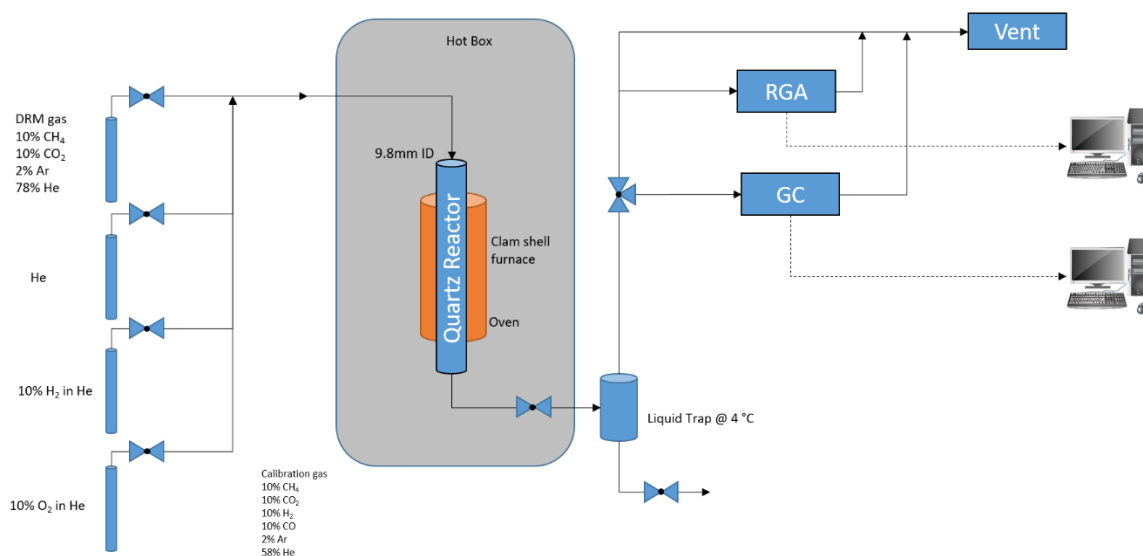


Figure 60 - Experimental Setup

Several runs comparing the calculated conversions from both GC and RGA were carried out. During a test, the outlet gas of the reactor is switched between the RGA and GC at regular intervals to monitor variation in conversion with varying flow rates. As mentioned previously, the strong vacuum created by the RGA pump prevents simultaneous exit gas measurement by GC and RGA. The RGA and GC trend very similarly.

Results of Short Time on Stream Runs

To finalize the operating conditions for kinetic investigations as well as future experimental campaigns, we performed short TOS tests (1-2 h for each flow-rate) with varying amounts of catalyst, dilution

ratios, particle sizes as shown in Table 19. All tests were performed with 20% Ni/Al₂O₃ (Riogen) and at 650 °C.

Table 19 - Details of short TOS runs

| Amount of catalyst (mg) | Amount of diluent sand (mg) | Particle Size (µm) | Flowrates of DRM gas (mNi/min – in steps of 30) |
|--------------------------------|------------------------------------|---------------------------|--|
| 10 | 250 | 75-150 | 30-150 |
| 5 | 250 | 75-150 | 30-150 |
| 2.5 | 250 | 75-150 | 30-150 |
| 5 | 500 | 75-150 | 30-150 |
| 2.5 | 100 | 75-150 | 30-120 |
| 2.5 | 25 | 75-150 | 30-150 |
| 5 | 25 | 75-150 | 30-240 |
| 2.5 | 0 | 75-150 | 30-240 |
| 2.5 | 25 | <53 | 30-240 |

A typical run with the data analysis is shown in Figure 61. The simple average values of conversion and reaction rates for each flow-rate were used for analysis, described later.

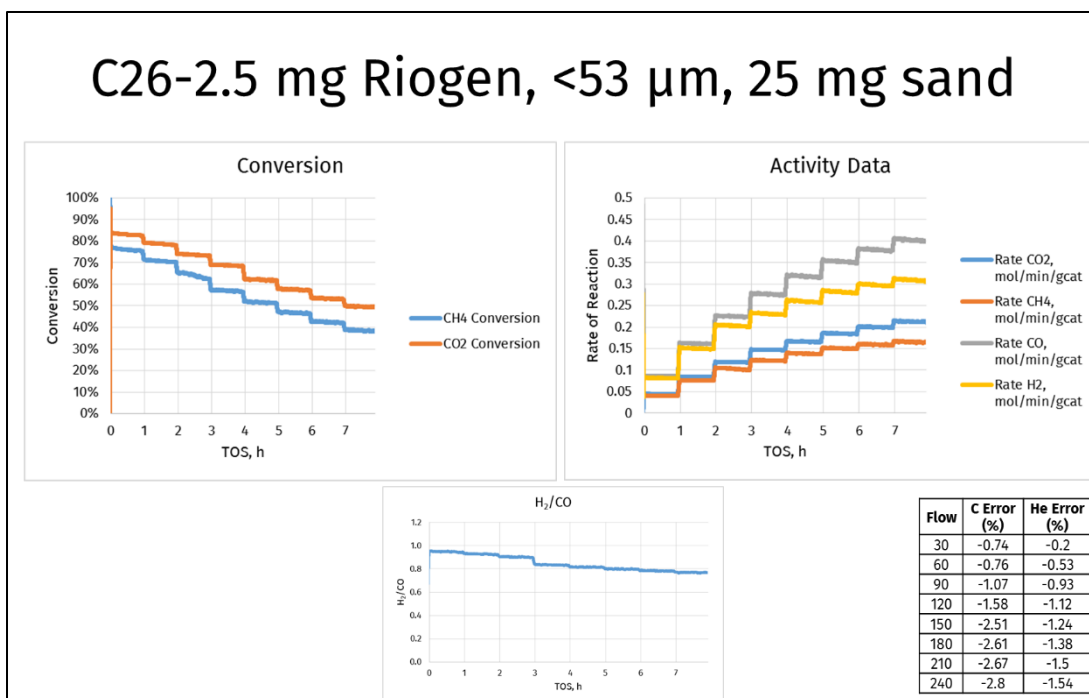


Figure 61 - Data Analysis for 2.5 mg Riogen, 25 mg sand, <53 μm range

For the kinetic experiments, the goal is to estimate the intrinsic reaction rate in the absence of external and internal mass transfer limitations. To achieve this, the reaction rate must not be affected by any other parameter other than those that affect the kinetic rate.

External Mass Transfer Limitation

A large dilution ratio of 5 mg catalyst dispersed in 500 mg sand was chosen as the starting point. As shown in Figure 62 and Figure 63, the reaction rates for CH_4 were very low. When the same amount of catalyst was diluted with 250 mg sand, the activity improved indicating that the diluent was restricting access of reactant gases to the active sites. Different amounts of catalyst (2.5 mg, 5 mg, and 10 mg) with 250 mg catalyst yielded vastly different results, indicating that the 250 mg sand was still limiting. Decreasing the dilution even further to 25 mg provided the most adequate rates thus far while maintaining a minimum acceptable catalyst and sand loading.

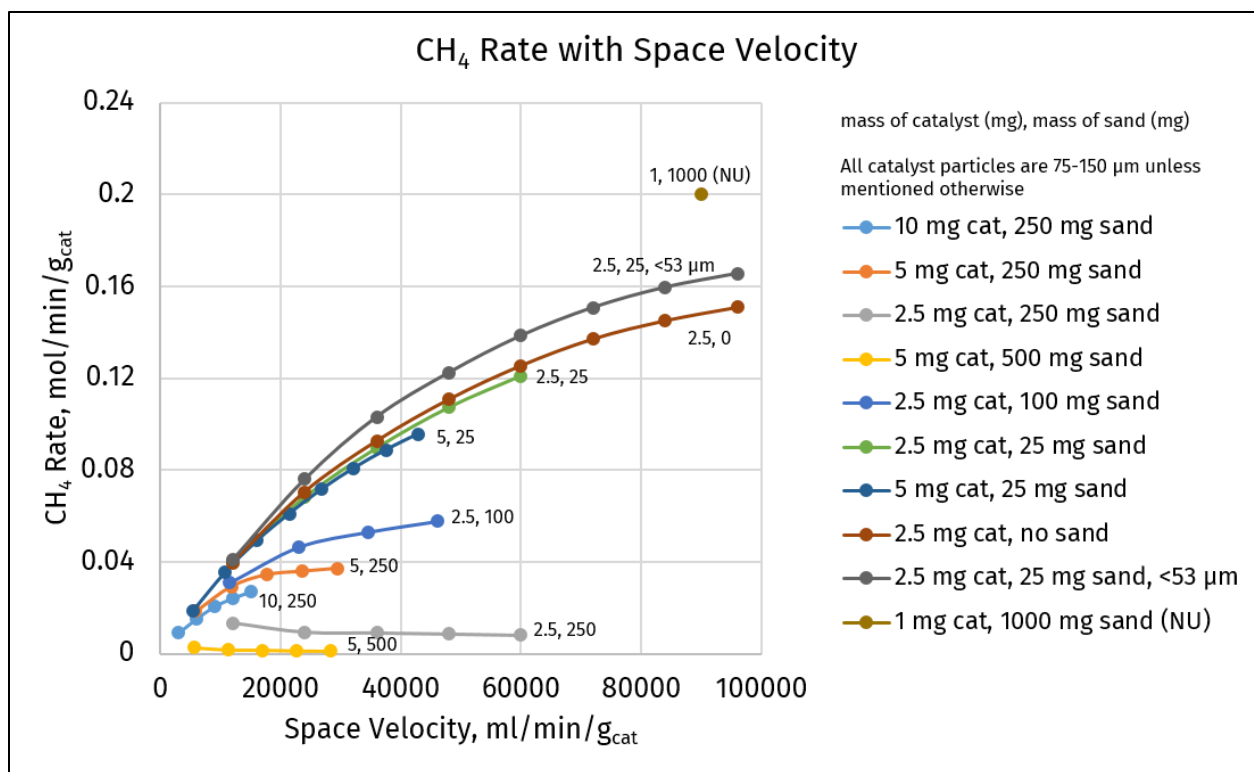


Figure 62 - CH₄ rate with Space Velocity (ml/min/g_{cat})

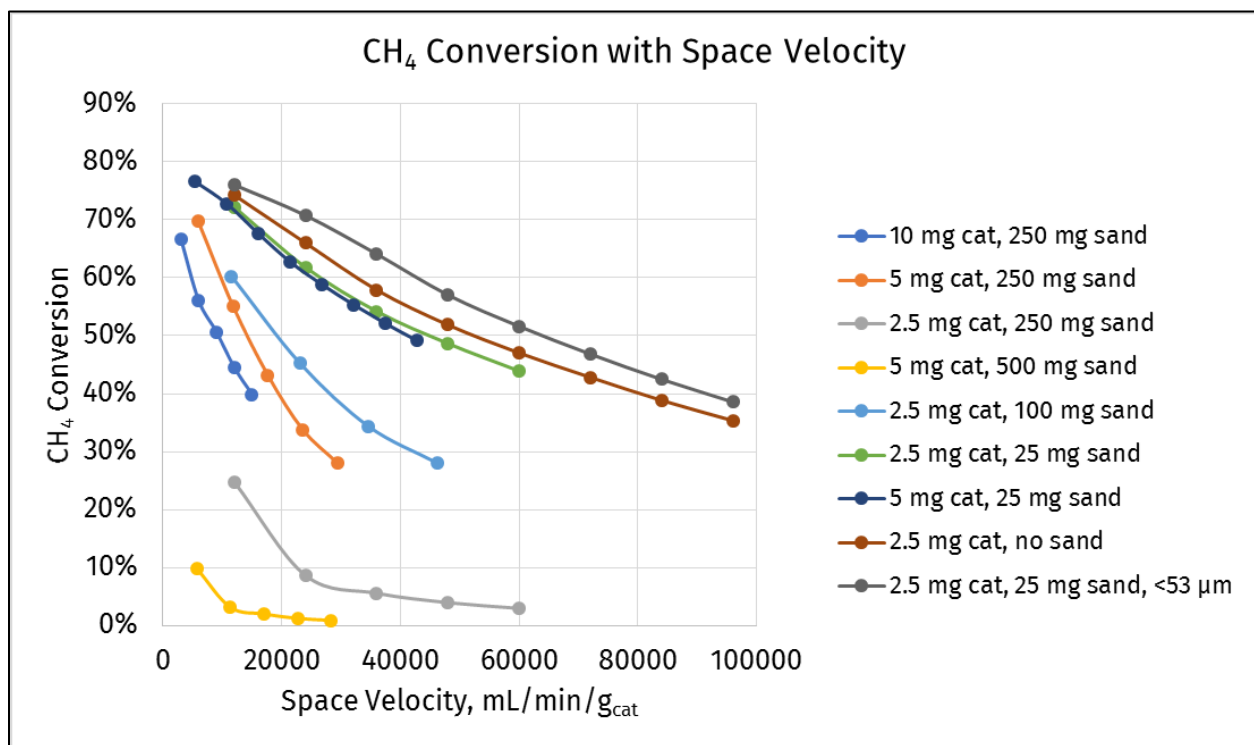


Figure 63 - CH₄ Conversion with Space Velocity (ml/min/g_{cat})

Internal Mass Transfer Limitation

To check for internal mass transfer limitations within the pores of the catalyst (intra-particle diffusion), the smallest sieved particle fraction (<53 μm) was used. As shown in Figure 62 and Figure 63, the performance is slightly improved indicating that the 75-150 micron range is still suitable for catalyst performance despite the minor intra-particle diffusion effects on the rate. Nevertheless, the < 53 μm fraction will be considered for the kinetic tests.

Calculation of Reaction Rate

From Figures 4 and 5, it is clear that even when using 2.5 mg of the smallest particle fraction (<53 μm) diluted in 25 mg sand and at the maximum flow rate possible (240 mL/min), a relatively high CH_4 conversion of $\sim 40\%$ was obtained. However, for developing kinetics, conversions need to be kept low enough, ideally, 10% and below in order to use Equation (A10) to calculate intrinsic rate. To account for this, we have modified the rate calculation method as follows:

Assuming PFR flow, we have the following equation:

$$(-r_A) = F_{A0} \frac{dX}{dW} \quad \text{Eq (A11)}$$

Instead of the conventional 'in-out' calculation for reaction rate, generate a plot of X vs. W/F_{A0} and apply the differential method of analysis for PFR (or 'PBR,' Packed Bed Reactor). For a fixed feed composition, W/F_{A0} (inverse of space velocity) is varied to obtain X . Subsequently, through curve fitting, a simple polynomial will fit the data of X vs W/F_{A0} . This will make it easy to just differentiate the equation to get reaction rate at required points. Moreover, since the experiments will be conducted at 500 $^\circ\text{C}$ and 550 $^\circ\text{C}$, we expect conversions to drop down to close to 10% or below, since there is a decrease of 100 $^\circ\text{C}$. And at low conversions, we would prefer to use the GC for quantification.

Proposed Operating Conditions based on Experimental Objective

For future experimental runs, conditions for DRM will be set depending on the expected research outcome of that specific campaign. They can be broadly classified into two campaigns: Performance testing and Kinetic studies and are described in Table 20.

Table 20 - Different Objectives, Different Conditions

| Performance Testing / Chemisorption Studies | Kinetic Testing |
|--|---|
| <ul style="list-style-type: none"> • Equilibrium conversion is an indicator of excess amount of catalyst for a given flow-rate and thus observing deactivation might be difficult for laboratory timescales. • Hence, stay away from equilibrium conditions • Using large amount of sand makes deactivation more evident | <ul style="list-style-type: none"> • Ensure external or internal mass transfer limitations have minimal effect on reaction rates |
| <p>Compare two catalytic systems at same conditions:</p> <ul style="list-style-type: none"> • Same particle size range • Same process conditions (T, P, Feed composition) • Space Velocity (moles of feed/unit time/mass of catalyst) • Same amount of nickel <p>NB: Amount of ALD catalyst will vary based on mass gain during ALD process, to keep Nickel % same during comparison</p> | |
| <p>Objective: Compare activity/deactivation/changes in crystallite size between uncoated and coated catalysts</p> | <p>Objective: Obtain reaction order, TOF, etc.</p> |
| <p>Outcome: Comment on coke formation rates (from TPO) and crystallite size changes (from chemisorption)</p> | <p>Outcome: Formulate kinetic model</p> |

Based on the results of the tests described in section 2, the conditions for future experimental campaigns are listed in Table 21 :

Table 21 - Operating Conditions for Future Testing

| Parameters | Performance comparison (ALD vs. non-coated) | | Kinetic investigations | Chemisorption studies |
|-------------------------------|---|---|---|---|
| | High initial activity, fast decline (a) | Lower activity, slow decline (b) | | |
| Mass of catalyst* | 5 mg | 2.5 mg | 2.5 mg | At least 10 mg |
| Catalyst particle size range | 75-150 μm | 75-150 μm | < 53 μm | 75-150 μm |
| Quantity of sand for dilution | 250 mg | 25 mg | 25 mg | 0 |
| Sand particle size range | 150-250 μm | 150-250 μm | 150-250 μm | N/A |
| DRM gas flow rate | 30 ml/min | 150 ml/min | 240 ml/min | 30 ml/min |
| Temperature(s) | 650 $^{\circ}\text{C}$ | 650 $^{\circ}\text{C}$ | 550, 600, 650 $^{\circ}\text{C}$ | 650 $^{\circ}\text{C}$ |
| DRM gas composition | 10:10:2:78 $\text{CH}_4:\text{CO}_2:\text{Ar}:\text{He}$ | | Variable, refer protocol | 10:10:2:78 $\text{CH}_4:\text{CO}_2:\text{Ar}:\text{He}$ |
| Comments | Expect moderate deactivation (due to 'diluent effect'), starting from equilibrium conversions | Expect ~50% CH_4 conversion due to higher flowrates and slow deactivation due to lesser diluent effect | Expect lower conversions than shown in this report at low temperature runs (550, 600 $^{\circ}\text{C}$) | Require at least 10 mg for reliable chemisorption results. Will most probably need to be increased to 30-50 mg range. |

| | | | | |
|--|-----------------------------------|--|--|--|
| | initially due to low flowrates | | | |
|--|-----------------------------------|--|--|--|

*Account for mass change due to ALD deposition process and change ALD catalyst mass accordingly

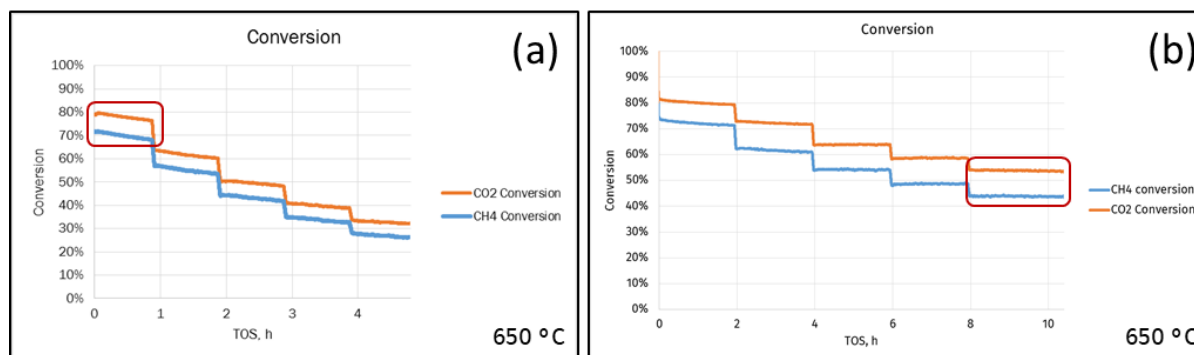


Figure 64 - Choosing the right conditions based on objective

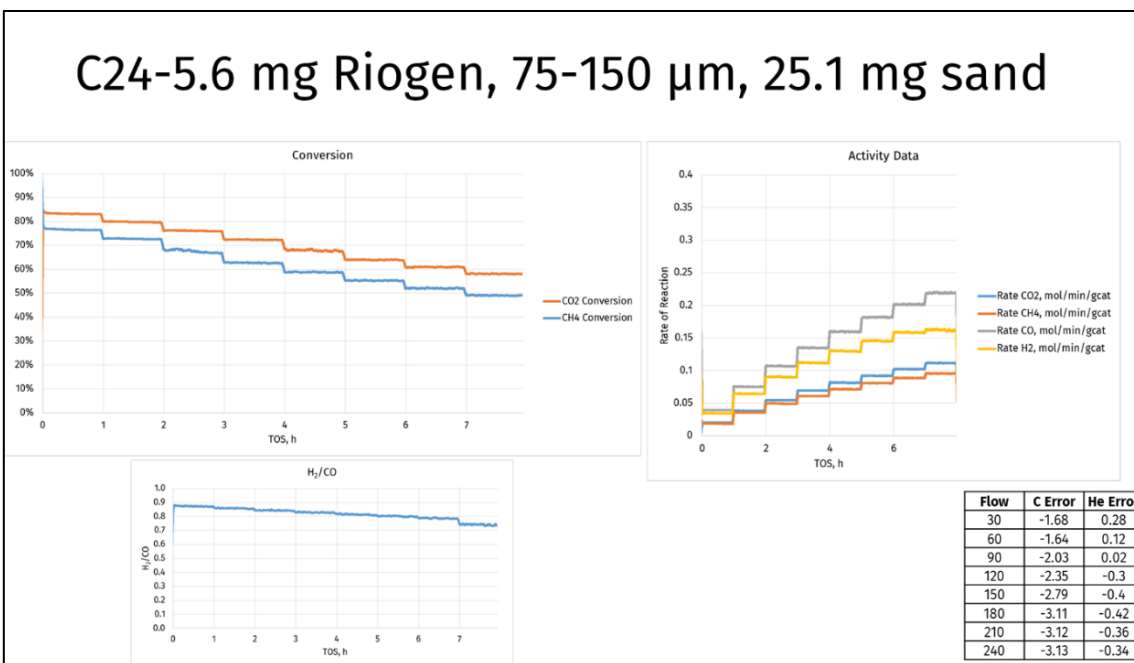
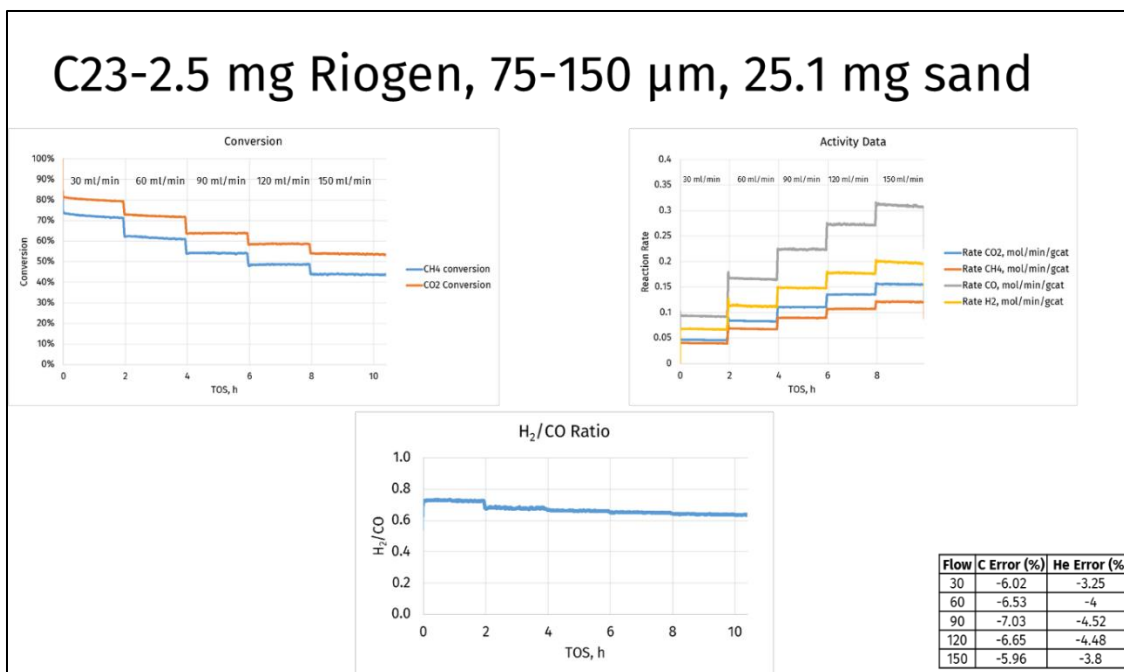
For the kinetic experiments, the following set of experiments are planned (Table 22). The objective is to investigate the effect of varying partial pressures of each of the gas species (CH_4 , CO_2 , H_2 , CO) on the reaction rate, and thereby formulate the kinetic model. For each fixed feed composition, once the curve of X_A v/s W/F_{A_0} is generated, reaction rate may be calculated using the slope of the curve (obtained from typical curve fitting). The origin (0,0) should give the initial reaction rate at the bed inlet.

Table 22 - Proposed set of kinetic experiments (more runs will be added as needed to vary the partial pressure span of species)

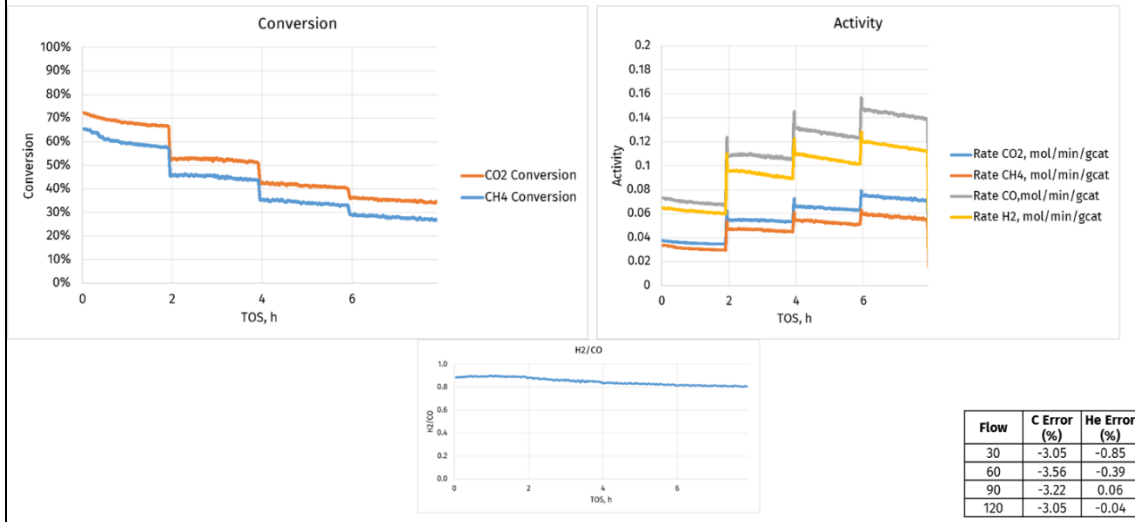
| Mole Fraction (feed) | | | | | Feed Ratios | | | | ONLY FILL UP CELLS BEOW THESE GREEN CELLS | | | | | | | | Total Flow | SV (Total flow basis) | | CH ₄ | | CO ₂ | |
|----------------------|-------------------|-------------------|------------------|--------------|-----------------|-----------------|----------------|-------------|---|------------------------|-------------------------|-------------|-------------------------|--------------------------|-------------|-------------|------------|-------------------------|--|-----------------------------|--|-----------------------------|--|
| T, °C | x-CH ₄ | x-CO ₂ | x-H ₂ | x-CO | CH ₄ | CO ₂ | H ₂ | CO | Calib Gas | Flow-rate, ml/min @STP | | | | | | | | ml/min/g _{cat} | W/F _{CH₄0} (g _{cat} -min/mol) | X _{CH₄} | W/F _{CO₂0} (g _{cat} -min/mol) | X _{CO₂} | |
| | | | | | | | | | | DRM gas | PURE H ₂ gas | PURE CO gas | 80% CH ₄ gas | PURE CO ₂ gas | PURE Ar gas | PURE He gas | | | | | | | |
| | | | | | | | | | | | | | | | | | | | | | | | |
| 550 | 0.083 | 0.083 | | | 1.00 | 1.00 | 0.00 | 0.00 | | 160 | | | | | | 32 | 192 | 76,800 | 3.5022 | | 3.5022 | | |
| 550 | 0.083 | 0.083 | | | 1.00 | 1.00 | 0.00 | 0.00 | | 200 | | | | | | 40 | 240 | 96,000 | 2.8018 | | 2.8018 | | |
| 550 | 0.083 | 0.083 | | | 1.00 | 1.00 | 0.00 | 0.00 | | 240 | | | | | | 50 | 290 | 116,000 | 2.3348 | | 2.3348 | | |
| 550 | 0.217 | 0.083 | | | 2.60 | 1.00 | 0.00 | 0.00 | | 160 | | | 32 | | | | 192 | 76,800 | 1.3470 | | 3.5022 | | |
| 550 | 0.217 | 0.083 | | | 2.60 | 1.00 | 0.00 | 0.00 | | 200 | | | 40 | | | | 240 | 96,000 | 1.0776 | | 2.8018 | | |
| 550 | 0.217 | 0.083 | | | 2.60 | 1.00 | 0.00 | 0.00 | | 240 | | | 48 | | | | 288 | 115,200 | 0.8980 | | 2.3348 | | |
| 550 | 0.085 | 0.213 | | | 1.00 | 2.50 | 0.00 | 0.00 | | 160 | | | | 24 | | 4 | 188 | 75,200 | 3.5022 | | 1.4009 | | |
| 550 | 0.083 | 0.217 | | | 1.00 | 2.60 | 0.00 | 0.00 | | 200 | | | | 32 | | 8 | 240 | 96,000 | 2.8018 | | 1.0776 | | |
| 550 | 0.082 | 0.219 | | | 1.00 | 2.67 | 0.00 | 0.00 | | 240 | | | | 40 | | 12 | 292 | 116,800 | 2.3348 | | 0.8755 | | |
| 550 | 0.083 | 0.083 | 0.083 | 0.083 | 1.00 | 1.00 | 1.00 | 1.00 | 160 | | | | | | | 32 | 192 | 76,800 | 3.5022 | | 3.5022 | | |
| 550 | 0.083 | 0.083 | 0.083 | 0.083 | 1.00 | 1.00 | 1.00 | 1.00 | 200 | | | | | | | 40 | 240 | 96,000 | 2.8018 | | 2.8018 | | |
| 550 | 0.083 | 0.083 | 0.083 | 0.083 | 1.00 | 1.00 | 1.00 | 1.00 | 240 | | | | | | | 48 | 288 | 115,200 | 2.3348 | | 2.3348 | | |
| 550 | 0.083 | 0.083 | 0.250 | 0.083 | 1.00 | 1.00 | 3.00 | 1.00 | 160 | | 32 | | | | | | 192 | 76,800 | 3.5022 | | 3.5022 | | |
| 550 | 0.083 | 0.083 | 0.250 | 0.083 | 1.00 | 1.00 | 3.00 | 1.00 | 200 | | 40 | | | | | | 240 | 96,000 | 2.8018 | | 2.8018 | | |
| 550 | 0.083 | 0.083 | 0.250 | 0.083 | 1.00 | 1.00 | 3.00 | 1.00 | 240 | | 48 | | | | | | 288 | 115,200 | 2.3348 | | 2.3348 | | |
| 550 | 0.083 | 0.083 | 0.083 | 0.250 | 1.00 | 1.00 | 1.00 | 3.00 | 160 | | | 32 | | | | | 192 | 76,800 | 3.5022 | | 3.5022 | | |
| 550 | 0.083 | 0.083 | 0.083 | 0.250 | 1.00 | 1.00 | 1.00 | 3.00 | 200 | | | 40 | | | | | 240 | 96,000 | 2.8018 | | 2.8018 | | |
| 550 | 0.083 | 0.083 | 0.083 | 0.250 | 1.00 | 1.00 | 1.00 | 3.00 | 240 | | | 48 | | | | | 288 | 115,200 | 2.3348 | | 2.3348 | | |

- The above table is only for 550 °C. The same shall be repeated for 600 and 650 °C.
- Only two levels of partial pressure have been considered here for each species, this will be increased to 3 levels of partial pressure.

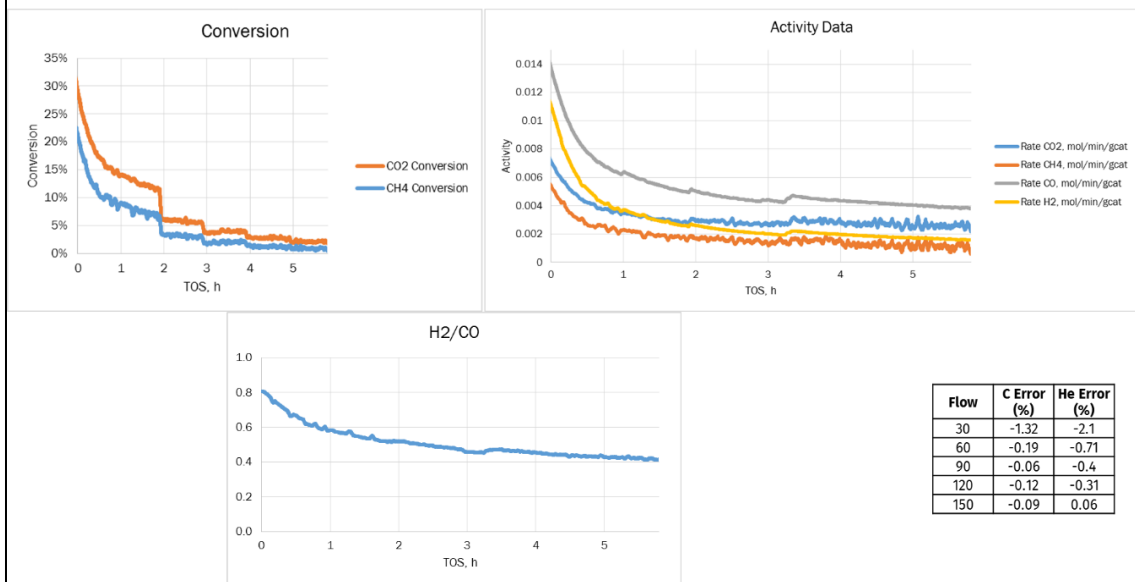
Experimental Results for varying catalyst weight and bed dilution



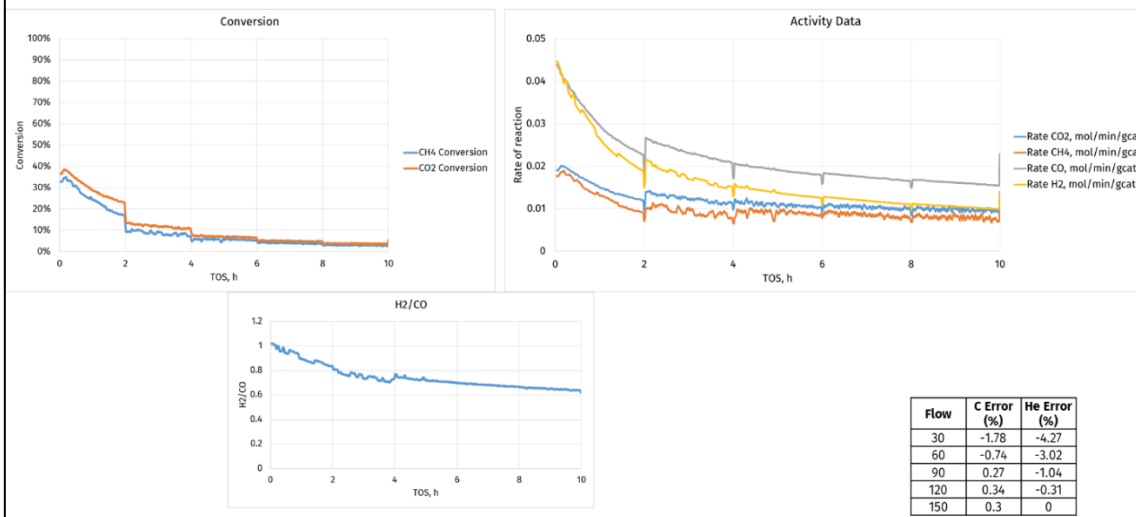
C21-2.6 mg Riogen, 75-150 μm , 100.3 mg sand



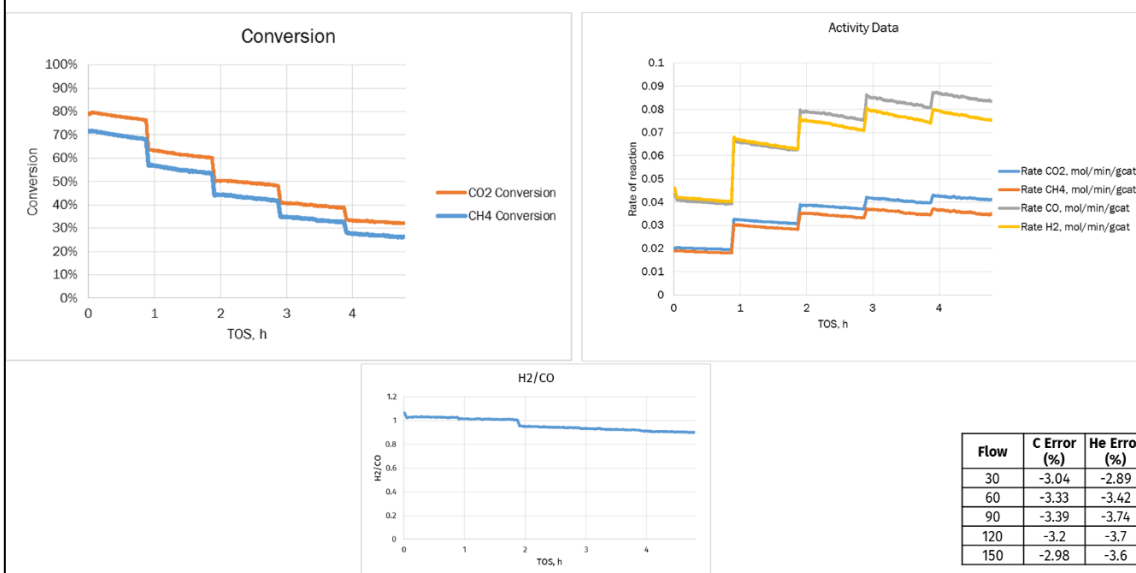
C19-5.3 mg Riogen, 75-150 μm , 500.5 mg sand



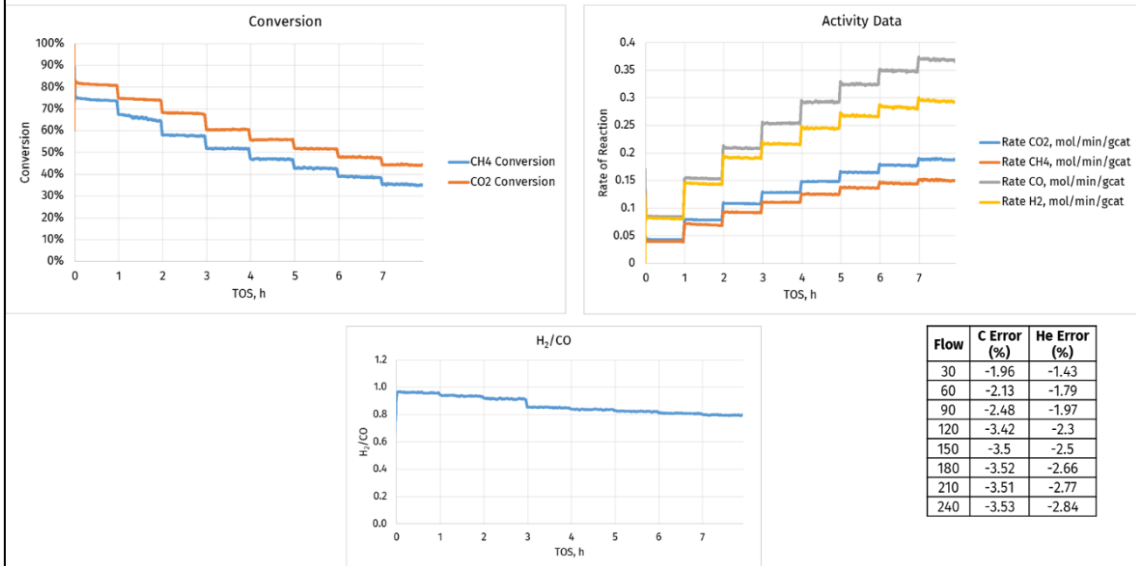
C18-2.5 mg Riogen, 75-150 μm , 250.7 mg sand



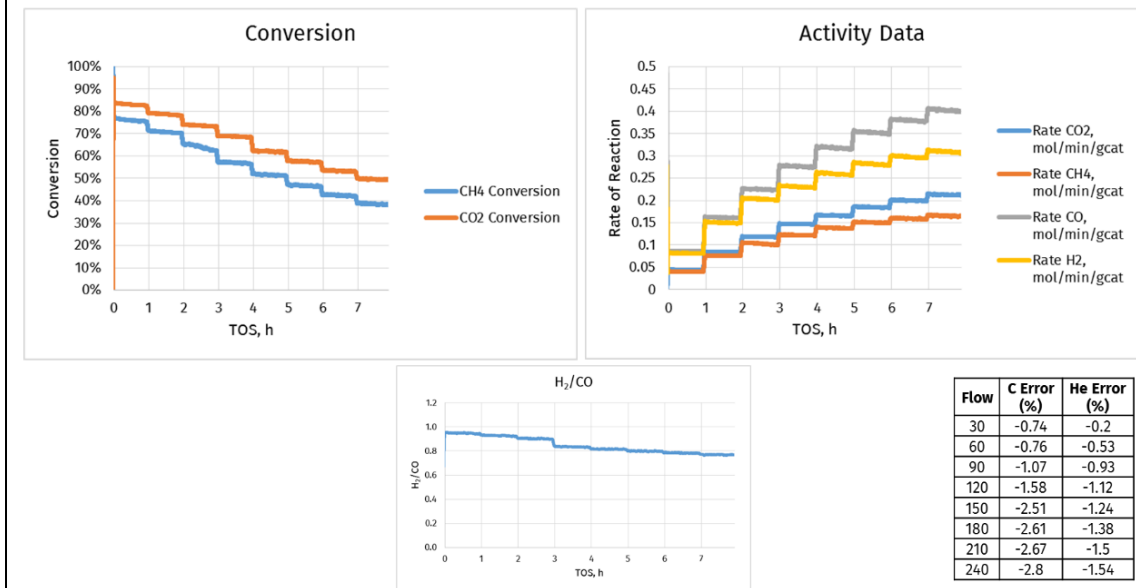
C17-5.1 mg Riogen, 75-150 μm , 250.8 mg sand



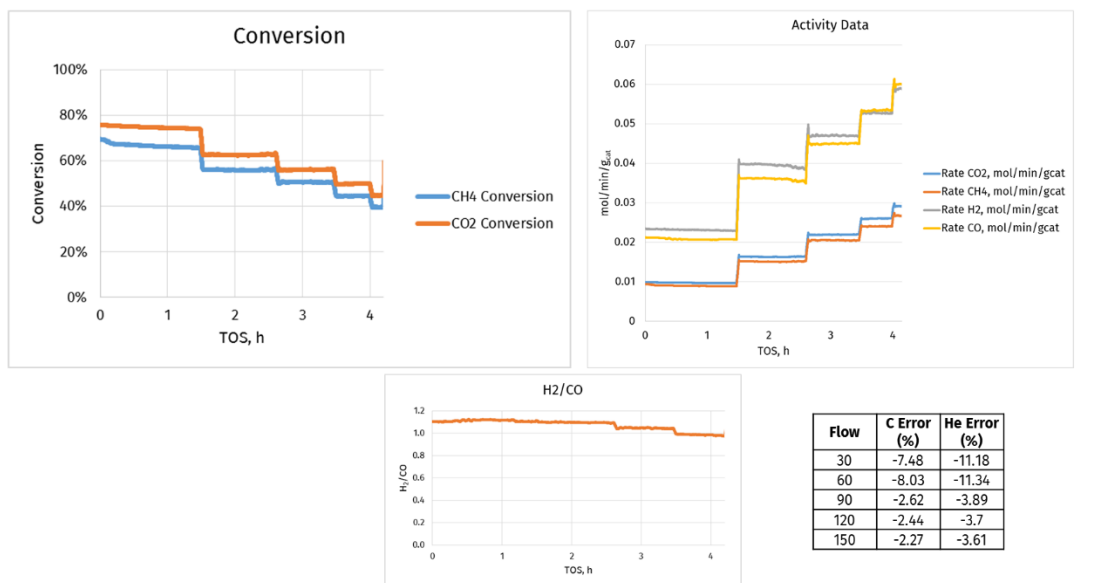
C25-2.5 mg Riogen, 75-150 μm , no sand

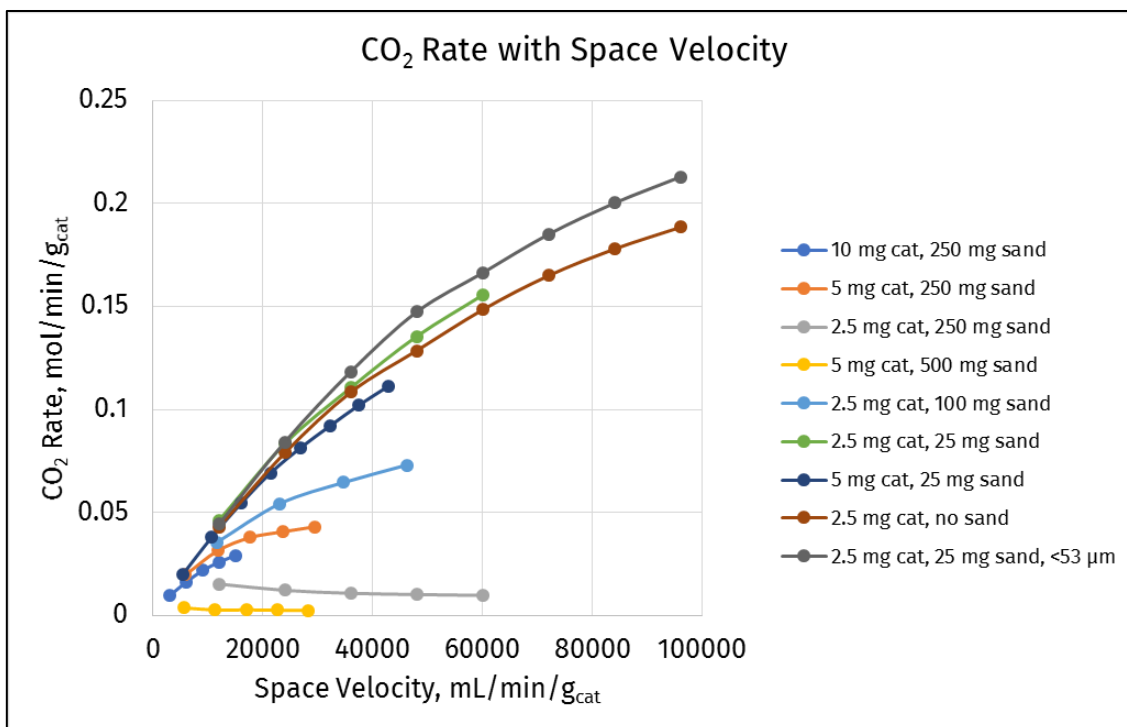
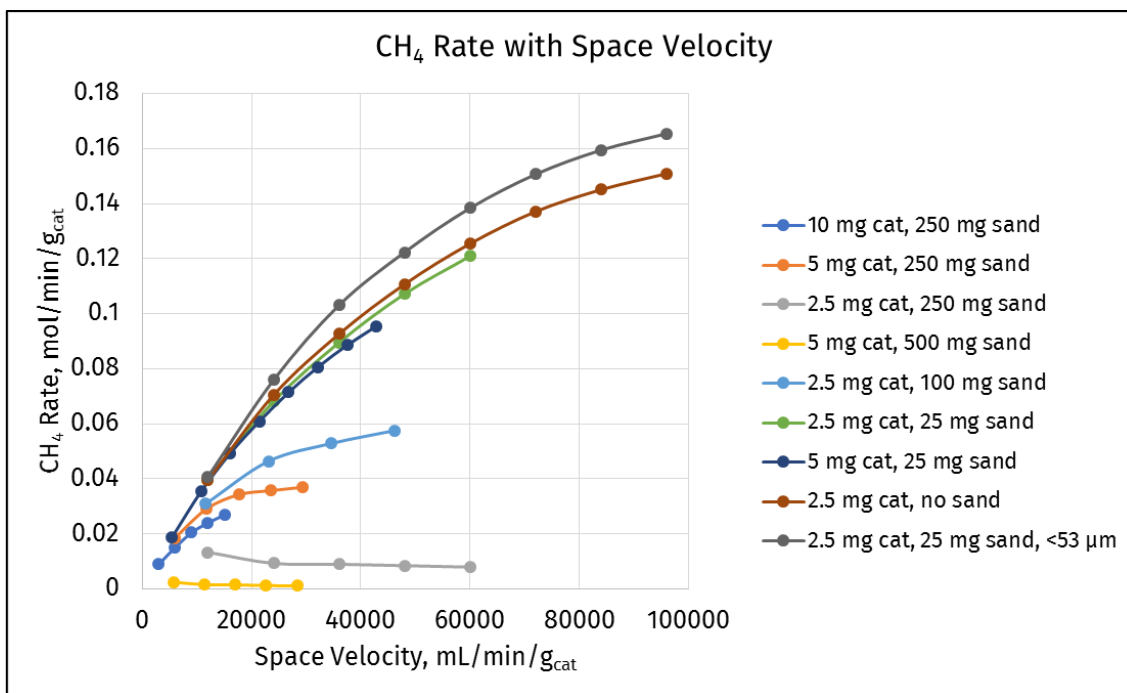


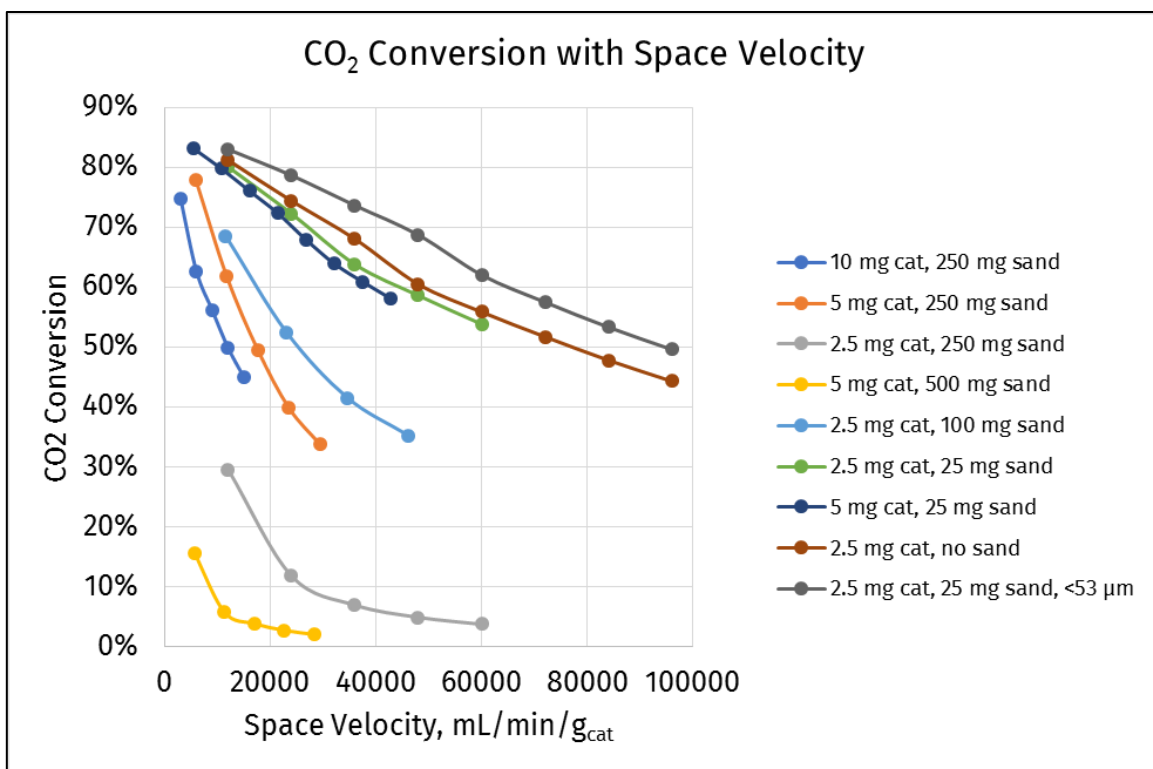
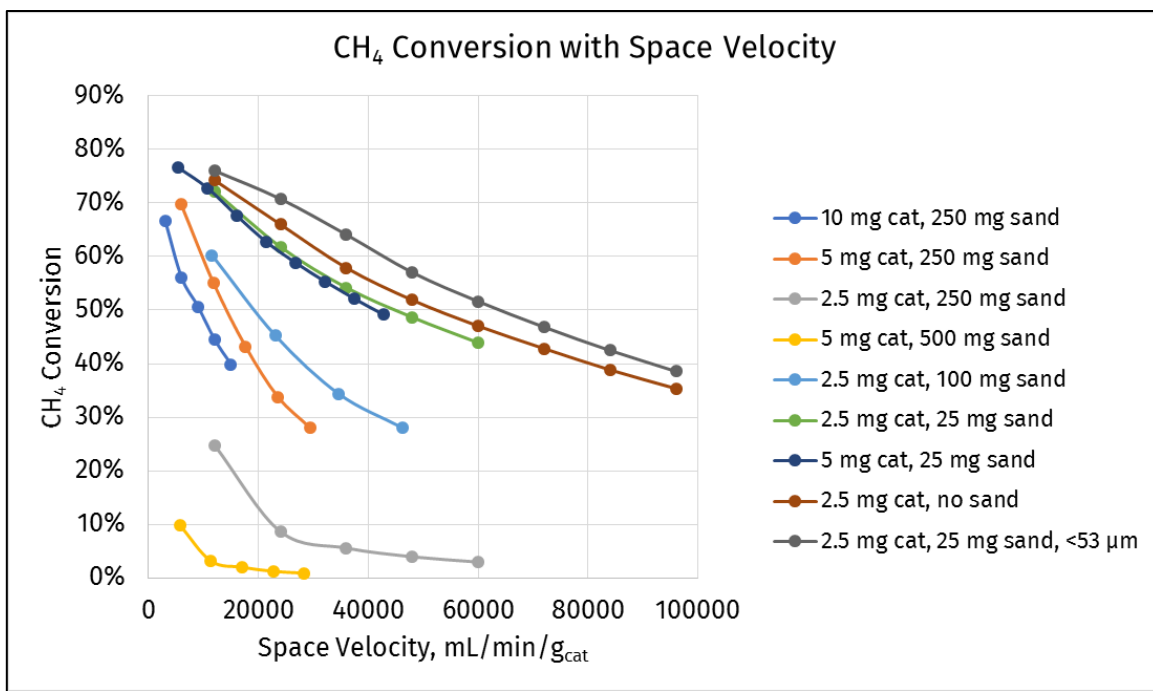
C26-2.5 mg Riogen, <53 μm , 25 mg sand



C16-10 mg Riogen, 75-150 μm , 250.2 mg sand







APPENDIX C

PATENT APPLICATION – PROCESSING METHANE FOR SYNGAS
PRODUCTION WITH REDUCED CO₂ EMISSIONS

(12) INTERNATIONAL APPLICATION PUBLISHED UNDER THE PATENT COOPERATION TREATY (PCT)

(19) World Intellectual Property
Organization
International Bureau



(10) International Publication Number
WO 2019/194694 A2

(43) International Publication Date
10 October 2019 (10.10.2019)

- (51) International Patent Classification: Not classified
- (21) International Application Number: PCT/QA2019/050008
- (22) International Filing Date: 03 April 2019 (03.04.2019)
- (25) Filing Language: English
- (26) Publication Language: English
- (30) Priority Data: 62/652,110 03 April 2018 (03.04.2018) US
- (71) Applicant: QATAR FOUNDATION [QA/QA]; P.O. Box 5825, Doha (QA).
- (72) Inventors: ELBASHIR, Nimir; c/o Texas A&M University at Qatar, Education City, 219 Chemical Engineering Program, P.O. Box 23874, Doha (QA). AFZAL, Shaik; c/o Texas A&M University at Qatar, Education City, 219 Chemical Engineering Program, P.O. Box 23874, Doha (QA). EL-HALWAGI, Mahmoud; CHEN Artie McFerrin Department of Chemical Eng., 3122 TAMU Room 200, College Station, Texas 77843 (US). SENGUPTA, Debali-na; CHEN Artie McFerrin Department of Chemical Eng., 3122 TAMU Room 200, College Station, Texas 77843 (US).
- (74) Agent: DEVSHI, Usha; Qatar Financial Centre Branch licensed by the, Qatar Financial Centre Authority (QFC No. 00144), Al Fanduq Street, PO Box 26100 West Bay, Doha (QA).
- (81) Designated States (unless otherwise indicated, for every kind of national protection available): AE, AG, AL, AM, AO, AT, AU, AZ, BA, BB, BG, BH, BN, BR, BW, BY, BZ, CA, CH, CL, CN, CO, CR, CU, CZ, DE, DJ, DK, DM, DO, DZ, EC, EE, EG, ES, FI, GB, GD, GE, GH, GM, GT, HN, HR, HU, ID, IL, IN, IR, IS, JO, JP, KE, KG, KH, KN, KP, KR, KW, KZ, LA, LC, LK, LR, LS, LU, LY, MA, MD, ME, MG, MK, MN, MW, MX, MY, MZ, NA, NG, NI, NO, NZ, OM, PA, PE, PG, PH, PL, PT, QA, RO, RS, RU, RW, SA, SC, SD, SE, SG, SK, SL, SM, ST, SV, SY, TH, TJ, TM, TN, TR, TT, TZ, UA, UG, US, UZ, VC, VN, ZA, ZM, ZW.
- (84) Designated States (unless otherwise indicated, for every kind of regional protection available): ARIPO (BW, GH, GM, KE, LR, LS, MW, MZ, NA, RW, SD, SL, ST, SZ, TZ, UG, ZM, ZW), Eurasian (AM, AZ, BY, KG, KZ, RU, TJ, TM), European (AL, AT, BE, BG, CH, CY, CZ, DE, DK, EE, ES, FI, FR, GB, GR, HR, HU, IE, IS, IT, LT, LU, LV, MC, MK, MT, NL, NO, PL, PT, RO, RS, SE, SI, SK, SM, TR), OAPI (BF, BJ, CF, CG, CI, CM, GA, GN, GQ, GW, KM, ML, MR, NE, SN, TD, TG).
- Published:**
— without international search report and to be republished upon receipt of that report (Rule 48.2(g))
— in black and white; the international application as filed contained color or greyscale and is available for download from PATENTSCOPE
- (54) Title: PROCESSING METHANE FOR SYNGAS PRODUCTION WITH REDUCED CO₂ EMISSIONS
- (57) Abstract: A method for processing methane includes processing methane in presence of a carbon dioxide stream, whereby a synthesis gas including carbon monoxide and hydrogen is produced. The synthesis gas is contacted with a carbon monoxide-absorbing solution, thereby removing at least a portion of the carbon monoxide and producing a final synthesis gas having an increased ratio of hydrogen to carbon monoxide.

WO 2019/194694 A2